Utrecht University

Master Thesis

Bandgap Engineering of $Cs_2AgBiBr_6$ for Improved Photochemical Activity

Joost Reinders

01/06/2022

Inorganic Chemistry and Catalysis, Department of Chemistry, Utrecht University, PO Box 80125, 3584 CG Utrecht, The Netherlands

Bandgap Engineering of $Cs_2AgBiBr_6$ for Improved Photochemical activity

Joost Reinders[1]

June 1, 2022

Under supervision of H. Jöbsis[1] & Dr. E. Hutter[1]

1: Inorganic Chemistry and Catalysis, Department of Chemistry, Utrecht University, PO Box 80125, 3584 CG Utrecht, The Netherlands

Abstract

Photochemistry is a process based on transforming the energy of absorbed photons into chemical bonds. Here, sunlight-induced charge generation in a semiconductor material can facilitate the conversion of various (waste) materials into value-added chemicals via reduction or oxidation. To achieve high conversion efficiencies, the semiconductor requires a bandgap with an energy matching the reduction or oxidation potential of the respective species. In addition, the absorption of the semiconductor should overlap with the emission of sunlight to minimize absorption losses. Photochemistry is a promising way to tackle some of the global issues faced today. Due to the ever-growing CO_2 pollution in the atmosphere, the photoinduced reduction of CO_2 into useful chemical building blocks, such as CO and CH_4, can play a paramount role in reversing the devasting effects of CO_2 on the global climate. In this work we continue on this virtue and focus on using elpasolite-structured $Cs_2AgBiBr_6$ (CABB) for photochemical reactions. This photoactive material is better known as a double perovskite (DP) and has a high stability under ambient conditions. However, CABB shows moderate absorption of visible light, especially at higher wavelengths. We aim to increase the visible light absorption of CABB by substituting the Bi^{3+} cation with another cation, lowering the bandgap energy and shifting the absorption towards higher wavelengths. This way we seek to increase the photochemical activity of CABB without compromising the chemical stability. We have first incorporated Sb^{3+} at the sites of Bi^{3+} at known ratios of Sb^{3+}:Bi^{3+} and synthesized crystalline DP thin films. We assessed the photochemical activity of these thin films for photochemical CO_2 reduction and monitored the production of CO and CH_4 via gas chromatography. These measurements indicated that the low performance of our DP thin films makes it challenging to observe the effect of bandgap manipulation on the photoactivity. Hence, we directed our research to another photochemical process, namely dye degradation, which is often used as a model system to study changes in photochemical activity. In this part of the work, we are interested in evaluating the effect of DP alloying on the photochemical activity towards rhodamine B (RhB) and methylene blue (MB) degradation. A solid-state mechanochemical synthesis approach is used to produce an extensive inventory of different alloyed DPs, (partially) replacing the Bi^{3+} with Sb^{3+}, In^{3+}, Fe^{3+}, Al^{3+}, Sn^{2+}, and Ti^{4+}, respectively. Crystallography analysis reveals that, using a ball mill setup, each of the cations mentioned above could be incorporated into the CABB crystal structure forming a crystalline composite. In addition, UV-Vis diffuse reflectance spectroscopy shows a favorable redshift of the absorption for some of these composites (*i.e.*, Sb, Fe, Sn, and Ti-based DPs). Several dye degradation experiments are recorded under irradiation of various light sources. The results of these experiments indicate that the addition of up to at least 10% Fe^{3+} as replacement of Bi^{3+} improves the light absorption and enhances the degradation rate of MB under irradiation of blue and green light. These results highlight the promising endeavor towards improving photochemical reaction activities of DP materials.

Preface

This research project was commissioned and supervised by Dr. Eline Hutter, head of the Photochemistry group at Utrecht University, and was carried out under the daily supervision of Huygen Jöbsis. This work is part of my Master programme in Nanomaterials Science in accordance with Utrecht University, Department of Chemistry, in the group of Inorganic Chemistry and Catalysis (ICC). My work focused on manipulating the bandgap energy of $Cs_2AgBiBr_6$ to improve its photochemical activity.

Utrecht, June 2022 *Joost Reinders*

List of Abbreviations

CABB	$Cs_2AgBiBr_6$
DP(s)	Double perovskite(s)
ICC	Inorganic Chemistry and Catalysis
DMSO	Dimethyl sulfoxide
GC	Gas chromatography
UV-Vis	Ultraviolet-visible spectroscopy
AFM	Atomic force microscopy
SEM-EDX	Scanning electron microscopy energy dispersive X-ray spectroscopy
XRD	X-ray diffraction
RhB	Rhodamine B
MB	Methylene blue
Redox	Reduction and oxidation
VB	Valence band
CB	Conduction band
eV	Electron volts
PL	Photoluminescence
ETL	Electron transport layer
HTL	Hole transport layer
FWHM	Full width at half-maximum
RMS	Root-mean square
AM	Air mass
RPM	Rotations per minute
RT	Room temperature
NP(s)	Nanoparticle(s)

Table of contents

Chapter 1. Introduction

Sunlight can be considered as an excellent renewable alternative energy source to fossil fuels thanks to its low environmental impact and abundance. This energy source can be harvested through the absorption of photons, where its energy is converted into chemical bonds (photochemistry).[1] Due to the global impact of CO_2 pollution, the reduction of CO_2 into value-added chemicals is regarded as one of the holy grails of photochemistry.[2]

Sunlight conversion, however, faces several problems that limit its efficiency. A problem that often occurs is the low absorption of photons by the material, since most semiconductors absorb light in the lower visible and UV region, whereas sunlight irradiation covers a broader spectral range with a maximum around 550 nm.[3] Owing to their suitable optical and electronic properties, perovskites have recently been investigated as promising candidates to tackle this low-absorption issue.[4,5] A limitation to the most studied perovskite materials is their instability towards air and moisture exposure and toxicity.[6] $Cs_2AgBiBr_6$ (CABB) however, is a perovskite-like material which exhibits improved stability in (humid) air and is less toxic compared to other researched perovskites.[7] Although this material has an elpasolite crystal structure, it is more commonly known as a double perovskite (DP). An additional benefit of CABB is that its range of absorption can be tuned by exchanging one or more of the elements within the crystal structure.[8]

The work presented here focuses on the study of DP composites for their use in photochemical reactions and how bandgap engineering will impact the photochemical activity. To fully understand the purpose of this work it is necessary to discuss the theoretical aspects in detail. Hence, the theoretical background on the subject of photochemistry, perovskites and DPs, characterization techniques, crystallography, model reactions of photochemistry, and photochemical CO_2 reduction is discussed in Chapter 2.

We first explore the possibility of improving the visible light absorption of CABB-based thin films by exchanging Bi^{3+} with Sb^{3+}, redshifting the absorption (Chapter 3).[8] These thin films are produced by spin coating, involving the dissolution of bromide precursor salts in dimethyl sulfoxide (DMSO). Next, the photochemical performance of the DP thin films is tested for CO_2 reduction. Here, DP thin films are employed in a flow cell reactor coupled to a gas chromatograph (GC) to detect possible products (*i.e.*, CO and CH_4) of CO_2 photoreduction. The synthesis of so-called charge transport layers is also investigated. These layers can provide an improved separation of photogenerated charges. Characterization of the DP and charge transport thin films is performed with ultraviolet-visible (UV-Vis) spectroscopy, atomic force microscopy (AFM), scanning electron microscopy energy dispersive X-ray spectroscopy (SEM-EDX), and X-ray diffraction (XRD). These techniques allow us to record the optoelectronic, structural, elemental, and crystalline properties of the thin films, respectively.

Chapter 4 provides a detailed description of the synthesis of various alloyed DPs based on CABB. First, using a hot solution-based approach, crystals of CABB and $Cs_2AgSbBr_6$ (CASB) are synthesized. Next, an extensive inventory of bulk powders of DP composites with general form of $Cs_2AgM_xBi_{x-1}Br_6$ (M = Sb, In, Fe, Al, Sn, Ti) is obtained via a solid-state mechanochemical synthesis. The exchange of Bi^{3+} with cationic M changes the band structure of the DP, allowing the control over the optoelectronic properties.[9] The optoelectronic, elemental, and crystallographic properties of DP composites are analyzed by means of UV-Vis, SEM-EDX, and XRD, respectively. The aim is to synthesize crystalline DP composites that have an improved optical light absorption compared to CABB.

In Chapter 5 we report on the photochemical performance of the various DP composites towards dye degradation. We use a photochemical system of suspended DP powders in ethanoic solutions of rhodamine B (RhB) and methylene blue (MB), respectively. The decay of these dyes is measured over time while the DP suspensions are exposed to various sources of light. The aim of these experiments is to shed more light on the effect of elemental exchange in CABB on the photochemical activity of DPs.

Our findings are summarized in Chapter 6 with some remarks concerning the prospects on this topic. We will briefly give concluding comments on the synthesis, optical and structural properties, and performance towards CO_2 photoreduction of DP thin films. In addition, we review the mechanochemical synthesis of DP composites including their characterization and photochemical activity towards dye degradation.

Chapter 2. Theoretical background

To fully understand the purpose and insights of this project it is necessary to discuss some theoretical aspects in detail. First, we will elaborate on the prior art of photochemistry and how the current technology faces several problems regarding efficiency losses. The importance of perovskites and DPs for next-generation photochemistry applications is discussed next. We also focus on the formation mechanisms and synthesis routes of DPs. The fundamentals of UV-Vis spectroscopy and XRD is discussed next. The use of dye degradation as a model reaction for monitoring the photochemical activity is reviewed next. The final aspect that will be discussed is the pathway for photochemical CO_2 reduction.

2.1 Photochemistry

Photochemistry involves light-driven chemical effects.[10] This branch of chemistry is often used to induce chemical changes in molecules via reduction and oxidation (redox) reactions driven by photoexcited charges. Especially the last few decades, the number of applications involving photochemistry has increased significantly due to the ever-growing need of alternative fuel sources and reducing the CO_2 emissions, for example.[11]

The process of photochemistry consists of the following steps (Fig. 1). A semiconductor, a material which has its valence band (VB) and conduction band (CB) separated by an energy gap known as the bandgap, is exposed to electromagnetic radiation. Incident photons having an energy equal to or higher than the bandgap energy can excite electrons from the VB to the CB. The photogenerated charge carriers can subsequently migrate to the surface. At the surface, interfacial charge transfer processes and charge recombination can take place. Defects at the surface act as interfacial charge pathways allowing redox reactions to take place, while these defects also promote the recombination of charge carriers.[12]

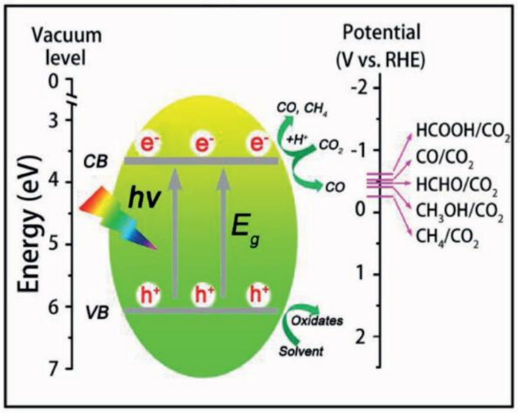

Figure 1. Schematic display of the photochemical reduction of CO_2, reproduced from Zhou *et al.*[7]

In practice, there are some issues to this process that limit the efficiency of photoconversion. In the first place, the nature of the bandgap plays a paramount role. The bandgap can either be direct or indirect, which depends on the alignment of the crystal momentum of the CB minimum and VB maximum.[13] The crystal momentum (or k-vector) is described as the momentum of electrons in a crystalline domain which reflects the periodicity of the crystal lattice. In a direct bandgap semiconductor, the momenta of the CB minimum and VB maximum are aligned whereas for an indirect bandgap these momenta are not aligned. This is depicted in Fig. 2. Here, the indirect transition from the VB to the CB does not satisfy the requirement of conservation of wavevector. However, if in this process a phonon is created the indirect transition is allowed according to the laws of conservation. Phonons are lattice vibrations oscillating at a single frequency.[14] Since an indirect transition requires both photons and phonons, the probability of this transition taking place is significantly lower than for a direct transition which is not dependent on phonons. This probability coincides with the degree of light absorption since the absorption of photons propagates the transition from VB to CB. In addition, phonons are known to be temperature dependent. Temperature-induced phonons can improve the light absorption of indirect semiconductors by shifting the absorption towards higher wavelengths.[15] The above considerations regarding the nature of the bandgap reveal that an indirect bandgap is not preferential for photoconversion applications due to the inferior absorption compared to a direct bandgap material.

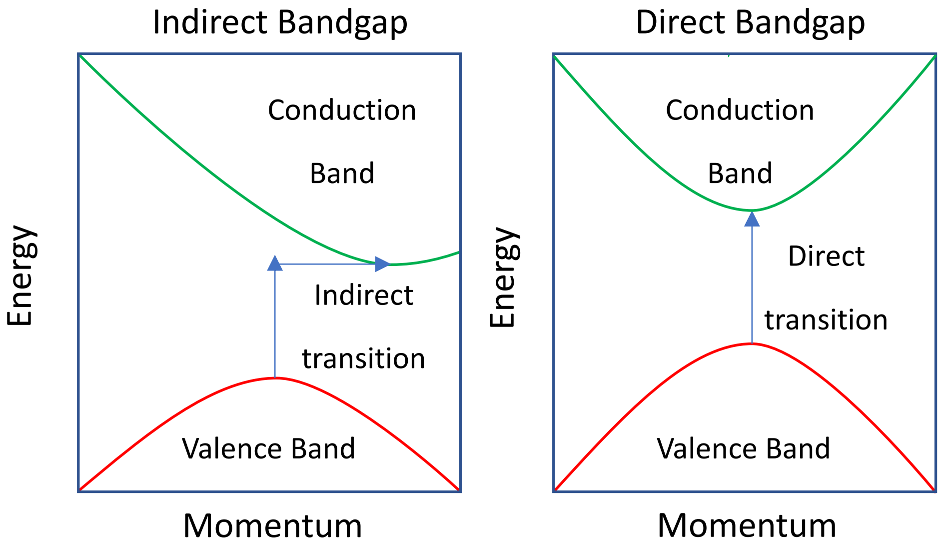

Figure 2. Schematic of an indirect bandgap and direct bandgap material.

Another concern that comes to light when discussing semiconductors is the recombination of charges. Here, photoexcited carriers relax from the CB to a lower energy state, either via non-radiative (*i.e.*, heat) or radiative (*i.e.*, light emission) decay.[16,17] Defect states that are located deep in the bandgap of the semiconductor, known as deep level states, can act as recombination centers to facilitate non-radiative decay.[18] If defects are close to the band edge of the CB or VB, however, these shallow states can act as trapping sites, localizing one of the charge carriers without undergoing recombination.[16]

The radiative decay process involves the relaxation of excited electrons to a lower energy state, thereby recombining with holes, leading to the emission of photons.[16,19] The resulting emission can be analyzed with photoluminescence (PL) measurements. The time a charge carrier remains in the excited state before it relaxes to a lower energy state is expressed as the carrier lifetime, which is usually in the order of pico- to nanoseconds, depending on the material.[20,21]

Due to the increasing demand for photoconversion applications, studies have focused on ways to tackle the charge carrier loss through recombination. For example, Zhang *et al.* incorporated metallic clusters into a semiconductor material which improved the charge separation of photogenerated holes and electrons. Metal particles are known to “collect” electrons, preventing them from being subject to recombination with holes.[22] Hirakawa *et al.* found that Ag in a Ag@TiO_2 core-shell structure is able to store photoexcited electrons, making them available on demand.[23] Zhang *et al.* employed this strategy to improve the photochemical dye degradation rate of $Cs_2AgBiBr_6$.[24]

Research has also been focusing on the use of so-called charge transport layers to effectively separate the photogenerated electrons and holes.[3,25,26] This strategy is often used in thin film devices, where the photoactive material is sandwiched between an electron transport layer (ETL) and a hole transport layer (HTL).[3] The resulting structure is better known as a so-called tandem cell. The charge transport layers can either exist of inorganic metal oxides or organic compounds.[27] Fig. 3 shows a schematic of the charge transfer processes that can take place in a sandwiched structure of ETL–photoactive material–HTL. Here, electrons are excited from the VB to the CB of the photoactive material (1). The electrons can then either migrate to a slightly lower energy state of the CB of the ETL (2) or recombine with holes in the VB (4). At the same time, photogenerated holes transfer to the VB of the HTL (3). In an ideal situation the electrons and holes occupy the CB of the ETL and VB of the HTL, respectively. Unfortunately, undesirable processes will also take place where the electrons and holes recombine via (5) and (6).[20]

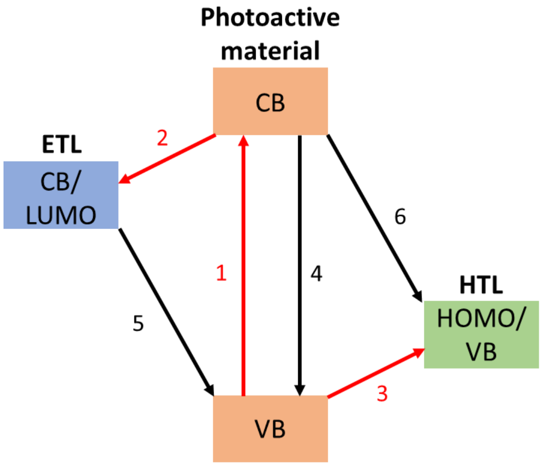

Figure 3. Depiction of charge transfer processes in a photoactive tandem cell.

Whether a material is suitable to act as a charge transport layer depends on the band alignment and bandgap energy of both transport layers and the photoactive material.[28] For example, the CB of the ETL should not be higher in energy than the CB of the photoactive material, otherwise it would be energetically more favorable for the excited electrons to recombine with holes in the ground state. The same principal applies to the position of the VB of the HTL, which should in fact be higher in energy than the VB of the photoactive material. The choice of selecting which ETL and HTL to use can be made by looking at an energy band alignment diagram as represented in Fig. 4.[28] Here, some of the traditional photocatalysts with their respective band edge energies are presented, compared to the more recently investigated lead halide perovskites.

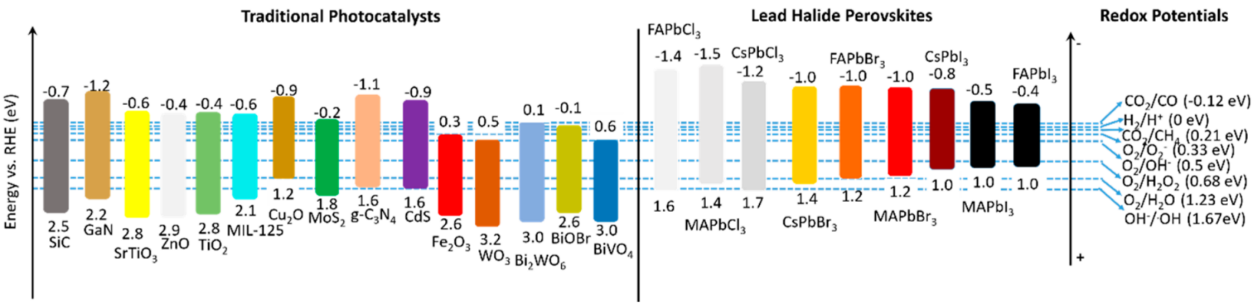

Figure 4. Various photocatalysts with their respective band edge positions (vs. reversible hydrogen electrode), compared to more recently investigated lead halide perovskite photocatalysts. Redox potentials of some important half reactions are given on the right. As reproduced from Huang *et al.*[28]

Another key issue of a semiconductor material is that it often lacks decent absorption of incident sunlight. For some common semiconductors, such as TiO_2 and NiO_x, the absorption starts to rise in the UV region, while in the visible part of the spectrum its absorption can be neglected such that most of the solar energy from sunlight is discarded. Due to the poor overlap of the absorption of these semiconductors and the spectral range of sunlight, there has been extensive research in the quest for other promising photoactive materials to be used in photoconversion devices. A field of investigated materials are perovskites and DPs, which will be discussed in the next paragraph.

2.2 Perovskites and double perovskites

Perovskites and DPs offer some unique optoelectronic properties compared to conventional semiconductors, which will become apparent in this paragraph. Perovskites have the general formula ABX_3 in a cubic structure with octahedral symmetry, as shown in Fig. 5.[29] Here, A and B are cations, and X is an anion that is bonded to these cations. Regarding the position of these ions, in an ideal structure, the larger A cation is located in the center of the cubic structure and the smaller B cations are positioned in the octahedral holes which are formed by the X anions.[30]

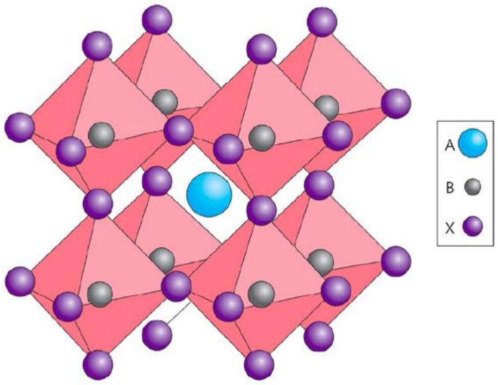

Figure 5. Depiction of a cubic perovskite crystal structure in the form of ABX_3, reproduced from Green *et al*.[30]

In the last decade, research has focused on replacing the traditionally used semiconductors for photoconversion applications with more promising photoactive materials. Organometallic halide perovskites are well-studied materials for these applications since they reveal good stability under ambient conditions and show an increased absorption of visible light compared to traditional metal oxide semiconductors.[31,32] One concern regarding the use of these perovskites is the presence of lead. Given the growing appreciation of using environmentally friendly materials, the applications for these lead-based perovskites are limited. In addition, the relatively small bandgap of these perovskites is not ideal for photochemistry, as will be discussed further in Chapter 2.4 and 2.5. Hence, studies have focused on the development of other perovskite-based photoactive materials.

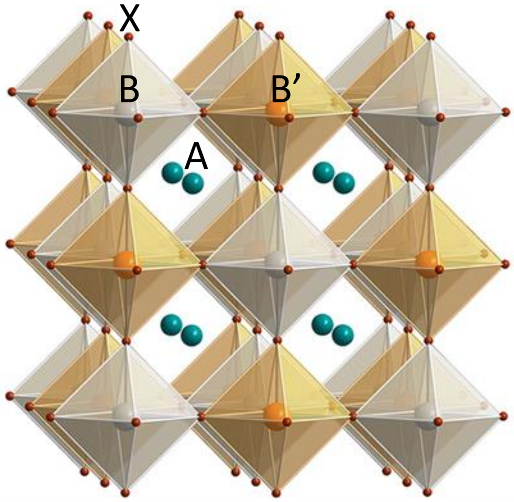

Figure 6. Schematic of a typical cubic DP crystal structure in the form of $A_2BB'X_6$, reproduced from Slavney *et al*.[44]

One branch of perovskite-based photoactive materials are the so-called double perovskites. These photoactive materials show promising optoelectronic properties, competing with the already established performance of lead-based perovskites towards photoconversion.[33] The term double perovskite entails a crystal structure known as elpasolite. The elpasolite structure displays a similar cubic structure as perovskites (Fig. 6). DPs consist of three different cations and one anion in the form of $A_2BB'X_6$. Generally, the X anion consists of either an oxygen or a halide, A is a monovalent cation which is larger than the monovalent B cation and trivalent B' cation, respectively.[34] Furthermore, the ordering of crystal structure is rock-salt, where A^+ is located in the framework cavities of the structure and $[BX_6]^{5-}$ and $[B'X_6]^{3-}$ octahedra alternate in the 3D space.[35]

The formation of these structures strongly relies on the ionic radii of the cations and anions that are used. There have been many efforts on determining criteria to assess the formability of perovskites.[36–39] Victor Goldschmidt was the first to report on this matter in 1926, introducing the Goldschmidt tolerance factor t, giving an indication of the stability of perovskites based on the ionic radii:[38]

$$t = \frac{r_A + r_X}{\sqrt{2}(r_B + r_X)} \tag{1}$$

Where, r_A, r_B and r_X are the ionic radii of A, B and X, respectively. There is a consensus that perovskites have a high probability of successful formation when $0.825 < t < 1.059$.[36] In addition to this tolerance factor, the so-called octahedral factor is often considered to predict the stability of the perovskite structure.[39] The octahedral factor μ is defined as:

$$\mu = \frac{r_B}{r_X} \tag{2}$$

Where stable perovskites fall in the range of $0.414 < \mu < 0.732$. Recently, Bartel *et al.* developed an improved tolerance factor τ that predicts 92% of the formation of perovskites correctly.[36] This tolerance factor combines the octahedral factor with a rewritten version of the Goldschmidt tolerance factor, stating that:

$$\tau = \frac{r_X}{r_B} - n_A\left(n_A - \frac{r_A/r_B}{\ln(r_A/r_B)}\right) \tag{3}$$

Where, n_A is the oxidation state of cation A. The new developments on predicting the formation of perovskites paves a way to study the formation of novel perovskites with improved optoelectronic properties for photochemical applications.

Considering the variety of cations, there are many different elemental compositions possible for the formation of perovskites.[40] This questions which combinations of cations and anions are possible. Similar to predicting the stability and formation of perovskites, the same concept can be applied to determine the probability of DP formation using the already mentioned tolerance factor τ. Instead of using the ionic radius of B, the mean ionic radius of B and B' are considered. This simplified approach allows one to predict the stability of DPs in a similar manner as for perovskites.

The synthesis of such DP materials has been studied in great detail over the years, ranging from solution-based synthesis methods to develop thin films to the solvent-free approach yielding crystalline powders.[41–44] A major drawback of solution-based syntheses is that the formation of stable DPs in solution are prone to side reactions, leading to the formation of unwanted perovskite analogues.[45] The undesirable side reactions are mainly predominated by precursor solubility which governs the stoichiometric outcome of the synthesis. So, the exploration of various DPs for thin film applications is limited due to the critical role of precursor solubility on the formation of DPs.

A promising method to avoid the formation of unwanted secondary phases is the solid-state mechanochemical synthesis.[45] Here, precursors in a stoichiometric ratio are mixed under high shear, mechanical force and pressure, driving the formation of a single-phased DP product. The consensus on the formation mechanism is that continuous mechanical action induces a particle size decrease which leads to the exposure of more reactive surfaces. These surfaces encounter other reactive surfaces and favor the formation of the desired product.[46] In the literature this approach is used to synthesize nanocrystals (NCs) and bulk powders, such as the work of Bolink *et al.* that reports on the synthesis of CABB bulk powders using a ball mill.[47] In this work the following reaction pathway is proposed:

$$3\ \mathrm{CsBr} + \mathrm{BiBr_3} \longrightarrow \mathrm{Cs_3BiBr_6} \tag{4}$$

$$\mathrm{Cs_3BiBr_6} + \mathrm{BiBr_3} \longrightarrow \mathrm{Cs_3Bi_2Br_9} \tag{5}$$

$$\mathrm{Cs_3Bi_2Br_9} + 2\ \mathrm{AgBr} + \mathrm{CsBr} \longrightarrow 2\ \mathrm{Cs_2AgBiBr_6} \tag{6}$$

Where CsBr and $BiBr_3$ initiate the reaction (4), and the incorporation of AgBr is a slower process taking place at a later stage (6). The authors were able to elucidate the mass fractions of the initial precursors, intermediates, and final product at certain time intervals during the synthesis. It was found that the formation of CABB is predominant in the first 15 minutes, forming almost phase-pure CABB (Fig. 7). It should be noted that the only secondary phase remaining after 60 minutes is AgBr, suggesting that the incorporation of this precursor is energetically challenging. This study also shows that the mechanochemical synthesis offers a rapid and facile approach to produce various DP compositions.

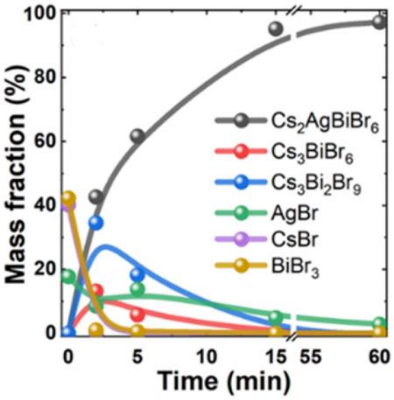

Figure 7. Mass fractions of precursors and intermediates during the mechanochemical synthesis of CABB, reproduced from Rodkey *et al*.[47]

In terms of photoactive DPs, CABB is a promising emerging material thanks to its low toxicity and great stability in ambient conditions, as we will demonstrate in Chapter 5.[35,44,48] Among these favorable characteristics, CABB still faces some challenges. One is the indirect nature of the bandgap which limits its absorption of light, as was discussed previously in Chapter 2.1. In addition, studies found that the absorption coefficient of CABB in the visible part of the electromagnetic spectrum (380-700 nm) is an order of magnitude smaller than the absorption coefficient of the direct bandgap perovskite $MAPbI_3$.[35] The absorption coefficient describes the attenuation of light intensity as light passes through a material.[49] Fig. 8 shows a typical absorption spectrum of a CABB thin film. At low wavelengths (<420 nm) the absorption sharply rises. This absorption plateau is attributed to the direct bandgap of CABB.

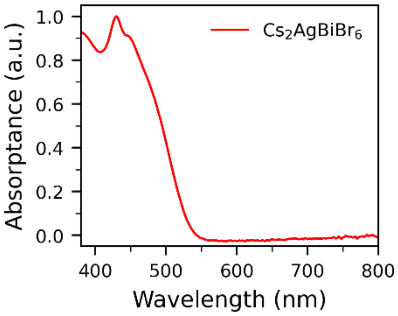

Figure 8. Absorption of CABB.

The origin of the absorption peak around 440 nm is still unknown. It is postulated that this feature arises either from excitonic absorption, localized Bi 6s6p transitions, or charge transfer transitions between Ag and Bi/Br orbitals.[35] The indirect nature of the bandgap presents itself as a broadening of the absorption feature at 440 nm going to higher wavelengths.

To tackle the poor light absorption at higher wavelengths, research groups have focused on finding ways to manipulate the bandgap of CABB.[9,43,50,51] One of the most commonly used practices is the heterovalent substitution of a native ion with a different ion, such as the substitution of Cs^{2+} with Rb^{2+}, Ag^{+} with Na^{+}, Bi^{3+} with Sb^{3+}, or Br^{-} with Cl^{-}.[8,52–54] The replacement of a native ion changes the electronic band structure of the material, shifting the VB and/or CB band edges. Band structure calculations of CABB performed by Du *et al.* reveal that the CB minimum derives from the Bi 6p orbitals, whereas the VB maximum is a contribution of Bi 6s, Ag 4d and Br 4p orbitals.[51] This study also shows that when a fraction of the Bi^{3+} cations is substituted by Sb^{3+}, the contribution of its 6p orbitals becomes less and the effect on the CB minimum position becomes less apparent. Hence, the contribution of other orbitals in the crystal structure become more pronounced. Furthermore, when Sb^{3+} is substituted with 25% of the Bi^{3+} cations, the Sb 5p orbitals introduce an orbital-derived band just below the CB minimum. The same effect applies to the position of the VB maximum, where a Sb 5s orbital derived band is being introduced above the VB maximum. According to the calculations, the increase of the VB maximum is approximately twice as large as the decrease of the CB minimum when Sb^{3+} is introduced in the crystal structure.[51]

Some cases also exist of heterovalent substitution. For example, Lindquist *et al.* investigated the heterovalent substitution of Sn^{2+} and Sn^{4+} with Ag^{+} and Bi^{3+} in the CABB crystal structure (Fig. 9a).[55] It is postulated that Sn^{2+} takes the position at the Ag^{+} site while Sn^{4+} is located at the Bi^{3+} site. The disparity between valences of Sn^{4+} and Ag^{+} makes the substitution between the two unlikely. In conjunction with the heterovalent substitution, the formation of lattice vacancies assure that charge neutrality is maintained. Elemental and structural analysis of single crystals reveals that Ag^{+} vacancies are the primary source of negatively charge compensating defects, while Bi^{3+} vacancies can be neglected. Fig. 9b) shows how the increase of Sn content in CABB crystals affects the visual appearance of the crystals in terms of its color. The optoelectronic changes are quantified

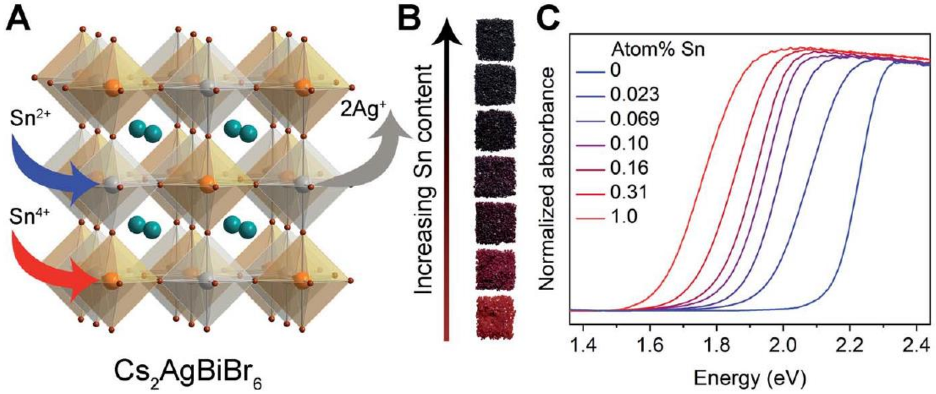

Figure 9. a) Representation of the crystal structure of CABB, where Sn^{2+} and Sn^{4+} accommodate the positions of Ag^{+} and Bi^{3+}, respectively. **b)** Sn-alloyed CABB crystals with increased Sn concentration. **c)** UV-Vis absorbance spectra of Sn-alloyed CABB crystals, reproduced from Lindquist *et al.*[55]

in Fig. 9c), showing a shift to lower energies with an increased concentration of Sn^{2+} and Sn^{4+} into the crystal structure of CABB.[55] Computational studies show that the change in optical properties is induced by the mixing of the Sn 5s orbital with the Br 4p orbital in the VB maximum and of the Sn 5p orbital with the Bi 6p orbital in the CB minimum.[50,56] The mixing of the Sn 5s orbital in the VB pushes the band edge upwards, while introducing the Sn 5p orbital in the CB increases the width of this energy band, lowering the bandgap energy, and even changes the nature of the bandgap transition from indirect to direct.

These computational studies, complemented with experimental data, demonstrate how the substitution of cations results in strategies to manipulate the bandgap of DPs and allows for the tuning of optical properties. In this work we aim to manipulate the bandgap of CABB through ion exchange as well. To study the effect of ion replacement on the absorptive properties we will use UV-Vis spectroscopy, and to check the formation of a single crystal phase X-ray diffraction crystallography is used. In the next section, these characterization techniques are briefly described.

2.3 Characterization of optoelectronic properties

The optical properties of photoactive materials are commonly characterized using UV-Vis. This method is a versatile technique to analyze the reflective, transmissive and absorptive properties of different samples, such as solutions, colloidal dispersions, thin films, single crystals, powders, *etc.* Depending on the type of sample (*e.g.*, solution, colloidal dispersion, thin film, single crystal, powder) the measurement is performed in a different manner. In this section, we will focus on UV-Vis measurements involving powder and thin film samples.

In the case of analyzing the optoelectronic properties of powders, one can only consider the reflectance. Powders are generally an infinitely thick sample of which the transmittance is zero. The total reflectance can be regarded as the sum of specular and diffuse reflectance. Specular, or mirror reflectance, entails the reflectance of light at the same angle as the incident light on the reflecting surface on the opposite side.[57] The contribution of both reflection phenomena depends mainly on the sample particle size, structure and other properties that influence the so-called surface state. Since powders consist of small domains of reflecting surfaces, the reflection of light is regarded as diffuse since the orientation of the reflecting surfaces is random. The diffuse reflectance can also be described as a phenomenological result of reflection, refraction, diffraction, and absorption. However, one also needs to consider that, when the particle size is smaller than or identical to the incident wavelength, these various contributions to diffuse reflectance are inseparable. This is better known as scattering.

Typically, the total reflectance is measured in an integrating sphere (Fig. 10), where specific geometric conditions apply and the material covering the inside has a diffuse reflectance close to unity. Here, a light source irradiates the sample at an angle of no more than 10°.[57] The angular position of the beam towards the sample ensures no light will be directly reflected back through the transmittance port (entrance of the source beam). Some of the light will be absorbed and the remaining light is reflected either as spectral or diffuse reflectance. In some cases, a specular exclusion port is located at the opposite angle of the transmittance port. By removing the specular exclusion port, one is able to only measure the diffuse reflectance as the specular beam is reflected out of the integrating sphere.

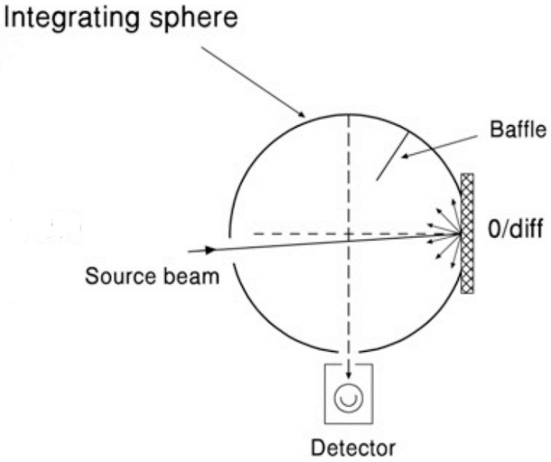

Figure 10. Schematical depiction of an integrating sphere, reproduced from Torrent

In 1931, P. Kubelka and F. Munk presented a theory to approximate the diffuse reflection of light of an inhomogeneous and infinitely thick layer.[58] The Kubelka-Munk theory that was put forward describes the diffuse reflectance R_∞ of such a material as:

$$R_\infty = 1 + \frac{a}{r} - \sqrt{\frac{a^2}{r^2} + 2\frac{a}{r}} \tag{7}$$

Where, a is the absorption coefficient and r the scattering coefficient. One can rewrite eq. 7 to obtain a new term, $F(R_\infty)$, where the diffuse reflectance is directly related to the ratio of absorption coefficient and scattering coefficient, as written as:[59]

$$F(R_\infty) = \frac{a}{r} = \frac{(1-R_\infty)^2}{2R_\infty} \tag{8}$$

Since the Kubelka-Munk function, as stated in eq. 8, is approximately proportional to the absorption coefficient, a transformation is obtained from the diffuse reflectance to a measure for absorption ($F(R_\infty)$).

If we consider thin films, the assumption of an infinitely thick layer breaks down. However, using an integrating sphere, the absorptance (fraction of absorbed light, A) can be determined. By placing the thin film inside the integration sphere the sum of reflectance (fraction of reflected light, R) and transmittance (fraction of transmitted light, T) is recorded. As the sum of A, R and T should be unity, ignoring scattering, A can be calculated using:[8]

$$A = 1 - (R + T) \tag{9}$$

By placing the thin film at the side of the integrating sphere only R is recorded so that T can be calculated as well:

$$T = 1 - A - R \tag{10}$$

To conclude, depending on the DP material (*e.g.*, powder-based or thin film), the optical properties can be studied in different ways. Next to the optical properties, the crystallinity of DP materials is another important characteristic when considering photoconversion applications. The aspect of crystallography will be discussed in the next paragraph.

2.4 Crystallography

X-ray diffraction (XRD) is a common technique to study the crystallographic characteristics of perovskites and DP materials. This technique allows to determine the crystal structure which is based on the presence and orientation of lattice planes in the crystal.[60] XRD is able to detect the reflections of X-rays on these lattice planes, obtaining a pattern corresponding to the angles of reflection.[14]

Lawrence Bragg and William Henry Bragg were the first to relate the reflection angle to the spacing between lattice planes in a crystal.[61] When a crystalline material is exposed to electromagnetic radiation with wavelengths in the order of 10^{-9} to 10^{-11} m, waves scatter from lattice planes that are separated by distance d. If the scattered waves are in-phase they undergo constructive interference and specularly reflect off the lattice, where the angle of reflection is equal to the angle of incidence. The angle of reflection θ (in radians) is governed by the radiation wavelength λ (in Å), order of diffraction n, and spacing between lattice planes d (in Å). This is formulated into the Bragg's law:[14]

$$n\lambda = 2d\sin\theta \tag{11}$$

The spacing between lattice planes depends on the radii of cations and anions, as well as the crystal structure.[62] By the exchange of an ion with a homovalent ion, the distance between lattice planes will either contract or expand, depending on the ionic radii of the substituting ion. The change in lattice constant can be observed as a shift of the reflection angles in a diffractogram. From the Bragg's law in eq. 11, one can calculate the change in lattice constant (d) when the reflection angle (θ) is determined, given that the λ is the same.

One should also note that the value of n in eq. 11 is always an integer and corresponds to the difference in path length of diffraction between two lattice planes in the crystal structure.[14] These planes are described by so-called Miller indices; numbers that indicate the orientation of lattice planes. If one considers the crystal unit cell as a 3D space with axis along the dimensions of this space, then the Miller indices are determined from the intersection point of the planes with each of the axis.[63] The corresponding indices are represented by h, k, and l.

The lattice spacing d of a cubic cell can be expressed as a function of the Miller indices:[60,64]

$$d = \frac{a}{\sqrt{h^2+k^2+l^2}} \tag{12}$$

With a the lattice constant. Combining eq. 11 and eq. 12 yields the following relation for the lattice constant:

$$a = n\lambda\frac{1}{2\sin\theta}\sqrt{h^2+k^2+l^2} \tag{13}$$

Giving a direct relation of the diffraction angle on the lattice constant, since n, λ, h, k and l are constant if only a single reflection angle is considered:

$$a \propto \frac{1}{\sin\theta} \tag{14}$$

In addition to lattice constant, the full width at half-maximum (FWHM) of a diffraction peak can be used to perform a structural analysis on a crystalline material. In 1918, the Swiss physicist Paul Scherrer, related this width to the size of a crystalline domain:[65]

$$\tau = \frac{K\lambda}{\beta\cos\theta} \tag{15}$$

Where K is a unitless shape factor (for cubic structures K≈0.9) and β is the line broadening of the FWHM in radians. According to Cullity and Stock, this approximation of the crystalline domain size is only valid for domains below 200 nm.[63] Their claim on this limitation is based to the resolution of the diffractometers, however.[66] This so-called Scherrer limit was further investigated by Muniz *et al.*, showing that the Scherrer limit is inversely proportional to the absorption coefficient of the crystalline material.[66,67]

The crystallographic properties can be very well analyzed using XRD. Useful information can be extracted from the acquired reflection angles, such as the presence of certain lattice planes and crystal domain size. These characteristics are of key importance for the characterization of crystalline materials.

2.5 Model reactions of photochemistry

We previously discussed the essence of photochemistry, types of photoactive materials and their limitations, and the optoelectronic characteristics concerning their form (*i.e.*, powder-based and thin films). In this section we will focus on some prior art of perovskite and DP related photochemistry, emphasizing on the model reactions of dye degradation.

The degradation of dyes has been intensively studied in the photochemistry community.[68–70] The reports that focus on the degradation of dyes often declare the work as a proof of principle study. By using the dye degradation as a model reaction, the fundament has been laid for work on more relevant and impactful photocatalytic reactions, such as CO_2 reduction. In these studies, many have focused on using TiO_2 in an aqueous solution, under irradiation of a light source to degrade various dyes, including rhodamine B (RhB) and methylene blue (MB), and investigated the reaction pathways leading to the degradation products.[71–73] Both of these dyes are a so-called cationic dyes, meaning that the dye dissociates into a cationic component when dissolved. Regarding the degradation of such dyes, it usually involves the formation of hydroxyls that interact with the dye and as such, the dye dissociates into various side products.

In the case of RhB degradation, Yang *et al.* proposed a reaction pathway based on the side product detection by means of gas chromatography-mass spectrometry (GC-MS).[68] A system of TiO_2 thin films and an aqueous solution of RhB, exposed to UV light, was used in this study. The proposed pathway of RhB degradation is shown in Fig. 11. The *m/z* values represent the peaks in the mass spectra, where *m/z* 443 signifies the initial RhB molecule. The base aromatic ring structure of RhB remains initially intact, whereas the ethyl groups are removed first. Next, decarboxylation takes place at the R-COOH group. The formed hydroxyl radicals (·OH) attack the C=C double bond, inducing a ring opening (represented by *m/z* 154 and 143). While investigating the degradation pathway of RhB, one should consider the reaction conditions, as well as the type of catalyst, since there have been reports of other postulated mechanisms for experiments conducted under different conditions.[70,74] For example, when the reaction medium of dye degradation is water-based, it allows the formation of ·OH radicals, following:

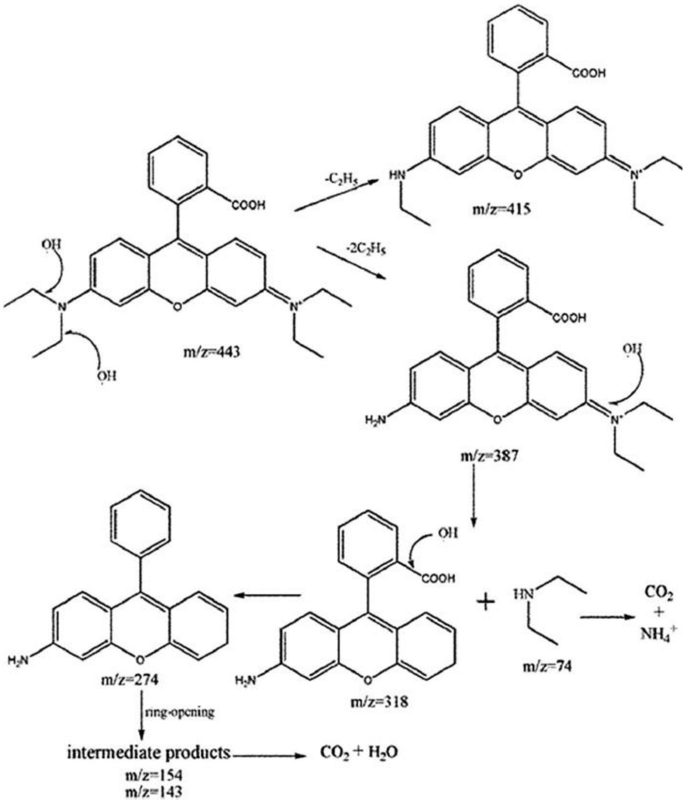

Figure 11. Proposed degradation mechanism of RhB according to Yang *et al.*, with TiO_2 thin films as catalyst (note: *m/z* represents the mass divided by the charge number of the detected molecule in GC-MS).[68]

$$\text{semiconductor} + \text{hv} \longrightarrow \text{h}^+ + \text{e}^- \tag{16}$$

$$\text{H}_2\text{O} + \text{h}^+ \longrightarrow \text{H}^+ + \cdot \text{OH} \tag{17}$$

$$\text{O}_2 + \text{e}^- \longrightarrow \cdot \text{O}_2^- \tag{18}$$

The ·OH radical is considered as a strong oxidant that can easily degrade many organic dyes.[71] However, some examples exist of the absence of hydroxyl radicals during photocatalytic dye degradation. Zhang *et al.* uses a free-radical system of RhB in ethanol using photoactive CABB, postulating the mechanism of:[24]

$$\text{CABB} + \text{RhB} \longrightarrow {}^*\text{RhB} \tag{19}$$

$$\text{CABB} + \text{hv} \longrightarrow \text{h}^+ + \text{e}^- \tag{20}$$

$$\text{O}_2 + \text{e}^- \longrightarrow \cdot \text{O}_2^- \tag{21}$$

$$\cdot \text{O}_2^- + {}^*\text{RhB} \longrightarrow \text{mineralization products} \tag{22}$$

Here, CABB first adsorbs RhB onto its surface, activating the dye molecule (indicated by *RhB, eq. 19). The photogenerated electrons in eq. 20 are captured by O_2 molecules which are present as dissolved species in solution, forming $\cdot O_2^{-}$ radicals (eq. 21). These radicals react with the adsorbed *RhB molecules and subsequently follow a pathway towards mineralization products, as indicated by eq. 22. The term mineralization products is commonly used to describe the formation products of dye degradation. The final mineralization step is relatively fast after the initial RhB activation and the photoexcitation of CABB is also known as a rapid process, making the radical formation the rate-limiting step.[75] Since the radical formation controls the rate of degradation, the reaction rate is independent of the RhB concentration. The RhB concentration can therefore be described by the general linear equation:

$$C_t = C_0 - kt \tag{23}$$

Where C_t equals the concentration of the dye at time t, C_0 equals the initial dye concentration at t=0, and k is the reaction rate, making it a zeroth-order reaction where the RhB concentration decreases linearly.[24]

A similar reaction pathway for the photoinduced degradation of MB is expected since both RhB and MB are both cationic dyes. In a similar study, the photocatalytic degradation of Sudan Red III was tested.[76] The proposed mechanism in ethanol, using a photoactive DP, follows the same steps as described above. In addition, similar reaction kinetics towards RhB, methyl red, and methyl orange degradation were found in this study.

Regarding MB degradation, several reaction pathways have been investigated. Fig. 12 shows a pathway proposed by Houas *et al.*, with TiO_2 powder suspended in an aqueous solution which is irradiated with UV light.[71] Here, the degradation of MB is induced by the formation of hydroxyl radicals in a water-free environment. Interestingly, the degradation of MB with TiO_2 follows first-order kinetics, where the rate of degradation depends on the MB concentration. The difference in order of kinetics when using different photoactive materials could arise from adsorption effects. For example, literature attributes a zeroth-order kinetic to the strong adsorption of sulfosalicylic acid onto a photoactive material, while first-order kinetics only apply to weak adsorptive materials for this molecule.[77] This study has not been extended to relating the adsorption of dyes on the degradation kinetics. However, another study describes a zeroth-order reaction for dyes as a process where the catalyst surface is saturated with the dye, and therefore the rate of degradation is independent of the change in dye concentration.[78]

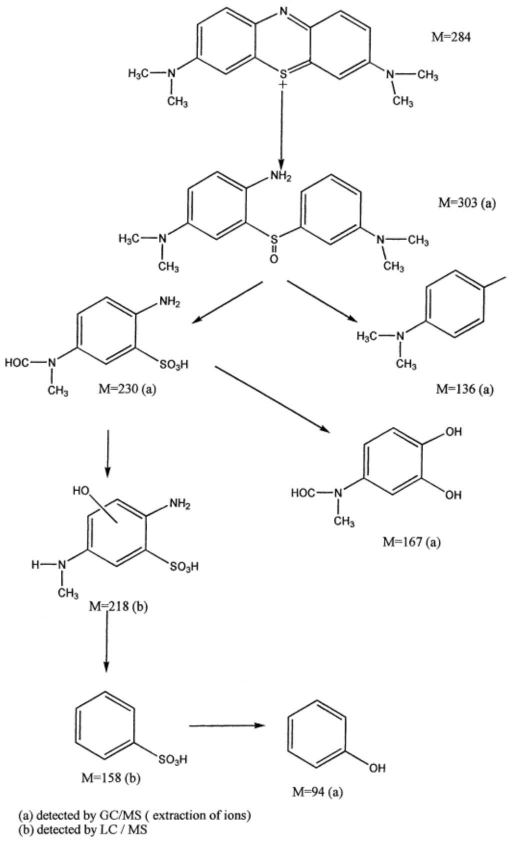

Figure 12. Proposed degradation mechanism of MB according to Houas *et al.*, with TiO_2 powder as catalyst.[71]

So far, we have showed prior art on photochemical dye degradation experiments, revealing that different kinetics of degradation depends on the dye and photoactive material. The discussed studies present valuable information regarding the degradation pathway of RhB and MB. They also demonstrate the purpose of dye degradation experiments in line of a model reaction system to compare the photochemical activity of various photoactive materials. In the next chapter, we will discuss literature on a higher-impact photochemical reaction, namely CO_2 reduction.

2.6 Photochemical CO_2 reduction

In the final theoretical section we will elaborate on one of the "holy grails" of photochemistry, namely CO_2 reduction.[79] In the last few years, photochemistry has focused on tackling the ever-increasing CO_2 pollution of our atmosphere that contributes to the impact on the global climate. Photochemistry is an attractive strategy to partake in converting CO_2 into useful chemicals since the required energy can be harvested from the sun. Depending on the energy that is delivered to the chemical system, CO_2 reduction can follow many different pathways leading to a variety of chemicals. Since we are dealing with reduction reactions, the required potential to drive these reactions should be equal or lower than the bandgap energy of the semiconducting material. Table 1 lists some common reduction reactions related to CO_2. The respective reduction potentials are versus a standard hydrogen electrode (SHE) since these potentials are measured in an electrochemical cell.[2] One may note from Table 1 that the conversion of CO_2 can lead to the formation of other greenhouse gasses, such as CO and CH_4. However, one should also consider that the formation of these chemicals can be of key importance for future industries since CO and CH_4 can either serve as a fuel or as chemical building blocks.[79]

Table 1. A selection of CO_2 reduction reactions with the respective reaction potentials (vs. SHE).[2]

Reduction reactions	E (V) vs. SHE (at pH of 7)
$CO_2 + e^- \rightarrow CO_2^-$	−1.9
$CO_2 + 2H^+ + 2e^- \rightarrow HCOOH$	−0.61
$CO_2 + 2H^+ + 2e^- \rightarrow CO + H_2O$	−0.52
$CO_2 + 6H^+ + 6e^- \rightarrow CH_3OH + H_2O$	−0.38
$CO_2 + 8H^+ + 8e^- \rightarrow CH_4 + 2H_2O$	−0.24

Chen *et al.* performed a computation study on the photocatalytic reduction of CO_2 with CABB as catalyst.[80] Density functional theory (DFT) calculations were used to investigate the adsorption of CO_2 on the CABB surface and how the bandgap of CABB aids in the process of CO_2 reduction. Fig. 13 shows the complicated reduction pathway of CO_2 taking place on the CABB surface, where H^+ and e^- activates the protonation of CO_2. Here, the authors focus mainly on the optimal reaction pathways, following only the energetically most favorable steps leading to the formation of single carbon products (*i.e.*, CO, CH_4, HCOOH, CH_3OH). In this process, CO_2 first adsorbs on a Cs atom site in the structure, where the O atom is most likely to attach to the Cs atom. Energetically, the formation of double carbon bonded products is not favored due to the distance between two adjacent Cs atoms in the CABB crystal structure, where this distance is governed by the halide atom.[80]

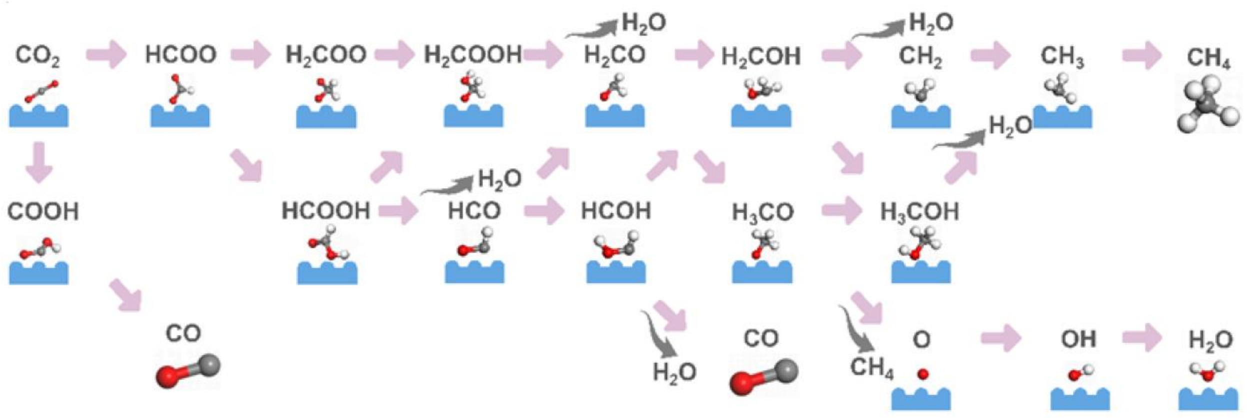

Figure 13. Proposed reduction pathway of CO_2 following the energetically most favorable steps, leading to single carbon products, reproduced from Chen et al.[80]

In terms of experimental studies, there have been limited reports on the use of CABB for the photocatalytic reduction of CO_2.[81–83] One of the first and leading studies in this field is reported by Zhou *et al.*, using CABB NCs in a dispersion medium of ethyl acetate.[7] The authors present the formation of CO and CH_4 as primary reduction species of CO_2, with a yield of 14.1 µmol for CO and 9.6 µmol for CH_4 per gram of catalyst in 6 hours' time, respectively (Fig. 14). This yield is far from the yield that is achieved with defective TiO_2 NCs in water, reaching a CH_4 production of 17 µmol/h/g.[84] The low CO_2 reduction rate with CABB NCs could be due to the lack of protonated species such as water. From Table 1 we can see some redox reactions require the presence of protons (H^+), however ethyl acetate generally does not donate a proton such that these reactions are less likely to take place.

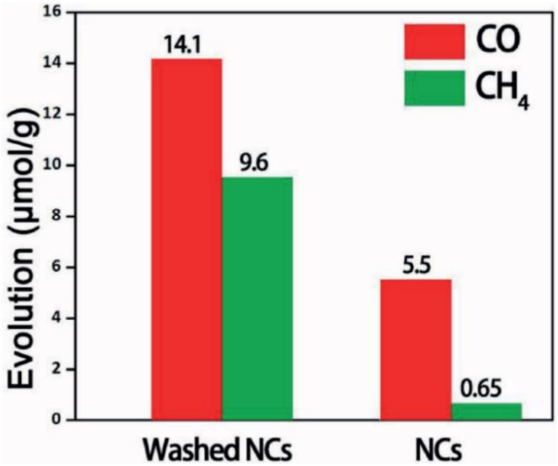

Figure 14. Photocatalytic performance of CABB NCs towards CO_2 reduction, presenting on the evolution of reduction species over the course of 6 hours, reproduced from Zhou *et al.*[82]

Since the field of using CABB for CO_2 photoreduction is relatively new, there has been little insight into the influence of surface chemistry and shape effects, for example. One report, however, describes the photocatalytic reduction of CO_2 using CABB NCs of different shapes.[82] Here, nanoplatelets and nanocubes of CABB were tested, showing that the total yield of CO and CH_4 is approximately 4-fold for nanoplatelets than for nanocubes.[82] This exemplifies the significance of taking the particle shape into consideration when studying the photoactivity.

Chapter 3. DP thin films for CO_2 reduction

This section describes the synthesis method of CABB (and Sb-composite) thin films on glass substrates for photochemical CO_2 reduction, and discusses the main challenges involved. In literature, the most used method to synthesize these films is by dissolving the respective precursor salts in an organic solvent, such as dimethyl sulfoxide (DMSO) or dimethylformamide, and spin coating the resulting solution onto a substrate.[85] Many factors will affect the structural properties of the DP film, such as deposition temperature, spin speed, DP concentration, and annealing temperature.[41,86] In this work, we reproduce the procedure as described by Sirtl *et al*. to obtain CABB thin films with a reproducible coverage and thickness (Chapter 3.1).[87] In Chapter 3.2, we will go deeper into using this method to synthesize Sb-alloyed CABB thin films with varying Sb concentrations. The performance of the DP films towards photochemical CO_2 reduction is tested next (Chapter 3.3). In addition, the fabrication of different charge transport layers, which can improve the charge separation in DP thin film devices, is reported in Chapter 3.4.

3.1 Synthesis and optimalization of CABB thin films

CABB thin films are prepared following a solution-based approach.[87] First, the bromide precursor salts (*i.e.*, CsBr, AgBr, $BiBr_3$) are dissolved stoichiometrically in DMSO, inside a nitrogen-filled glovebox. The resulting DP-solution is spin coated on a clean glass substrate, and the resulting thin film is annealed at elevated temperatures. Fig. 15 shows a graphical representation of this procedure and for a detailed description of the experimental method see Chapter 3.6.2.

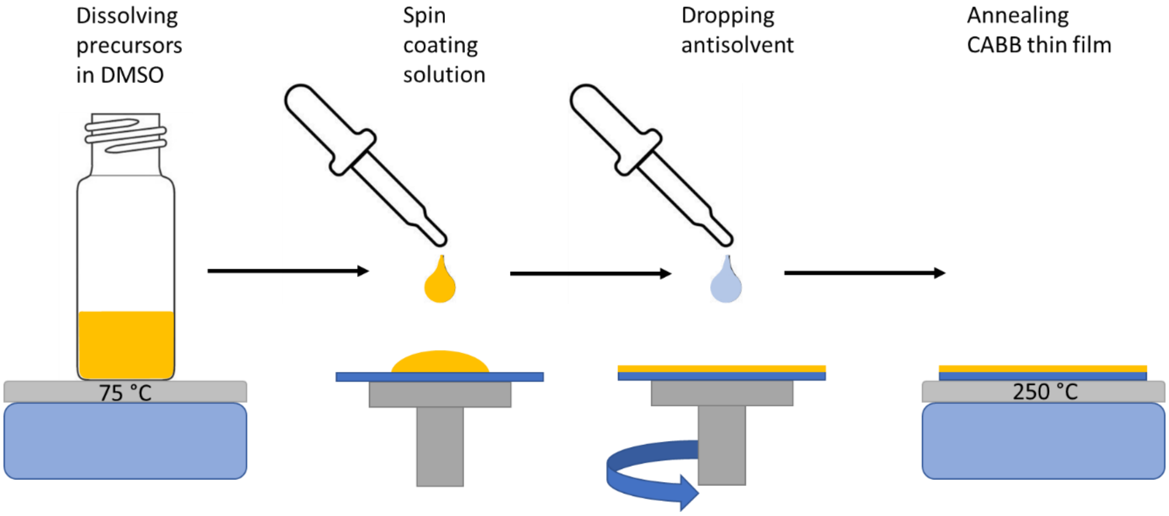

Figure 15. Schematic depiction of the process of spin coating solution-based DPs onto a substrate. First, the bromide precursor salts are dissolved and the DP solution is spin coated. During spin coating, an appropriate amount of antisolvent is added dropwise to initiate crystallization. Lastly, the thin DP film is annealed.

The optical properties of the DP thin films are analyzed with an UV-Vis spectrophotometer equipped with an integrating sphere. As described in the theory (Chapter 2.3), with the use of an integrating sphere the A, R, and T can be determined. R is determined by placing the DP thin film at the back of the integrating sphere. By mounting the DP thin film inside the integrating sphere $R+T$ is determined. A is then calculated following eq. 9.

The A, R, and T of a CABB thin film are shown in Fig. 16. The magnitude of these phenomena strongly depends on the incident wavelength. Since the absorptive characteristics of CABB are already discussed in the theoretical section (Chapter 2.2), we will focus here on the reflectance and transmittance of a CABB thin film. We can base some of our observations on the work of Jöbsis *et al.*, where the optical properties of a CABB thin film are described in detail.[88] The dip in transmittance at 445 nm is commonly described as the excitonic transition between VB and CB at the center of the Brillouin zone (Γ).[89] Without going into further detail, the Brillouin zone can be regarded as the crystal lattice in reciprocal space. Concerning the reflectance, it remains relatively moderate over the entire spectrum, with a few features at distinct wavelengths. These features are a result of the films' dielectric properties and absorption resonances, giving rise to interference effects that govern the nature of the reflectance. The reflectance scales with the dielectric of air, and since it is known that the dielectric function of a material maximizes at a frequency just below an absorption resonance, the feature at 445 nm can be ascribed to the excitonic transition which is also observed in the transmittance.[88] The broad feature in reflectance peaking around 580 nm could be the effect of the absorption resonance that is ascribed to the indirect bandgap of CABB. At higher wavelengths (above 500 nm), the majority of the light is transmitted through the material. In addition, the absorptance drops below zero at a wavelength of 550 nm and higher, which is physically not possible. We hypothesize that when placing the thin film inside the integrating sphere a (small) portion of the light is reflected out of the sphere. If this is the case the contribution of R in $R+T$ is too large, resulting in a negative value for A at higher wavelengths (where A is approximately 0).

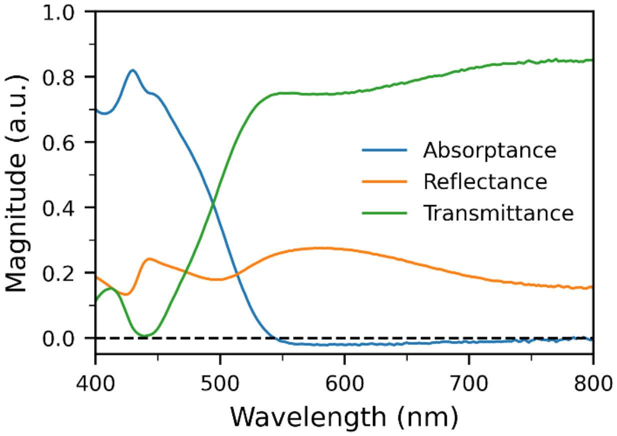

Figure 16. UV-Vis analysis of a CABB thin film, presenting the fractional magnitude of the absorptance, reflectance and transmittance.

Crystallographic analysis is performed to verify the elpasolite crystal structure of the synthesized CABB by comparing it to an elpasolite reference (Fig. 17). The major reflections of the elpasolite structure are also present in the diffractogram of CABB, indicating that the synthesis is successful in obtaining crystalline CABB thin films. The presence of secondary phases which might have formed during the synthesis, such as $Cs_3Bi_2Br_9$, Cs_3BiBr_6, Cs_2AgBr_3 and $CsAgBr_2$, is also studied.[90–92] Since no additional reflections are detected that could correspond to these secondary phases, it can be assumed that the CABB thin film is phase-pure.

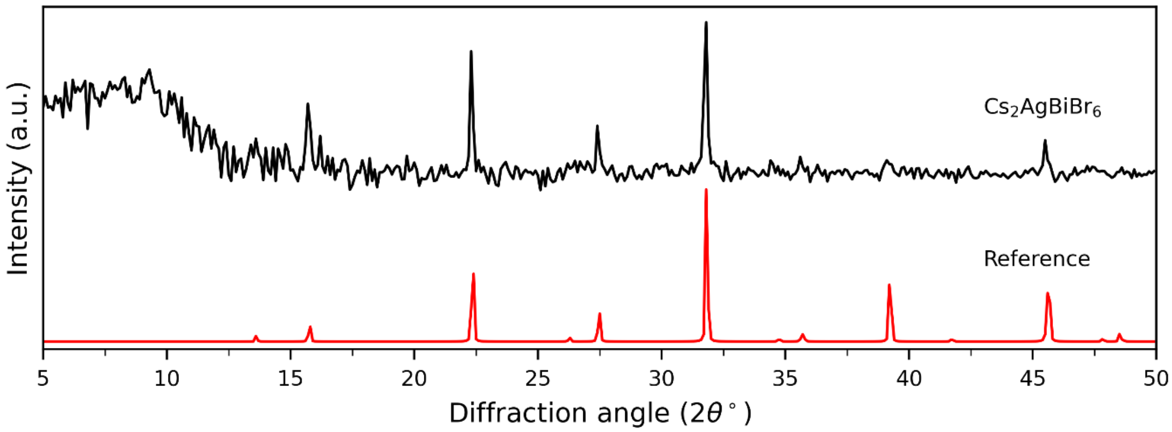

Figure 17. XRD pattern of CABB (black) compared to a reference (red).

However, a high noise to signal ratio together with a broad band is observed in the diffractogram, especially at lower angles. The combination of a high noise and the presence of a broad feature can have a few causes. It might be a result of the sample holder. These thin films are measured while being in an air-tight dome, and the height of the substrate cannot be aligned properly. In essence, the dome compartment should not interfere with the incident X-rays. However, it is key that the samples are aligned with the incident X-rays, especially in the z-direction, otherwise the loss of signal at low diffraction angles could be considerable. However, we cannot assure that the thin films in the dome are aligned with the radiation source. The broad feature might also be due to scattering from either the sample or the glass substrate. It is well-known that crystallite imperfections, in for example glass, can cause intense diffuse scatter.[93,94] In addition, small particles in the order of several nanometers can give rise to X-ray scattering, which is an effect that is often studied with small-angle X-ray scattering.[95] The decrease of crystalline domains leads to the formation of an amorphous phase, causing the broadening of diffraction bands.[96] Since the characteristic reflections of CABB are considered as sharp, the broad band at lower angles is likely from an amorphous secondary phase which formed during the synthesis or from the misalignment of the sample.

In addition to crystallography, AFM measurements on CABB thin films are performed to determine the film thickness and to analyze the surface morphology. The left side of the image in Fig. 18a) shows a scratch made with a syringe needle to determine the thickness, which is around 210 nm. Interestingly, the film has a rather irregular surface covered with holes, which is verified by considering the height differences across the film surface, as shown in Fig. 18b). The surface profile reveals height differences in the 100 nm regime, which is considerable for thin films. Further analysis of the surface profile allows to determine the surface roughness of the thin film, which is expressed as the root mean square (RMS) roughness. A RMS roughness of approximately 42 nm is found, while values below 25 nm are not uncommon.[5,88] These characteristics show that the CABB grains are not densely packed on the substrate which is indicative of inadequate crystallization.

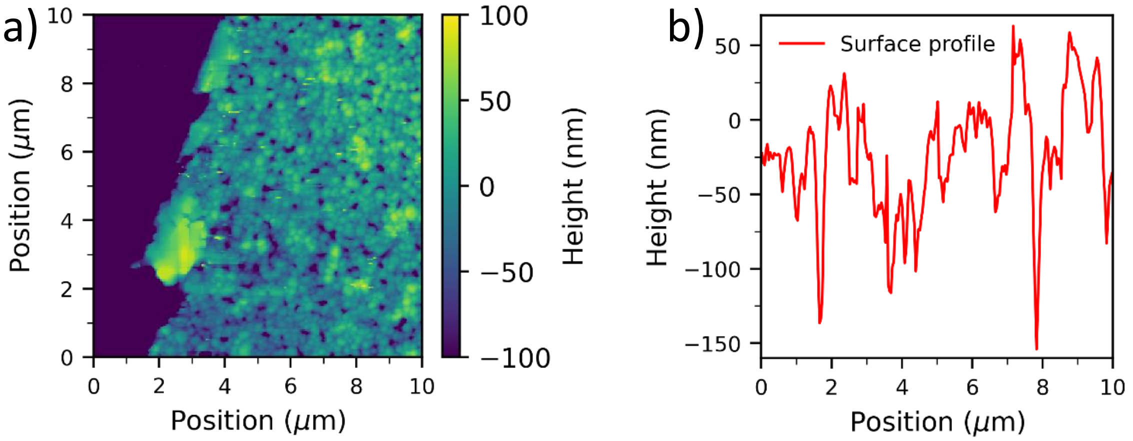

Figure 18. AFM measurement of a CABB thin film. **a)** AFM image of a CABB thin film surface. **b)** Surface profile of a CABB thin film, illustrating the height differences across the surface.

According to literature, the dropwise addition of an antisolvent during the DP spin coating initiates the immediate crystallization of the DP, increasing the grain packing density and thus improving the quality of the film as compared to without antisolvent.[5,85] To improve the quality of our CABB thin films, isopropanol is added dropwise during the CABB spin coating.

By employing this approach, a visual difference is revealed between a CABB thin film synthesized without (opaque) and with (transparent) antisolvent, as shown in Fig. 19. Regarding the optical properties, the *R*+*T* is measured of both CABB films by placing them at the back of the integrating sphere, and the *A* is calculated from these fractions. Even though the films have a different appearance concerning the transparency, there is no significant difference in the calculated *A* between a CABB thin film spin coated with and without antisolvent, as shown in Fig. S1. One might expect that the poor surface coverage of the thin film without antisolvent gives rise to a significant scattering effect of light, leading to a different absorption profile for these films. However, since both films are measured in an integrating sphere the scattered light is also collected by the detector. Hence, the effect of light scattering is included in these measurements, leading to similar absorptance profiles for a CABB thin film spin coated with and without antisolvent.

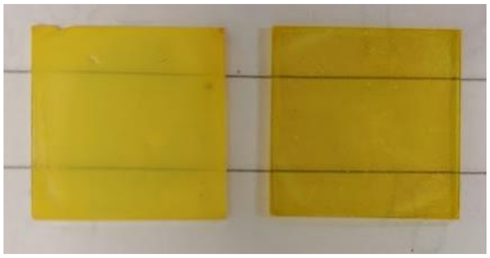

Figure 19. Image of CABB spin coated without (left) and with (right) antisolvent.

AFM measurements show that the addition of isopropanol during spin coating improves the surface coverage and leads to an enhanced surface smoothness of the CABB film (Fig. 20a). The crystal grains are more uniform in size and cover nearly the entire surface, leading to a high grain packing density. The film thickness of CABB spin coated with antisolvent is approximately 180 nm, which is in the same order of magnitude as the film thickness of CABB spin coated without antisolvent. Having a similar film thickness but a visually different reflection (transparent versus opaque) of films spin coated with and without antisolvent is a clear indication of an improved smoothness and coverage of the film. Indeed, the RMS of the sample with antisolvent is considerably lower than without antisolvent. The RMS roughness of a CABB thin film spin coated with antisolvent is approximately 8.8 nm, which is a significant reduction of the RMS compared to the lower-quality thin film analogue. The smoothness of the high-quality CABB thin film is demonstrated in Fig. 20b), revealing the small deviation in height when crossing the films' surface.

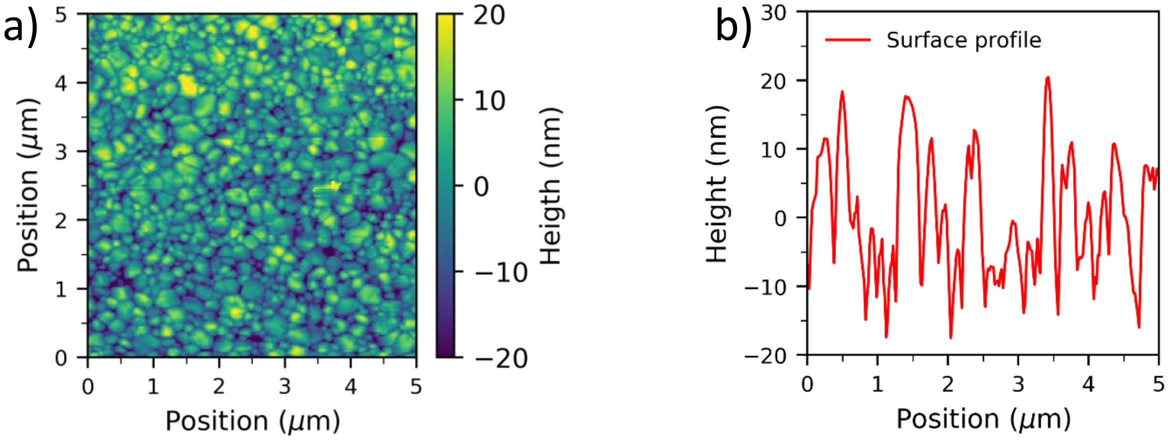

Figure 20. AFM measurement of a CABB thin film spin coated with isopropanol. **a)** AFM image of the respective CABB thin film surface. **b)** Surface profile of the respective CABB thin film, illustrating the height differences across the surface.

3.2 Synthesis of $Cs_2AgSb_xBi_{1-x}Br_6$ (x=0.00, 0.125, 0.25, 0.375, 0.50, 0.75, 1.00) thin films

We explore the synthesis of Sb-alloyed thin films, commonly expressed as $Cs_2AgSb_xBi_{1-x}Br_6$ (Section 3.6.2 for the detailed synthesis procedure). Our aim is to synthesize a collection of Sb-alloyed CABB thin films with Sb concentrations of 0%, 12.5%, 25%, 37.5%, 50%, 75% and 100%, respectively. According to literature, the annealing temperature of Sb-containing films should be lowered from 250 °C (for CABB) to a range of 90–150 °C to reduce the formation of undesired side phases.[8,9,90] For the synthesis of the above-mentioned Sb-alloyed CABB thin films, we follow the procedure as described in previous paragraph, but lower the final annealing temperature to 130 °C.

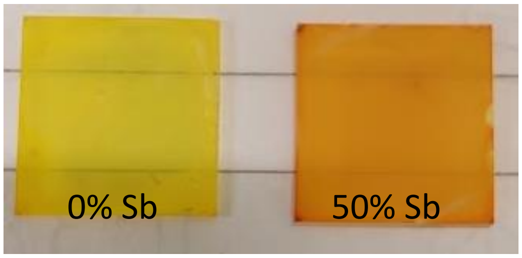

Figure 21. Images of thin films of $Cs_2AgBiBr_6$ (left) and $Cs_2AgSb_{0.50}Bi_{0.50}Br_6$ (right).

The alloying of Sb^{3+} into the crystal structure of CABB alters the optical properties of thin films. To demonstrate the color change, a CABB and 50% Sb-alloyed CABB thin film, both synthesized without antisolvent, are visually compared in Fig. 21. The exchange of Bi^{3+} with Sb^{3+} causes an increase of the VB maximum by higher energy 5s states of Sb, leading to a decreased bandgap energy, as was discussed in Chapter 2.2.[51] This is observed as a redshift in *A* with increased concentration of Sb^{3+}, as can be seen in Fig. 22a). Note that these spectra are all normalized at the absorptance maximum of CABB (at 440 nm), which allows to better visualize the redshift in *A*. Without normalization the intensity of *A* decreases upon increasing the Sb^{3+} alloying concentration, indicating that the surface coverage and/or thickness decreases. The hypothesis of decreasing surface coverage with increasing Sb^{3+} concentration is discussed later in this chapter. The film thickness is not measured, however. One should notice that similar to what is observed for CABB, the Sb-alloyed DP thin films also show a negative signal in absorptance above 550 nm. We postulate that an effect, comparable to what is described before, contributes to

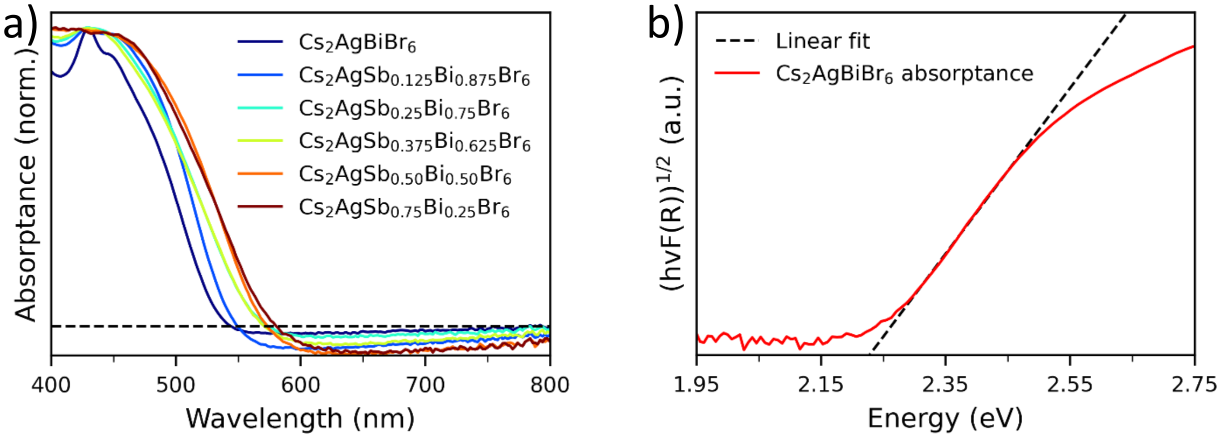

Figure 22. UV-Vis analysis of $Cs_2AgSb_xBi_{1-x}Br_6$ thin films, with **a)** the normalized absorptance of Sb-alloyed DP thin films, revealing the redshift with increased Sb^{3+} concentration. **b)** Tauc plot of CABB to estimate the bandgap energy.

the negative A. Thus, a small portion of the incident light is reflected out of the integrating sphere during the measurements, increasing the contribution of R in $R+T$, and consequently obtaining a lower value for A.

The effect of Sb-alloying on the change in bandgap energy is also investigated. Here, the bandgap energy of a semiconducting material can be approximated by using a so-called Tauc plot.[97] Note that using a Tauc plot to determine the bandgap energy can be considered controversial, since this method strongly depends on the data processing of the user.

The controversy is demonstrated in the following description of the Tauc plot method. Here, the absorptance wavelengths, determined with UV-Vis, are converted to energy in eV. Depending on the transition (direct or indirect), the absorptance is transformed by a power component. For indirect bandgap materials, such as CABB, the A is considered by a power of ½.[97] Next, the sloped linear part of A is fitted with a linear regression. The interception point of the horizontal axis and linear regression indicates the approximated bandgap energy of the material. Fig. 22b) shows an example of the linear part of the A of CABB combined with the linear regression and the interception point. The bandgap energies of $Cs_2AgSb_xBi_{1-x}Br_6$ (x=0, 0.125, 0.25, 0.375, 0.5, 0.75) are listed in Table 2. As expected, the bandgap energy decreases with increased Sb^{3+} concentration.

Table 2. Bandgap estimations of $Cs_2AgSb_xBi_{1-x}Br_6$, acquired from Tauc plots.

Perovskite composite	Bandgap energy (eV)
$Cs_2AgBiBr_6$	2.23
$Cs_2AgSb_{0.125}Bi_{0.875}Br_6$	2.16
$Cs_2AgSb_{0.25}Bi_{0.75}Br_6$	2.09
$Cs_2AgSb_{0.375}Bi_{0.625}Br_6$	2.06
$Cs_2AgSb_{0.50}Bi_{0.50}Br_6$	2.05
$Cs_2AgSb_{0.75}Bi_{0.25}Br_6$	2.00

Crystallography analysis of the Sb-alloyed CABB films is performed by means of XRD. The XRD patterns are compared to a reference of the elpasolite crystal structure of CABB to verify if the elpasolite crystal structure is maintained upon Sb-alloying (Fig. 23a). The major reflections of the elpasolite structure are present in the diffractograms of Sb-alloyed DP films, suggesting that the synthesis of Sb-based DP thin films is successful. Similar to what is observed for CABB, a high noise to signal ratio as well as a broad diffraction band is present in the diffraction patterns of the

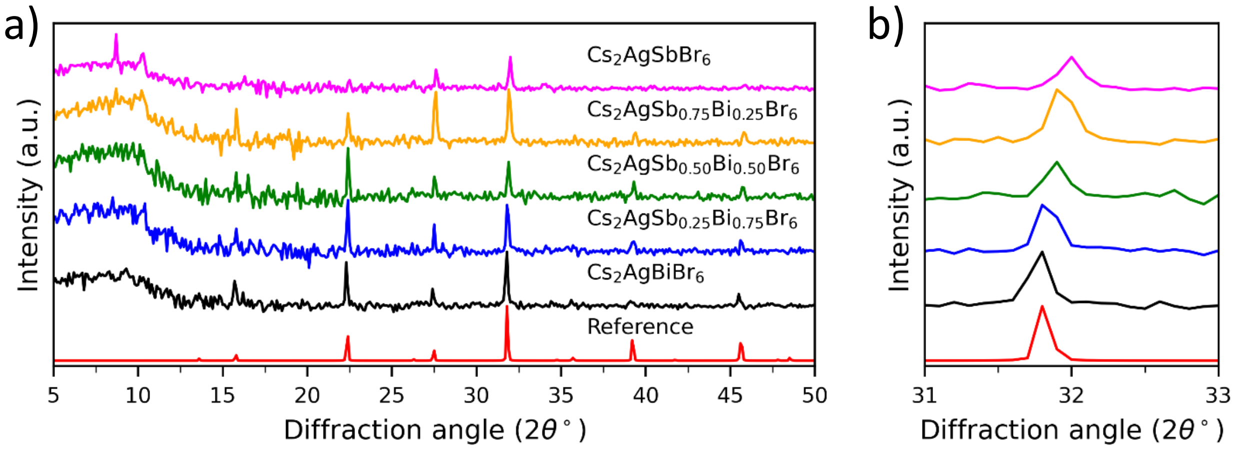

Figure 23. a) XRD patterns of a selection of composite DPs compared to a reference. **b)** Inset of one of the major diffraction peaks around 31.8° 2θ to illustrate the diffraction shift to higher angles with increased Sb-alloying.

Sb DP analogues. These features are likely to have the same origin as for CABB, as was suggested in previous chapter. In addition to analyzing the crystallinity of the DP thin films, the presence of secondary phases, such as $Cs_3Sb_2Br_9$, $Cs_3Bi_2Br_9$, Cs_3SbBr_9, Cs_3SbBr_6, Cs_3BiBr_6, Cs_2SbBr_6, Cs_2AgBr_3 and $CsAgBr_2$, is also studied.[90–92] In case of $Cs_2AgSbBr_6$ (CASB) some diffraction peaks are not present compared to the reference. Notably, the peak at 22.4° and 45.6° 2θ are missing, indicating that this DP thin film might not be phase-pure. The synthesis of DP films with increasing Sb^{3+} concentration proves to be more challenging since an undissolved solid remains in a mixture during the synthesis of the corresponding Sb-alloyed DP. Noteworthy, this solid phase is filtered out prior to the spin coating (see experimental details, Chapter 3.6.2), and hence the stoichiometric ratio of precursors to form the desired DP cannot be preserved, consequently giving the opportunity for other side phases to form. From the secondary phases that are listed above, Cs_3BiBr_6 has diffraction angles close to peaks that are found in the CASB sample at 8.7° and 10.3° 2θ, respectively (Fig. S2). This strongly suggests that the solution-based synthesis does not yield phase-pure DP thin films when the Sb^{3+} alloying is increased.

In addition to checking the crystallinity of the samples, the modest shift in diffraction angles that can be observed from XRD analyses with increasing Sb-alloying concentration is investigated. Fig. 23b shows a zoom-in of the XRD-diffractogram around 32° 2θ. It follows that upon increasing the Sb content the peak shifts to larger diffraction angles. This can be explained by the fact that Sb^{3+} is a smaller ion than Bi^{3+}. The replacement of Bi^{3+} by Sb^{3+} causes the crystal unit cell to contract, following Bragg's Law, as was explained in the theoretical section (Chapter 2.4). The lattice constant can be subsequently calculated from eq. 13:

$$a = n\lambda \frac{1}{2\sin\theta}\sqrt{h^2 + k^2 + l^2} \tag{13}$$

The reflection peak around 31.8° 2θ is used to calculate the lattice constant for each of the DP films. Fig. 24 shows the decreasing trend in lattice constant with increasing fraction of Sb into CABB. The shrinking lattice constant follows a linear trend which is indicative of the full incorporation of Sb^{3+} into the crystal lattice.[98] Non-linear behavior would suggest that not all the Sb^{3+} is incorporated in the elpasolite structure but that it is rather forming side phases or is remaining as part of the $SbBr_3$ reactant. Even though the linear decrease of the lattice constant suggests that Sb^{3+} is fully incorporated into the DP alloys, XRD did also reveal that increasing the Sb^{3+} alloying concentration results in the formation of side phases, with the most likely candidate Cs_3BiBr_6. Hence, we hypothesize that the majority of Sb^{3+} does indeed incorporate into the lattice of the elpasolite crystal structure, whereas a fraction of some of the other components (e.g., Cs^+, Bi^{3+}, and Br^-) form the secondary phase.

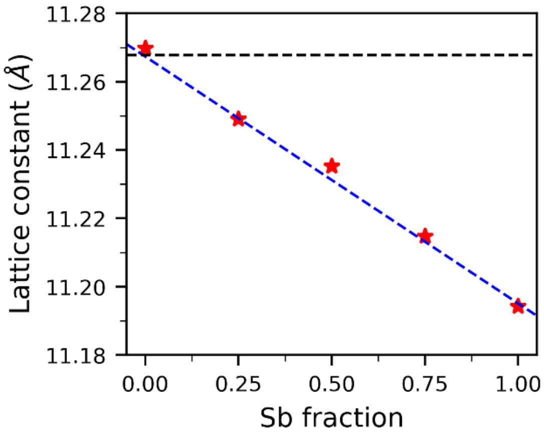

Figure 24. Plot of the mean lattice constants of Sb-alloyed CABB thin films, revealing that the lattice constant decreases linearly with increasing Sb concentration.

In addition to crystallography analysis, SEM analysis is performed on the synthesized thin films to investigate the surface coverage, which is an important factor to consider when thin films are being used for photochemical reactions.[99] We confirm with SEM, as shown in Fig. 25, that the surface coverage of Sb-alloyed DPs decreases as the alloying concentration increases. The images reveal that the crystal grains are less packed for $Cs_2AgSb_{0.25}Bi_{0.75}Br_6$ (Fig. 25b) compared to $Cs_2AgBiBr_6$ (Fig. 25a). One can even conclude that the grains are nearly fully separated from each other when the concentration of Sb^{3+} increases even further as is the case for $Cs_2AgSb_{0.75}Bi_{0.25}Br_6$ (Fig. 25c). This supports the hypothesis of a decreasing absorptance due to a lowering of the surface coverage as the Sb-concentration increases, as was postulated earlier with UV-Vis analysis.

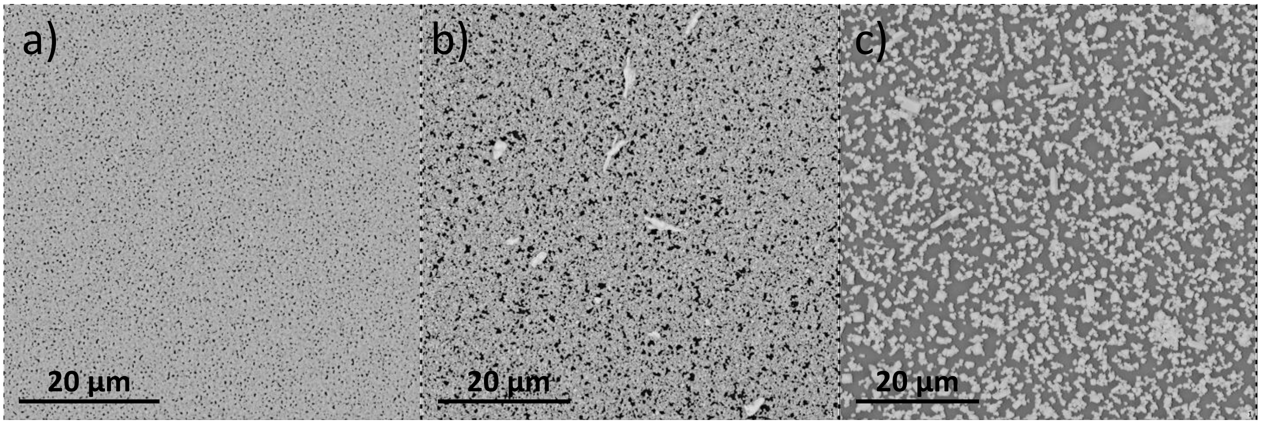

Figure 25. SEM micrographs of $Cs_2AgSb_xBi_{1-x}Br_6$ thin films, with a composition in the form of **a)** $Cs_2AgBiBr_6$, **b)** $Cs_2AgSb_{0.25}Bi_{0.75}Br_6$ and **c)** $Cs_2AgSb_{0.75}Bi_{0.25}Br_6$.

Next to structural analysis, the stoichiometric composition of the alloyed thin films is analyzed with SEM-EDX. This technique gives additional information on the distribution of elements across the film surface. Analysis shows that the distribution of elements is homogeneous on the surface of the thin films, independent of Sb-alloying concentration. The ratio of elements, however, does not correspond entirely to the used stoichiometry in the synthesis. In the case for Sb-alloyed DP thin films, the concentration of Br^- and Bi^{3+} are noticeably higher, while Cs^+, Ag^+, and Sb^{3+} are below their expected percentage. It should be noted that EDX has some disadvantages compared to other elemental analysis techniques such as inductively coupled plasma (ICP). The sample coverage, homogeneity, and other surface effects play a key role in the accuracy of EDX, while ICP analyzes the entire sample depth with a lower detection limit.[100,101] ICP would allow to not only measure the sample's surface but penetrate deeper into the film, which would give a better representation of the film composition. Since the discrepancy of the elemental compositions observed with EDX is relatively constant for every sample, it can be assumed that indeed Br and Bi are overrepresented and Cs, Ag and Sb are underrepresented in the EDX analysis.

3.3 Activity tests for CO_2 reduction

After successfully lowering the bandgap of the CABB thin films via Sb-alloying, the photochemical activity towards CO_2 reduction is studied. These experiments are performed in an airtight cell coupled to gas lines which are directed to an online GC system equipped with a methanizer. The gas lines and cell are first flushed with N_2 to remove reactive species, after which CO_2 and H_2 are flushed through before every measurement. This is done to prevent any side reactions or interferences with species other than CO_2 and H_2. The GC chromatograms are updated approximately every 4 minutes, and the light source to excite the photoactive material is turned on after stabilization of the signal output. For details on the experimental setup, see Chapter 3.6.2.

The first CO_2 reduction experiments are conducted with a CABB thin film that is made without antisolvent addition during the spin coating process. As discussed in the theoretical section, we expect the formation of reduction species of CO_2, such as CO and CH_4, which can be detected with the GC setup. By illuminating the sample at AM1.5, no CO or CH_4 is observed over the course of several hours. AM stands for air mass, which is a measure for the path length of sunlight before hitting the earth's surface. This measure scales with the intensity of the incident light, where the mean irradiance of AM1.5 corresponds to approximately 1 kW/m^2.[19] The absence of CO or CH_4 suggests that either no CO_2 is reduced, or the reduced CO_2 species concentration is below the detection limit of the system. In case of the latter, we attempt to achieve higher reduction rates by using a higher-quality CABB thin film which is spin coated with antisolvent. The enhanced surface coverage and increased grain sizes should aid in the photochemical reduction of CO_2.[86] Next to using a more promising thin film, a different light source is used that provides photons matching the bandgap energy of CABB, thus a greater portion of the incident light can be absorbed by the DP. A blue light source is used, emitting at a wavelength of 455 nm (see blue curve in Fig. S3 for the spectral range), closely matching the absorption maximum of CABB around 440 nm. We find that by irradiating the enhanced CABB sample for 60 minutes under a CO_2/H_2 atmosphere yields no reduction species.

Since no significant concentration of either CO or CH_4 is detected, the continuous flow system is changed to a quasi-batch reactor system. Here, the system is flushed with a CO and H_2 mixture. Next, the flow is stopped and the DP thin film is exposed to 455 nm light for 45 minutes. After the irradiation, a slow flow of N_2 at 0.2 mL/min is initiated. This quasi-batch process allows for a longer reaction time of the gases inside the cell and for a build-up of reduction products of CO_2. In this instance, a peak of CO appears in the chromatogram at 0.88 minutes (Fig. 26a). A zoom-in on the respective peaks illustrates how the CO peak quickly rises and then decreases again (Fig. 26b). A peak around 0.66 minutes presents itself that follows a similar trend as CO by a quick rise and decay. Unfortunately, we are unable to identify the compound that corresponds to this retention time, but it is hypothesized that this is one of the many CO_2 reduction products, as was discussed in Chapter 2.6. To identify this compound, one can use for example nuclear magnetic resonance spectroscopy.[102] However, since the identification of unknown species is beyond the scope of our work, we do not go deeper into identifying this species. In Fig. 26c) the intensity maximum of the CO peak at different time intervals is revealed. As mentioned before, the intensity quickly rises after flowing N_2 gas, but the intensity then significantly drops, after which the intensity decay follows a linear rate due to dilution of the initial reaction mixture.

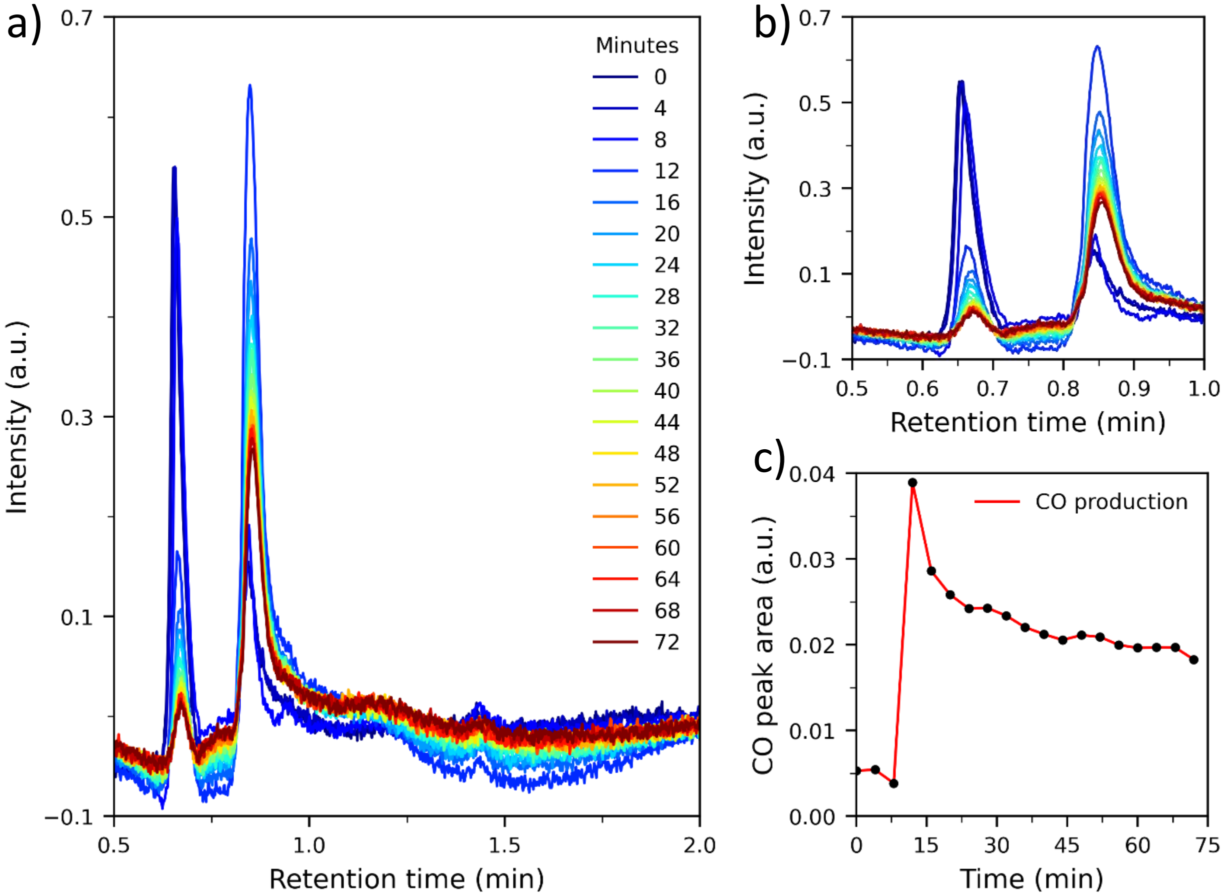

Figure 26. Overview of GC measurements of CO_2 reduction with CABB thin film under 450 nm light illumination. **a)** Chromatogram CO_2 conversion, showing the evolution of the CO peak around 0.85 minutes. **b)** Inset of the unknown peak around 0.66 minutes and the CO peak. **c)** Representation of the rise and decay of the CO peak, plotted as the CO peak area as a function of time.

To observe the effect of CABB on the photoactivity towards CO_2 reduction, we perform experiments with an empty cell and with a clean glass substrate mounted inside the cell. Here, the cell is flushed with N_2 prior to flushing it with reactants CO_2 and H_2. The flow is stopped, 455 nm light is irradiated onto the sample cell, and after 60 minutes a flow of 0.2 mL/min N_2 is passed through the cell. Similar to the CO_2 reduction experiment with a CABB thin film, a CO peak appears in the chromatogram of an empty cell and the cell containing the clean glass substrate. Both chromatograms are shown in Fig. 27.

We anticipate no evolution of CO for the control experiments. However, the rise of a CO peak illustrates that the absence of our DP thin film yields a comparable result as in the presence of the thin film. It is assumed that the rise of a CO peak is due to the presence of a photoactive contamination in the cell, driving the photochemical CO_2 reduction and produces CO species. Even though the cell is flushed with an inert gas and with reactant gases before every measurement, it is likely the cell was not properly manually cleaned beforehand and therefore contained residue of a photoactive material. We have not explored this matter in more detail due to the extensive usage of the solar simulator setup by other users, obstructing us in continuing the measurements with thin films. But more importantly, the low CO formation that is observed with the photoactive DP thin films encourages us to use a different photochemical system for testing DP materials (Chapter 5). Before the focus is shifted towards the new photochemical reaction, we give a brief elaboration in the next chapter on the use of charge transport layers to enhance the charge separation, which would lead to an enhanced photochemical activity.

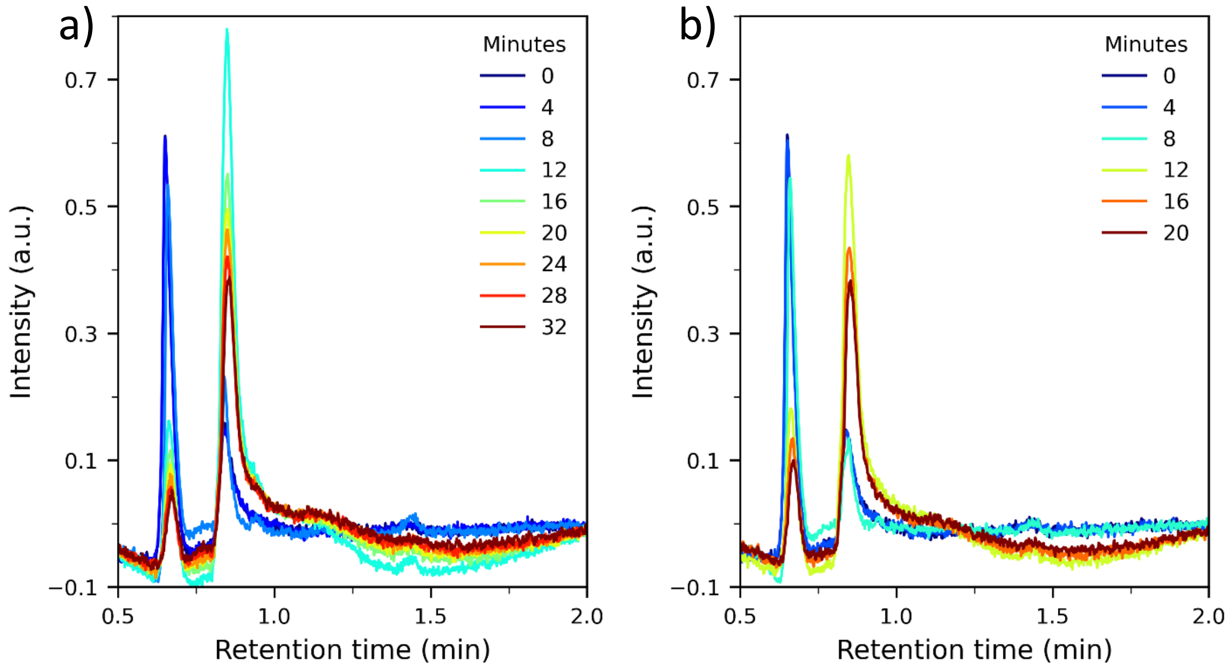

Figure 27. Overview of GC control measurements of CO_2 reduction with **a)** a clean substrate and **b)** an empty cell. Both control measurements show the rise and decay of a CO peak, and a peak of an unknown species around 0.66 min.

3.4 Synthesis of charge transport layers (TiO_2, NiO_x, ZnO)

Since the CABB thin films show no detectable activity towards CO_2 photoreduction, we give an outlook regarding the usage of charge transport layers, showing some preliminary results on the synthesis of TiO_2, NiO_x, and ZnO, respectively. These materials are often used in photoconversion and photovoltaic devices to improve charge carrier separation and consequently decreasing charge recombination losses.[103] By creating a sandwiched structure of HTL–DP–ETL, photogenerated charge carriers can be efficiently used for photochemical reactions taking place at the film surface. In this section we will discuss a selection of transport layers, that is TiO_2, NiO_x, and ZnO as possible materials to improve the photochemical activity of our DP samples and give a brief outlook on the use of these metal oxides in photochemical devices.

The above-mentioned three metal oxides are formed from the hydrolysis and condensation of their respective metal salt or metal alkoxide. The resulting colloidal suspensions are spin coated onto clean glass substrates. The TiO_2 and NiO_x films are annealed at elevated temperatures to form the final metal oxide thin films. For a detailed synthesis procedure of TiO_2, NiO_x, and ZnO thin films see Chapter 3.6.2.

The images in Fig. 28 represent the semiconductor thin films of NiO_x, TiO_2 and ZnO. The NiO_x film is made by a sequence of six spin coating cycles, resulting in an uneven looking film surface. The single layered TiO_2 film has high reflectivity, whereas the ZnO thin film is rather opaque.

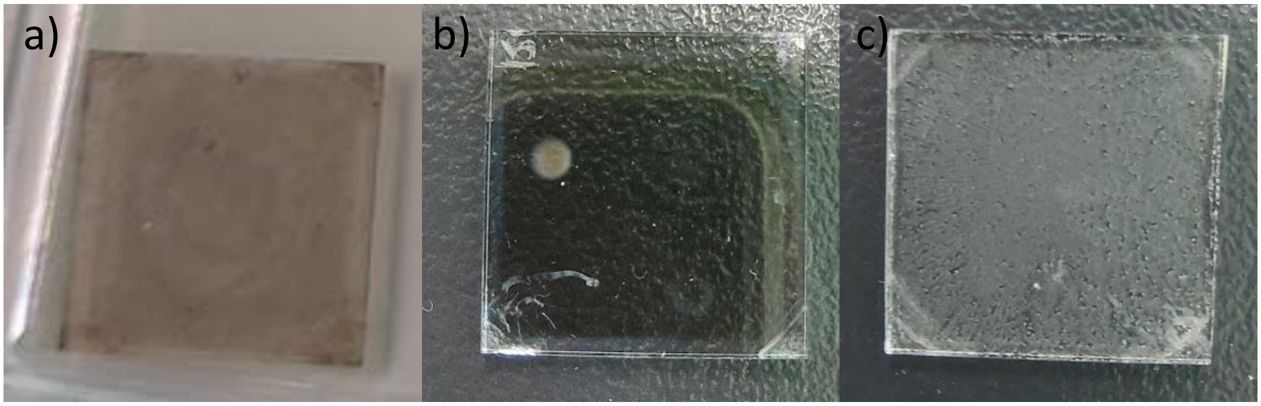

Figure 28. Images of **a)** NiO_x, **b)** TiO_2, and **c)** ZnO thin films.

UV-Vis spectroscopy is used to characterize the NiO_x thin film, as shown in Fig. 29. The absorption spectra of TiO_2 and ZnO are not recorded, but similar to NiO_x both semiconductor materials have a strong absorption in the UV-region, as is described in literature.[104,105] It is of paramount importance that the charge transport layers do not interfere with the visible light absorption of the DP, since this would limit the photoactivity of the device.

In addition to optical characterization, the crystallinity of the TiO_2 and NiO_x thin films is analyzed with XRD. However, no diffraction peaks are observed for the TiO_2 and NiO_x films (Fig. S4). Since XRD is a surface penetrating technique, it is plausible that the films are not sufficiently thick enough for the XRD to detect characteristic crystal planes of these materials. For future research, to obtain useful diffractograms for sample characterization, the integration time of the measurements should be significantly increased.

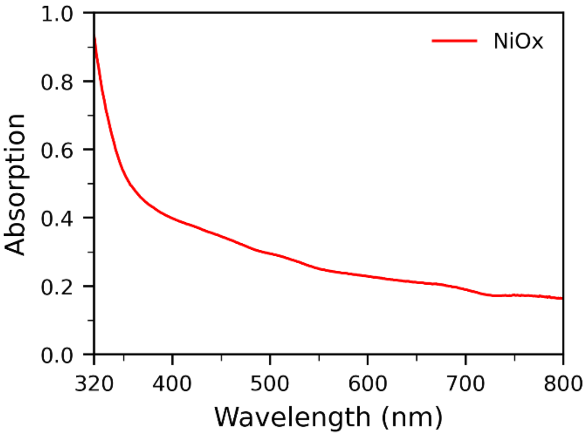

Figure 29. UV-Vis spectrum of a six-layer spin coated NiO_x thin film, illustrating its high absorption in the UV region.

Since the surface of the TiO_2 film is visually reflective, it indicates a low roughness of the film. The roughness of the surface is analyzed with AFM. The film thickness, being approximately 40 nm, is determined by mapping the difference between a scratched surface and the film layer, as shown in Fig. 30a). This image contains so-called scars which are visible as horizontal lines. These line defects can either be a consequence of a high scanning rate or by contamination (*e.g.*, dirt or dust) on the tip probe. A higher magnification measurement is performed to obtain Fig. 30b), showing very little deviation in the surface height, and the RMS roughness is determined to be around 1.8 nm. The texture-like image could also resemble noise from the measurement, which is not verified in this work. The zoomed-in image is used to obtain the surface profile in Fig. 30c), revealing height differences of only 4 nm above and below the average. The smooth surface and according to literature the low absorption in the visible spectrum are promising characteristics for the use of TiO_2 as ETL in a photochemical device. However, the high annealing temperatures that are required to form the TiO_2 will decompose the CABB layer underneath.[106]

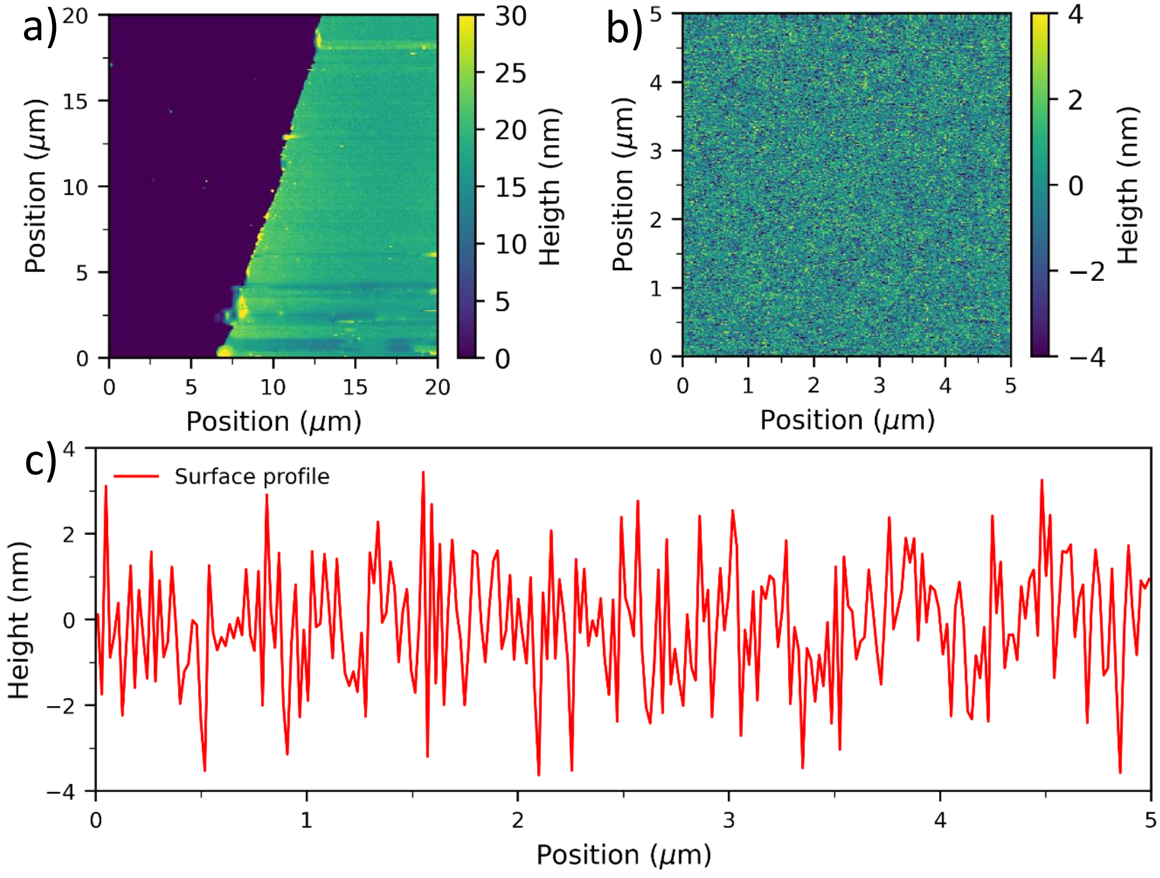

Figure 30. AFM measurements of a TiO_2 thin film, **a)** for film thickness determination, **b)** to determine the smoothness of the surface and **c)** gives an impression of the surface profile of a TiO_2 thin film.

3.5 Conclusions

We demonstrate that the quality of (Sb-alloyed) CABB thin films can be optimized by the addition of an antisolvent during spin coating, initiating immediate crystallization of the DP. This increases the surface coverage and reduces the surface roughness of the DP film surface significantly, as is confirmed with AFM and SEM analysis. $Cs_2AgSb_xBi_{1-x}Br_6$ thin films with Sb-alloying concentrations ranging from 0% to 100% are successfully synthesized. The linear shift of reflection angles determined from XRD measurements reveals that the incorporation of Sb^{3+} into the elpasolite crystal lattice is successful going from CABB to CASB. Crystallography analysis reveals that the CASB thin film is not phase-pure however, and we suspect that Cs_3BiBr_6 is the main contributor to the secondary phase. It is postulated that the majority of the Sb^{3+} is located in the DP structure, whereas a fraction of Cs^+, Bi^{3+}, and Br^- forms the Cs_3BiBr_6 side phase.

Our objective is to investigate the effect of the bandgap energy of CABB on the photochemical activity. In this chapter we discussed our attempt to reduce CO_2 and to study the effect of Sb^{3+} alloying on the activity. During this process some issues came to light. First, since we are limited in manipulating the bandgap via the solution-based synthesis due to the formation of side phases, we opt to direct our attention to a different synthesis approach, which will be discussed in Chapter 4. Second, due to the low formation concentration of CO_2 reduction species (*i.e.*, CO and CH_4) it is challenging to compare the photochemical activity of DP thin films with varying bandgap energy. Hence, we will explore different photochemical reactions which allows us to observe the effect of bandgap manipulation on the photoactivity of DPs (Chapter 5).

As an outlook, we have also briefly explored the possibility of employing charge transport layers into our DP thin films to enable better charge separation. Preliminary results of optical and surface characterization reveal that the spin coating process of NiO_x, ZnO and TiO_2 onto glass substrates is successful. However, the high annealing temperature of TiO_2 would decompose the DP film underneath, making this ETL unsuitable. The NiO_x HTL and ZnO ETL might be suitable for their use in a DP device, but their effectiveness during CO_2 reduction was not tested due to the presence of a contaminated photoactive material in the reaction cell. Further investigation of these transport layers with an optimized system to photochemically reduce CO_2 and detect its reducing species should be performed.

3.6 Experimental details

3.6.1 General information

All chemicals were used as received without any further purification. CsBr (99.999%), AgBr (99.998%), $BiBr_3$ (99%) and $SbBr_3$ (99.999%) were purchased from Alfa Aesar. Isopropanol (technical grade) was purchased from Acros Organics. Dimethyl sulfoxide (>99.9%), titanium butoxide (99%), $Ni(NO_3)_2 \cdot 6H_2O$ (99.9999%), 2-methylimidazole (99%), KOH (90%), chlorobenzene (99.8%) were purchased from Sigma-Aldrich. Ethanol (>99.9%), acetone (99.9%) and methanol (99.85%) were purchased from VWR Chemicals. HCl (≥37%) and zinc acetate dihydrate were purchased from Honeywell Fluka and Supelco, respectively. All borosilicate substrates mentioned in the upcoming sections were cleaned by the following protocol. First, the substrates were brushed clean using common dish soap and a toothbrush. Next, the substrates were placed in a solution of acetone and sonicated (Branson 2800 Cleaner) for 15 minutes, followed by 15 minutes of sonication in isopropanol. A filtered stream of compressed air was used to dry the substrates between every cleaning step. Organic contaminants remaining on the substrates were removed by a UV-ozone treatment (Ossila UV Ozone Cleaner) for 120 minutes. Unless mentioned otherwise, thin film samples were synthesized in a nitrogen-filled glovebox with H_2O and O_2 levels around 0.6 and <0.1 ppm, respectively.

3.6.2 Methods

Preparation of $Cs_2AgSb_xBi_{1-x}Br_6$ solution – In a typical synthesis, 1.5 mmol (319 mg) CsBr, 0.75 mmol (141 mg) AgBr and 0.75 mmol (337 mg) $BiBr_3$ were mixed in 1.5 mL DMSO. By heating at 75 °C and stirring at 700 rotations per minute (RPM) all the reactants dissolved within 1 hour to form a 0.5 M CABB solution. For $Cs_2AgSb_xBi_{1-x}Br_6$ samples, the amount of CsBr and AgBr were kept the same as for CABB, but the ratio of $BiBr_3$ and $SbBr_3$ were varied according to the respective stoichiometry (x=0.00, 0.125, 0.25, 0.375, 0.50, 0.75, 1.00). For a Sb alloying ratio of $x \geq 0.50$, a solid precipitate remained visible in the mixture despite increased reaction temperatures or additional solvent. This solid was removed by passing the solution through a 0.45 µm pore size filter. In the meantime, borosilicate substrates were cleaned as described above. The cleaned substrates were subsequently transferred into the glovebox and placed onto the 75 °C hotplate next to the CABB solution.

Fabrication of $Cs_2AgSb_xBi_{1-x}Br_6$ thin films – A cleaned borosilicate substrate was placed from the hotplate to the vacuum chuck of the spin coater (SPS–Europe, Polos–200), after which 80 µL of hot CABB solution was dropped onto the substrate with a pipette. Spin coating was immediately started at a speed of 4,000 RPM for 40 seconds, with an acceleration of 1,000 RPM/s. It was found that the dropwise addition of an antisolvent during spin coating is beneficial for obtaining a higher surface coverage (see Chapter 3.1). After 25 seconds of spin coating 100 µL of isopropanol was added dropwise onto the spinning substrate. This addition initiated immediate crystallization of CABB which was observed by a colour change from clear to dark yellow. The spin coated substrate was put aside for 15 minutes at room temperature (RT). As a last step the thin film was annealed by placing it on a 250 °C hotplate for 5 minutes. All thin film samples were stored in a glovebox for later use.

A similar procedure was followed for Sb-alloyed CABB thin films with a few minor modifications. The antisolvent addition during spin coating was done 5 seconds earlier, after 20 seconds of spin coating, respectively. The time difference is due to the fact that Sb-alloyed CABB crystallizes earlier than CABB. In addition, the annealing of the thin film was done at a lower temperature for Sb-alloyed CABB, namely at 130 °C instead of 250 °C. Literature shows that lowering the annealing temperature yields Sb-alloyed thin films with a higher surface coverage.[90]

Fabrication of NiO_x transport layer – A procedure was followed for the synthesis of NiO_x sol nanoparticles (NPs) that can act as HTL.[107,108] A sol can be described as a colloid in a suspension which is formed by the hydrolysis and condensation of a metal salt or alkoxide.[109] Here, 5 mmol (1.454 grams) of nickel nitrate hexahydrate ($Ni(NO_3)_2 \cdot 6H_2O$) was transferred to a 20 mL glass vial containing a stir bar, and 10 mL ethanol was added to obtain a final concentration of 0.5 M. According to literature, the addition of an amine can aid the stabilization of the sol and it can act as a sol modifier, which allows for good control of NiO_x sol formation.[110] The stabilizing agent used in this work is 2-methylimidazole, which was added to the vial in a 1:1 molar ratio of $Ni(NO_3)_2$ and 2-methylimidazole (this corresponds to 411 mg of stabilizer). Next, the temperature was raised to 70 °C and stirring was set to 500 RPM to allow for the dissolution of the nickel salt and stabilizer. During 2 hours of stirring, NiO_x sol NPs were formed in solution. To obtain a thin film of NiO_x, borosilicate substrates were first cleaned accordingly. Next, the cleaned substrates were placed onto the same hotplate as the NiO_x sol solution. The pre-heated substrate was placed on the vacuum chuck of the spin coater and 80 µL of hot NiO_x solution was dropped onto the substrate. This was spin coated for 40 seconds at 4,000 RPM with an acceleration of 1,000 RPM/s. After spin coating, the film was heated at 170 °C for 20 minutes, allowing the remaining solvent to evaporate. A step of annealing at 300 °C for 2 hours was required to obtain the final NiO_x thin film. To obtain a thicker film of NiO_x multiple layers can be spin coated. After each cycle of spin coating, the substrate was placed on a 170 °C hotplate for 10 minutes to allow the solvent to evaporate. After the final layer was added the thin film was annealed at 300 °C for 2 hours. Subsequently, the NiO_x thin film was stored in the dark for later use.

Fabrication of ZnO transport layer – A ZnO ETL can be formed by hydrolysis and condensation of a zinc-based salt, producing NPs which can be spin coated to form a thin film. The synthesis described below was adapted from Weller *et al.*[111]. Here, 6.72 mmol (1.475 grams) of zinc acetate dihydrate was added to a 250 mL round-bottom flask containing a stir bar. The round-bottom flask was placed in a heating mantle on a hotplate. 65 mL of methanol was added next, and the hotplate was set to 65 °C. To dissolve the zinc acetate the solution was stirred at 600 RPM. In the meantime, 850 mg KOH was dissolved in 38 mL methanol, obtaining a 0.35 M KOH solution. This solution was added dropwise to the zinc acetate solution under vigorous stirring. During the addition of the alkaline solution, the zinc acetate solution turned an opaque white. The opaqueness arises from the formation of ZnO NPs. After all the KOH solution was added, the ZnO suspension was stirred for an additional 2.5 hours at 65 °C to allow complete ZnO formation. The synthesis was followed by a washing step where the ZnO suspension was evenly transferred to two 50 mL centrifuge tubes. The ZnO NPs were collected by centrifugation (Hettich Rotina 380) at 4,300 RPM for 5 minutes. The resultant precipitate was redispersed in 15 mL methanol. Further purification was performed for another 3 cycles of centrifugation at 4,000 RPM for 5 minutes, and redispersion in 20 mL methanol. After the final cycle of centrifugation, the ZnO NPs were redispersed in 4 mL methanol and 4 mL chlorobenzene. The chlorobenzene aids in stabilizing the ZnO NPs in solution since these are insoluble in pure methanol. The resulting suspension was allowed to rest overnight, after which the supernatant was partially removed until approximately 2 mL was left. The ZnO NPs were redispersed in the leftover 2 mL solution with the aid of sonication. To obtain a thin film of ZnO, a clean borosilicate substrate was placed on the vacuum chuck of the spin coater and 80 µL ZnO NPs solution was dropped onto the substrate with a pipette. The ZnO NPs solution was then spin coated at 2,000 RPM for 40 seconds. The thin film was air dried and stored in the dark for later use.

Fabrication of TiO_2 transport layer – Another ETL material was explored, namely TiO_2.[87] Here, 426 µL titanium butoxide was added to a 20 mL glass vial and 2.53 mL isopropanol was added next. This solution was stirred at 500 RPM until fully mixed. Meanwhile, 35 µL of 2 M HCl was added to 2.53 mL of isopropanol. This acidic solution was then added dropwise to the Ti-solution under vigorous stirring at 750 RPM. During the addition, a sol-gel solution of TiO_2 was formed via the hydrolysis of the titanium alkoxide. Before the sol started to form into a gel, 25 µL of the sol solution was added dropwise on the substrate, and the substrate was spin coated for 45 seconds at 2,000 RPM. The thin film was placed in a pre-heated oven at 500 °C for 30 minutes to form the desired TiO_2 thin film. After the annealing step, the TiO_2 film was stored in the dark.

Photochemical CO_2 reduction – Here, a CABB thin film was mounted in a reaction cell with quartz window. The cell was placed in front of a light source (*i.e.*, simulated sunlight or 455 nm light) to excite the photoactive material, in a house-build gas flow setup located in a black box. Gas lines were connected to the gas inlet and gas outlet of the reaction cell. The lines and cell were flushed with N_2 gas at 2 mL/min for 30 minutes. After removal of gaseous contaminants, the cell was flushed with the reactants, namely with CO_2 and H_2 at a flow of 1 mL/min and 2 mL/min, respectively. The gas passing through the gas outlet was sampled every 4 minutes, and automatically injected in a GC equipped with a methanizer. The methanizer consists of a flame ionization detector (FID) and a reactor which converts CO and CO_2 into CH_4. This process allows for the detection of very low concentrations of CO. After stabilization of the flow, the light source was turned on.

X-ray diffraction crystallography – X-ray patterns were recorded with a Bruker AXs D8 Phaser in Bragg-Brentano geometry, using a Cu X-ray source ($K\alpha_{1,2}$ = 1.54184 Å) operated at 40 kV. All diffractograms were obtained by measuring from 5–60° 2θ with an integration time of 0.25 s and an increment of 0.025°. The thin film samples were loaded into an air-tight dome inside a glovebox.

UV-Vis spectroscopy – The absorptance, reflectance, and transmittance were determined using a Perkin-Elmer lambda UV-Vis-NIR lambda_950S with integrating sphere. The R was determined by placing a DP thin film at the back of the integrating sphere under an angle of 8°. The sum of R and T was determined by placing the thin film inside the sphere under an angle of 8°. The A was calculated using eq. 9 and T was determined with eq. 10. All measurements were carried out from 900 nm to 350 nm with a step size of 2 nm and integration time of 0.24 s.

Atomic force microscopy – The film thickness can be of key importance for the materials activity towards photochemistry.[5] Light absorption is increased when the film thickness is increased, but this is at the expense of trapped charges that are unable of participating in a chemical reaction due to its confinement in deeper crystal grains.[86,112,113]

Here, substrates were cut in smaller pieces with a diamond cutting tool, after the DP layer was lightly scratched using a syringe needle. These scratches allowed to determine the height difference between the substrate surface and thin film surface. Additionally, AFM was used to determine the smoothness of the surface, as it can probe individual nanometer-scale grains.

Scanning electron microscopy – A PhenomProX was used, operating at 15 kV. For analysis, borosilicate substrates with thin films were attached to the sample holder using carbon tape. The surface coverage and crystal grain size of thin films was determined, and equipped with an energy dispersive X-ray detection system, the stoichiometric composition of the DP thin films was analyzed

Chapter 4. Mechanochemical synthesis of DP composites

This section describes the process of synthesizing various CABB-based DP composites. First, we discuss the synthesis of CABB and CASB crystals via a well-reported procedure involving hot acidic conditions to dissolve bromide precursor salts.[44,114,115] Single crystals are of interest since these have different optoelectronic properties compared to bulk powders and thin films, such as defect density and carrier lifetimes.[17] Since we are also interested in a solvent-free approach to synthesize various composites derived from CABB, we explore the mechanochemical synthesis of various DP composites based on CABB. This strategy has already yielded promising results in the prior art of DP syntheses.[45,116]

4.1 Synthesis of CABB and CASB crystals

The solution-based synthesis of CABB and CASB in HBr is often used to obtain single crystals.[44] Here, the bromide precursor salts (CsBr, AgBr and $BiBr_3$ or $SbBr_3$ for CASB) are stoichiometrically dissolved in concentrated HBr acid at elevated temperatures. After the dissolution of the precursors, the hot acidic solution is allowed to cool down, decreasing the solubility of the DP and initializing the crystallization of the DP. A more elaborate description of the synthesis procedure is given in Chapter 4.4.2. One should note that the formation of CASB is more challenging than the well-documented synthesis approach of CABB crystals. Wei *et al.* describes a hydrothermal synthesis approach of CASB crystals in HBr at an elevated temperature of 160 °C for a prolonged time of 5 days, carried out in an autoclave.[90] In our synthesis approach of CASB we use milder reaction conditions, comparable to what was used for CABB, with a difference in amount of added HBr. For CASB, an additional amount of HBr is added to complete the dissolution of the CASB precursors. After dissolution, the majority of HBr is evaporated to allow CASB to crystallize. Similar to the Sb-alloyed CABB thin films, the color of the DP crystal redshifts with the incorporation of Sb^{3+}. Fig. 31a) and Fig. 31b) represent images of the synthesized CASB and CABB crystals, respectively.

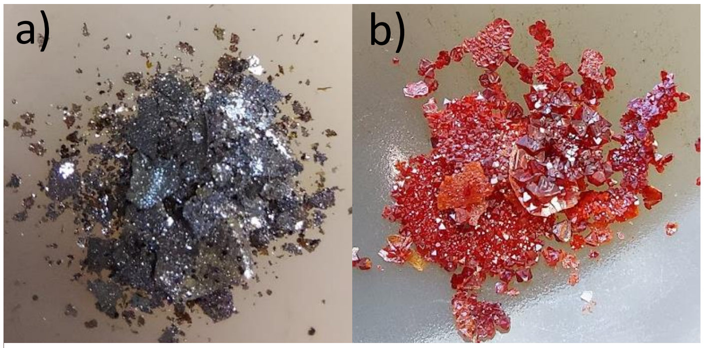

Figure 31. Images of crystalline **a)** CASB and **b)** CABB, synthesized via the solution-based HBr procedure.

The crystallinity of these CABB and CASB crystals is analyzed by means of XRD. The crystals are crushed prior to the measurement. As opposed to crystals, for the analysis of powders the preferential orientation of certain crystal facets is eliminated, yielding a homogeneous distribution of facets. XRD analysis of the obtained DP powders is performed under ambient conditions. We find that the XRD patterns closely resemble the reference of CABB (Fig. 32a). However, the peak intensities of CABB and CASB are different from the reference. The reference entails a simulated pattern of CABB which is calculated from single crystal X-ray experiments.[55] The intensity difference between sample and reference could be due to a preferential orientation of crystal facets that is used in the calculations, whereas the DP samples should have a homogeneous distribution of facets.

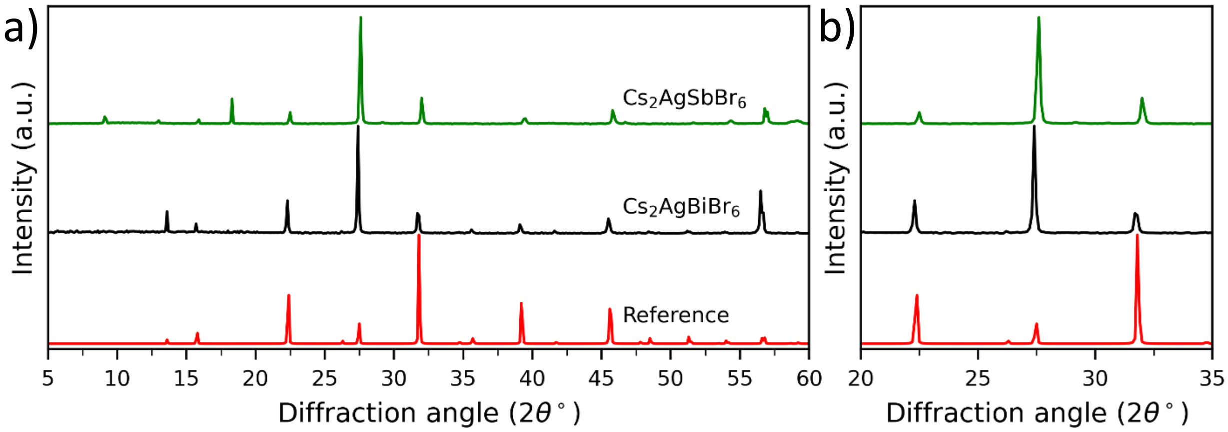

Figure 32. a) XRD patterns of CABB and CASB powdered crystals, compared to a reference and **b)** inset of the major peaks of these DPs to illustrate the peak shift of CASB to higher diffraction angles.

Even though the peaks that are attributed to CABB are also found in the diffractogram of CASB, there are some additional peaks appearing at angles of 9.1°, 13.0° and 18.3° 2θ, respectively. This is an indication of the presence of crystalline phases other than CASB. Possible side-products of the synthesis are $Cs_3Sb_2Br_9$, Cs_3SbBr_9, Cs_3SbBr_6, Cs_2SbBr_6, Cs_2AgBr_3 and $CsAgBr_2$.[90–92] Particularly $Cs_3Sb_2Br_9$ could be present as mixed phase, since its diffractogram shows peaks at approximately 8.9°, 12.6° and 17.9° 2θ (Fig. S5), closely matching with the reflections of the undesired component in the CASB XRD pattern.[117,118] Similar to the Sb-alloyed thin films, a diffraction shift to higher angles is also observed for CASB crystals as compared to CABB crystals, as shown in Fig. 32b). The origin of this shift is the contraction of the lattice constant.

Although the synthesis of CABB crystals via the HBr approach is a success, it proves to be more challenging for CASB. Even though that most XRD reflections of the elpasolite crystal structure can be observed in the diffractogram of CASB, the presence of additional peaks suggests the formation of a side product. This could also explain the insoluble yellow powder observed in the CASB precursor solution for the thin film method described in Chapter 3. We hypothesize that in this method an energetically more favorable product, such as $Cs_3Sb_2Br_9$, is formed. To circumvent the usage of a solvent we explore a mechanochemical approach to alloy CABB. Henk Bolink *et al.*[47] demonstrate that Bi^{3+} can be successfully substituted with other cations using ball milling. This technique will be discussed in more detail in the next section.

4.2 Mechanochemical synthesis of $Cs_2AgM_xBi_{x-1}Br_6$ (M = Sb, In, Fe, Al, Sn, Ti)

The mechanochemical synthesis via ball milling allows to produce various alloyed CABB derivatives without the use of solvents, making this a more environmentally friendly technique than solution-based counterparts.[45] For the synthesis of any of the alloyed DP composites, the precursor bromide salts are loaded into the ball mill jar together with steel milling balls in a nitrogen-filled glovebox. The jar is mounted in the ball mill and by the back-and-forth motion of the jar at 30 Hz the formation of the DPs is initiated. Fig. 33 shows a selection of the DPs that are synthesized in this work via ball milling. The synthesis leads to DP products with various colors, depending on the used alloy.

Figure 33. Images of a selection of the composite DPs that are synthesized with the ball mill. The differences in color demonstrate the effect of atomic exchange on the optical properties.

Electron microscopy is used to verify the stoichiometric ratio of elements for each of the synthesized DPs. Here, DP powder is loaded on a stub and mounted into the SEM. This microscopy technique allows us to see the crystalline powders on a micrometer scale. Fig. 34a-c) represent micrographs of some of the synthesized DP powders, namely $Cs_2AgBiBr_6$, $Cs_2AgFe_{0.50}Bi_{0.50}Br_6$ and $Cs_2AgSbBr_6$. Although SEM is considered as a reliable technique to analyze samples on the micrometer to nanometer scale (depending on the microscope), one should take into consideration that only a minute portion of the total sample is mapped. To limit this problem, multiple areas of the sample are analyzed, revealing that the crystal grains are uniform in size. However, it is noteworthy that with increased substitution of Bi^{3+} cations with another cation the crystal grain size increases. It is uncertain if the grain size difference is due to the alloying or if another effect is at play, such as the presence of unreacted precursors.

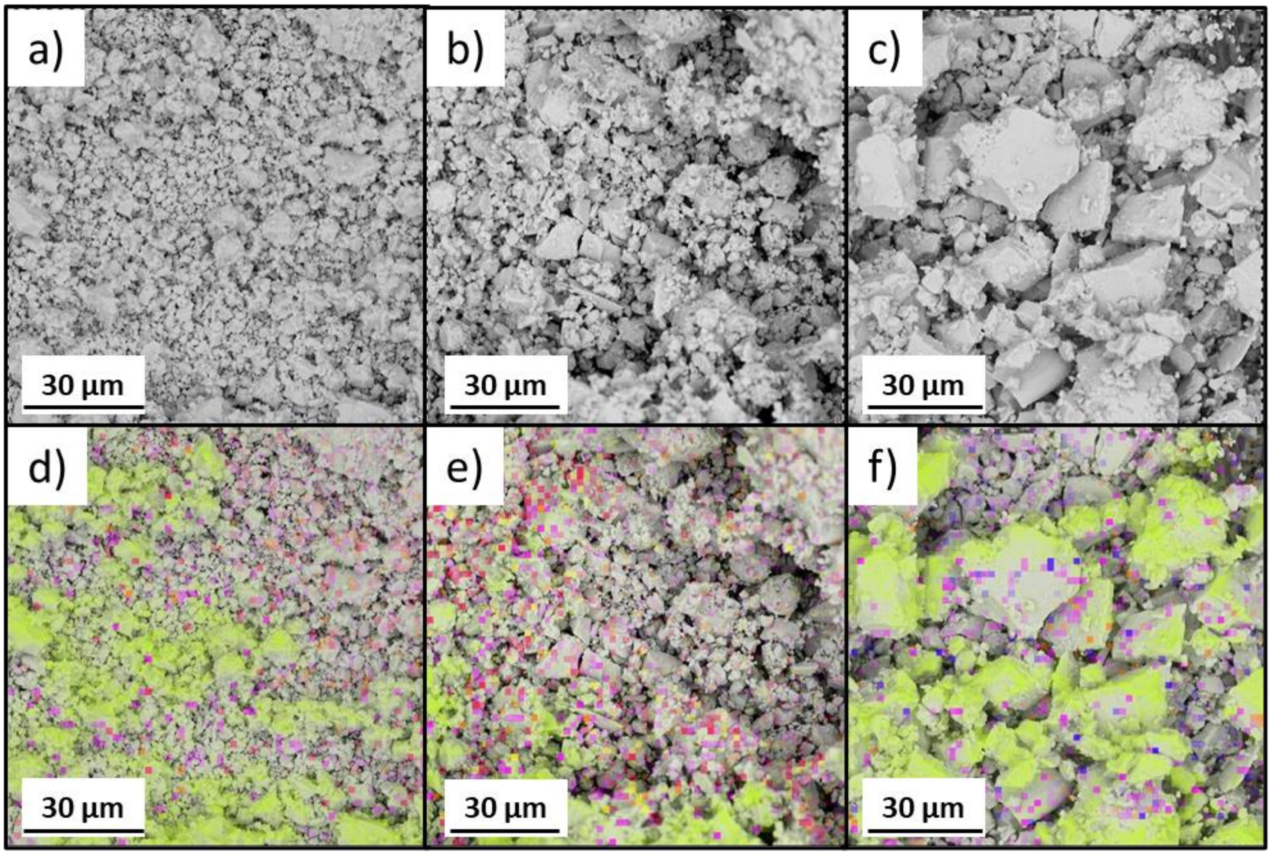

Figure 34. SEM micrograph of mechanochemically synthesized **a)** $Cs_2AgBiBr_6$, **b)** $Cs_2AgFe_{0.50}Bi_{0.50}Br_6$ and **c)** $Cs_2AgSbBr_6$. **d-f)** SEM-EDX analysis was performed on the respective DP composites. Green = bromide; pink = cesium; orange = silver; red = bismuth; yellow = iron; purple = antimony.

To confirm the stoichiometric ratio of elements in the DP powders we conduct SEM-EDX, which is a surface analysis technique to quantify the atomic ratio of elements on the surface of the analyzed sample. We show that the elements are distributed homogeneously across the powdered surface (Fig. 34d-f). The atomic ratios of the used elements are listed in Table 3. The stoichiometric concentrations of Br, Cs, Ag and Bi (or Bi with a substituted element) for the DPs should be 60%, 20%, 10% and 10%, respectively. In general, the stoichiometric ratios correspond well with the real atomic ratios listed in Table 3. It appears that for the most DPs the atomic ratio of Cs and Bi (or Bi with a substituted element) is higher than the stoichiometric ratio, while for Ag and Br the opposite is true. The certainty of the atomic concentration values is higher for elements that are substantially more present in the samples (*i.e.*, for Cs and Br). The certainty rapidly drops for Bi-exchanged DPs. To exemplify, a mere 0.79 out of 1.00 is the certainty for the concentration of Fe in the $Cs_2AgFe_{0.10}Bi_{0.90}Br_6$ DP, hence why the atomic concentration of Fe in $Cs_2AgFe_{0.01}Bi_{0.99}Br_6$ could not be reliably determined since the Fe concentration falls below the detection limit. Furthermore, the fact that EDX is a surface analysis technique and barely penetrates the sample argues that we are not able to fully rely on these values for real atomic ratios.

Table 3. Summary of the atomic compositions of Cs, Ag, X (X= Sb, In, Fe, Ti, Sn), Bi and Br, determined with SEM-EDX analysis.

DP composite	**Conc. of Cs**	**Conc. of Ag**	**Conc. of X* / Bi**	**Conc. of Br**
$Cs_2AgBiBr_6$	21.1%	8.5%	13.4%	57.0%
$Cs_2AgSbBr_6$	21.5%	9.8%	8.9%	59.7%
$Cs_2AgInBr_6$	21.8%	8.7%	7.8%	61.7%
$Cs_2AgIn_{0.5}Bi_{0.5}Br_6$	21.3%	8.6%	4.4% / 6.7%	59.1%
$Cs_2AgFe_{0.5}Bi_{0.5}Br_6$	22.0%	8.7%	4.6% / 6.3%	58.5%
$Cs_2AgFe_{0.1}Bi_{0.9}Br_6$	22.1%	8.2%	0.7% / 11.8%	57.1%
$Cs_2AgTi_{0.15}Bi_{0.85}Br_6$	19.4%	7.5%	1.1% / 12.8%	59.1%
$Cs_2AgSn_{0.15}Bi_{0.85}Br_6$	21.6%	8.2%	1.5% / 12.3%	56.4%

*X = Sb, In, Fe, Ti, Sn

4.3 Crystallographic and optoelectronic analysis of DP composites

In contrary to solution-based syntheses, the solid-state mechanochemical synthesis of DPs circumvents the formation of unwanted side products that are typically formed in solution.[119] To check the crystallinity of the ball mill products, XRD crystallography is used. The incorporation of different cations in the CABB structure mostly yields single-phased DPs (Fig. 35a). To exemplify, we have studied multiple substitution concentrations of Bi^{3+} by Fe^{3+}, namely 1%, 10%, 50% and 100%. Here we find that the complete substitution of Bi^{3+} with Fe^{3+} does not result in a single-phased DPs, whereas exchanging 50% or less of the Bi^{3+} with Fe^{3+} is successful in forming a an elpasolite structure. We also observe some reflections that do not correspond to the elpasolite crystal structure reference. For instance, related to what is observed for CABB thin films in Chapter 3.1, there is a broad reflection feature ranging from 7° to 15° 2θ. It is likely that the mechanical force during the ball milling process leads to a decrease in particle size, such that the crystalline domains become amorphous. This is presented by a characteristic broad feature, indicative for amorphous materials.[96]

In addition to this broad feature, in nearly all XRD patterns there is a shoulder or overlapping secondary peak on the left side of the reflection around 31° 2θ. This angle corresponds to one of the main peaks of AgBr, indicating that not all Ag^+ cations are incorporated into the elpasolite crystal structure and are left as its primary bromide salt.[120,121] AgBr also has a feature around 44.5° 2θ, which is particularly evident in the XRD pattern of $Cs_2AgTi_{0.15}Bi_{0.85}Br_6$.

The XRD data of some DPs reveal additional reflections in the diffractograms, indicating the presence of unwanted secondary phases or unreacted precursor salts. Highlighted are $Cs_2AgAl_{0.50}Bi_{0.50}Br_6$ and $Cs_2AgInBr_6$. XRD patterns of these DPs reveal reflections that do not appear in the elpasolite crystal reference. In the case of $Cs_2AgAl_{0.50}Bi_{0.50}Br_6$, peaks are located around 13°, 23.5°, 26° 2θ and an overlapping peak at 27.5° 2θ, which are not in accordance with the reference. Interestingly, $AlBr_3$ has matching reflections corresponding well with the observed secondary phase. Fig. S6 includes a calculated XRD diffractogram of $AlBr_3$ with peaks at 23.5°, 25.9°, and 27.8° 2θ, matching with the peaks in the diffractogram of $Cs_2AgAl_{0.50}Bi_{0.50}Br_6$.[122]

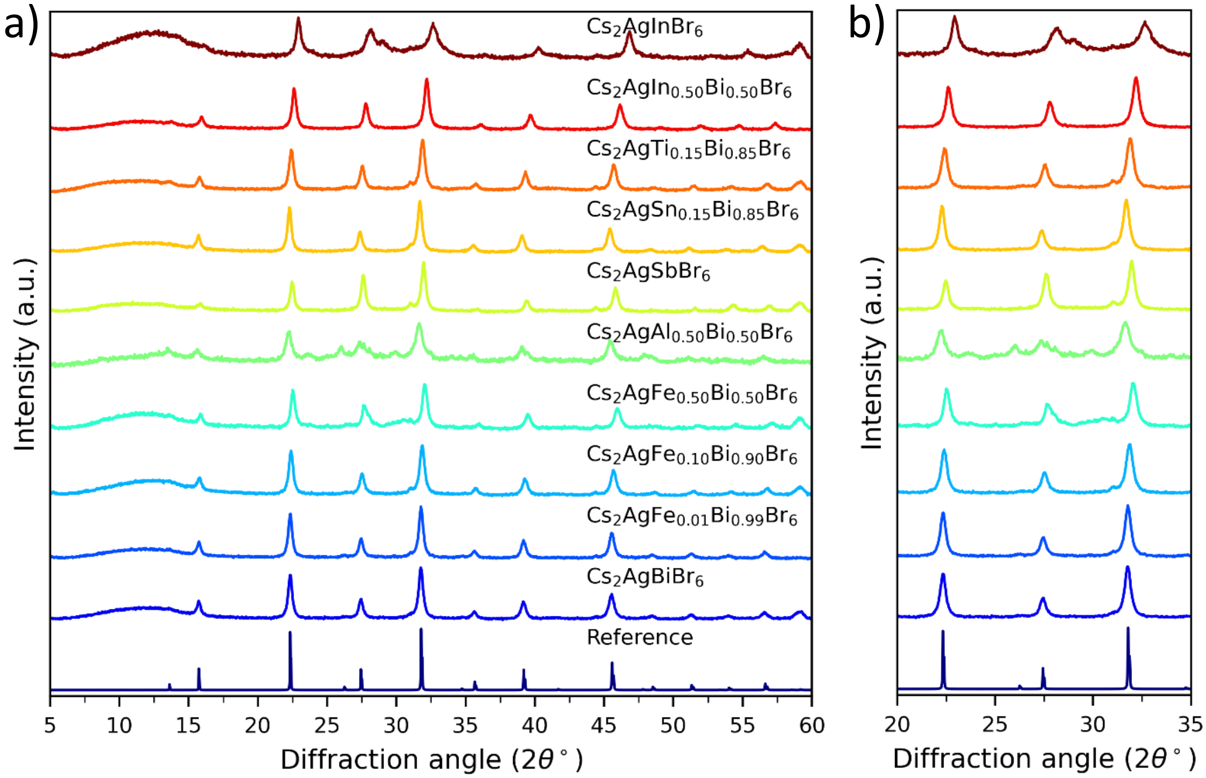

Figure 35. a) XRD patterns of the mechanochemically synthesized DP composites, compared to a reference. The diffraction peaks are in general relatively broad, which is most likely due to the small grain size of the DP crystals. **b)** Inset of the main XRD features to demonstrate the diffraction angle shift of the DP composites. The shift is caused by a change in lattice spacing, induced by exchanging cations in the crystal structure.

In the case of $Cs_2AgInBr_6$, we observe the rise of a reflection at 29° 2θ which is most likely from $CsAgBr_2$, since its main reflections are at 27.5° (overlapping with elpasolite reflection), 29.1° and 29.5° 2θ (Fig. S7).[123] In an attempt to reduce the presence of side phases in the $Cs_2AgInBr_6$ sample, we extended the duration of ball milling to 180 minutes. The XRD of 90 minutes and 180 minutes ball milling is presented in Fig. S8 and reveals the reduction of the 29° 2θ peak, indicating that extended ball milling could remedy the concern of having undesired phases in the DP sample.

In addition, as was also observed for alloyed DP thin films and crystals, we see a shift of the diffraction angles as the alloy is varied (Fig. 35b). As mentioned in the theoretical section (and in Chapter 3.2), X-ray reflections are dependent on the lattice spacing of a crystal, and the lattice constant a is calculated from eq. 13. The lattice constant for each of the synthesized DP composites is calculated using the reflection angles around 22.5°, 27.5°, 32° and 45.5° 2θ, corresponding to lattice planes with Miller indices (220), (222), (400) and (440), respectively.[41] The mean of the lattice constant for every DP composite is determined, and is plotted versus the respective DP alloy (Fig. 36).

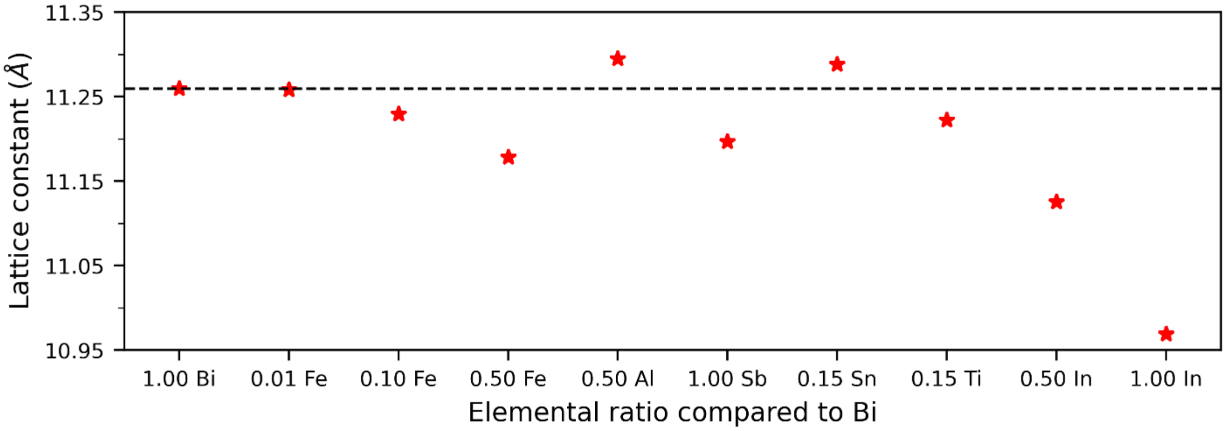

Figure 36. Plot of the calculated mean lattice constants of (alloyed) DP composites.

Interestingly, because the value of the lattice constant depends on the ionic radii, we can estimate whether the lattice constant will increase or decrease based on the type of alloy. Thanks to their high ionic radii, nearly all the used cations for alloying are smaller than Bi^{3+}, except for Sn^{2+}. In fact, the lattice constant expands with the alloying of Sn^{2+} while the smaller cations induce the shrinking of the lattice constant. Remarkably, the opposite is observed for the smaller Al^{3+} cation, and the lattice constant expands even though the Al^{3+} cation is nearly half the size of Bi^{3+}.[124] Unfortunately, it is not well-understood what effect could give rise to this expansion of the unit cell when CABB is alloyed with Al^{3+}.

A convenient way of determining if all the precursors react during the ball milling process is by relating the change in lattice constant to the alloying concentration. Since the lattice constant has a linear dependence on the alloying concentration, we can determine if the incorporation of the cationic substituent is successful.[98] Interestingly, increasing the Fe^{3+} concentration in DP alloys does not lead to a linear decrease of the lattice constant, suggesting that not all the $FeBr_3$ is reacting during ball milling (Fig. S9). To test the hypothesis of an incomplete incorporation of Fe^{3+} into the CABB crystal structure, the presence of unreacted $FeBr_3$ is studied in more detail. Given that $FeBr_3$ dissolves in ethanol, known amounts of the Fe-alloyed DP composites (*i.e.*, 10% Fe and 50% Fe) are added to 20 mL ethanol. The suspension is shaken to allow for any remaining $FeBr_3$ to dissolve. Upon introduction of any Fe-containing DP, the color of the solution changes to orange, indicating the dissolution of a component in the DP. The addition of $FeBr_3$ to ethanol results in a similar color. Both solutions are analyzed by means of UV-Vis and show similar absorption profiles (Fig. 37a), suggesting that either unreacted $FeBr_3$ is present as a mixed phase or that $FeBr_3$ is leaching from the crystal structure of Fe-alloyed DP composites. The latter hypothesis will be discussed in the upcoming paragraph. The amount of the unreacted $FeBr_3$ in the Fe-containing DP samples can be determined with the use of a dilution series with known $FeBr_3$ concentrations. The calibration curve is determined by matching the absorption maxima of the solutions with corresponding $FeBr_3$ concentrations (Fig. 37b). We find that for $Cs_2AgFe_{0.50}Bi_{0.50}Br_6$ approximately 82.6% of the Fe-species dissolves in the ethanol, while for $Cs_2AgFe_{0.10}Bi_{0.90}Br_6$ about 18.6% dissolves. Interestingly, when isolating the DP powder no color change is observed as compared to native color of the powder. This suggests that the Fe^{3+} ions (partially) remain in the DP crystal structure and that $FeBr_3$ in solution could be originating from unreacted reagents.

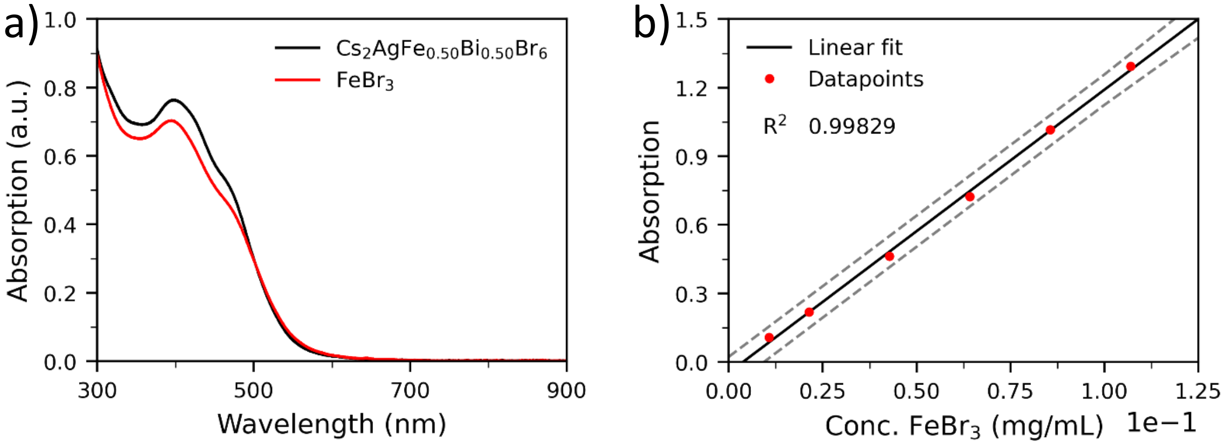

Figure 37. a) Normalized UV-Vis absorption spectra of an ethanoic solution of $FeBr_3$ (red) and $Cs_2AgFe_{0.50}Bi_{0.50}Br_6$ (black). **b)** Linear calibration curve of the absorption of known concentrations of $FeBr_3$ in ethanol.

To test the second suggested hypothesis of $FeBr_3$ leaching from the crystal structure, XRD analysis is performed to check if the crystal structure of the Fe-alloyed DP is maintained after the washing procedure with ethanol. First, samples of $Cs_2AgBiBr_6$ and $Cs_2AgFe_{0.10}Bi_{0.90}Br_6$ are analyzed by means of XRD, after which these powders are added to ethanol and stirred for 180 minutes. The resulting suspensions are centrifuged, and the DP powders are dried under vacuum. XRD of the dried powders are compared to the XRD of the respective powders before exposure to ethanol (Fig. 38a). If $FeBr_3$ is leaching from the crystal structure, the diffraction angles of the Fe-containing DP should shift to angular positions that correspond to CABB given that the incorporation of Fe^{3+} into the crystal lattice of CABB changes the lattice parameters. Highlighted by one of the main peaks of an elpasolite structure (Fig. 38b), the main peaks of $Cs_2AgFe_{0.10}Bi_{0.90}Br_6$ after washing with ethanol remain at their original position. This strongly suggests that $FeBr_3$ does not leach out of the crystal structure but is in fact more likely to be present as an unreacted precursor phase.

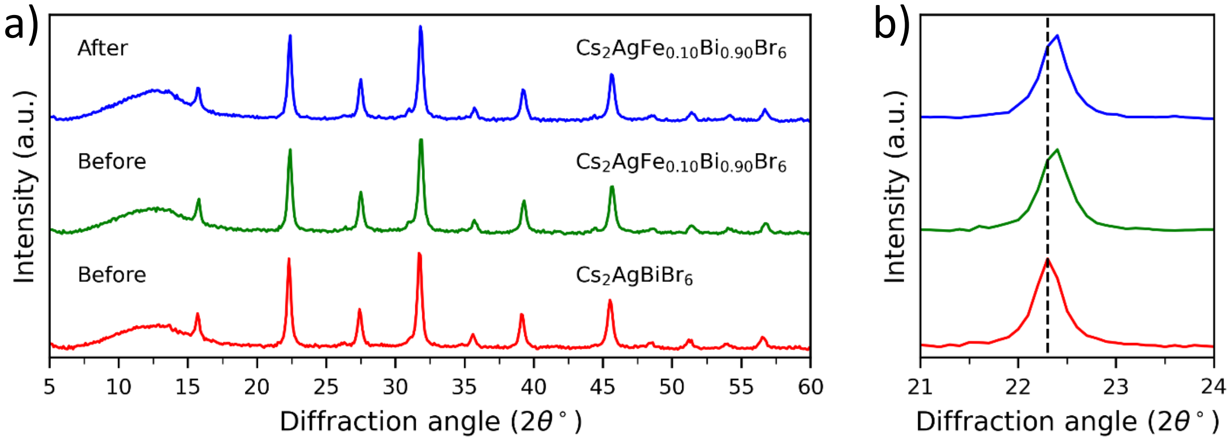

Figure 38. a) XRD patterns of $Cs_2AgBiBr_6$ (red) and $Cs_2AgFe_{0.10}Bi_{0.90}Br_6$ before (green), and $Cs_2AgFe_{0.10}Bi_{0.90}Br_6$ (blue) after washing with ethanol. The XRD peaks do not shift after the washing step, indicating no structural change as occurred. **b)** Inset of one of the main XRD peaks, showing the peak has not shifted to lower angles after ethanol washing, hence no $FeBr_3$ was leached from the crystal structure.

To validate the hypothesis of having $FeBr_3$ as unreacted phase mixed in with the Fe-alloyed DPs, one could perform XRD analysis of the DPs before and after washing with ethanol, in a range where an isolated reflection peak of $FeBr_3$ is present and detect if the peak corresponding to $FeBr_3$ diminishes. Unfortunately, all the peaks of $FeBr_3$ overlap with peaks of the elpasolite crystal structure, making this strategy challenging.

After establishing the phase-purity of our DP composites, we investigate the optical properties. The spectra of the DPs are recorded with UV-Vis spectroscopy, as shown in Fig. 39a-b). As was discussed in the theoretical section, in case of an infinitely thick material (*i.e.*, no transmission of light), the absorptance can be approximated by only considering the diffuse reflectance, according to the Kubelka-Munk theory. Fig. S10 shows diffuse reflectance spectra of the corresponding DP composites, and by transforming this data with the Kubelka-Munk function we obtain a relation to the absorptance of our materials, described as F(R), represented in Fig. 39. Here, the effect on the optical properties by the substitution of Bi^{3+} cations with a different cation is clearly demonstrated. The F(R) redshifts when Bi^{3+} is (partially) exchanged with cations of Sb^{3+}, Fe^{3+}, Sn^{2+}, and Ti^{4+}. The substitution of Sb^{3+}, giving rise to changes in the position of VB and CB band edge, is explained in detail in Chapter 2.2. For the other alloying cations, a comparable effect of shifting the CB minimum and VB maximum is expected to take place. In a theoretical study by Sebastiá-Luna *et al.* it is reported that alloying of Sn^{2+} into the CABB crystal structure has a similar contribution to the CB and VB alignment, redshifting the optical absorption.[50] Particularly for Fe-alloyed composites, as indicated in Fig. 39b), the redshift is significant where especially the highest loading of Fe^{3+} shows absorption features into the near infrared. On the other hand, by introducing In^{3+} a blueshift is observed (Fig. 39a). This is in line with the literature where it is demonstrated that the incorporation of In^{3+} increases the bandgap energy.[119]

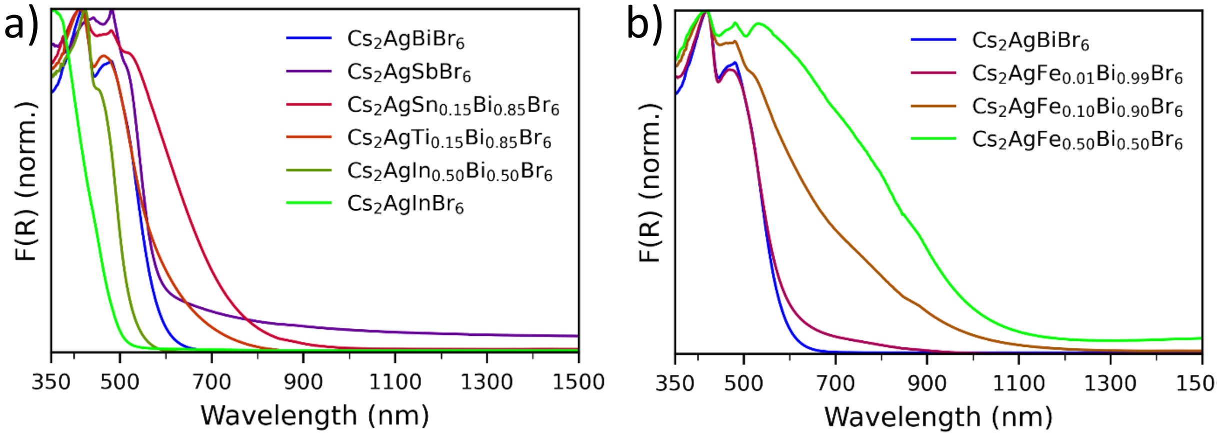

Figure 39. An overview of UV-Vis absorptance spectra of $Cs_2AgM_xBi_{1-x}Br_6$ DP powders. **a)** Absorptance of various synthesized DP composites, as indicated in the legend. **b)** Absorptance of Fe-substituted composites, showing the shift to infrared as more of the Bi^{3+} is substituted by Fe^{3+}.

4.4 Conclusions

We demonstrate the use of a solution-based approach to synthesize CABB and CASB crystals in HBr. XRD analysis reveals the excellent crystallinity of these samples, with only a few minor peaks in the diffraction pattern of CASB that do not correspond to the pure phase, suggesting the presence of a secondary phase, most likely $Cs_3Sb_2Br_9$.

To allow for a rapid and facile synthesis of a variety of different DP composites, we employ a mechanochemical synthesis route in the form of ball milling. Crystallographic analysis reveals that Bi^{3+} is successfully (partially) replaced with Sb^{3+}, In^{3+}, Fe^{3+}, Al^{3+}, Sn^{2+} and Ti^{4+}, forming near-pure crystalline phases. Furthermore, the change in lattice constant of each of the alloyed DPs is related to the ionic radius of the cationic substituent. This illustrates that both are in good agreement, apart from the Al-alloyed DP, where the lattice constant increased while the Al^{3+} cation is significantly smaller than Bi^{3+}. UV-Vis analysis shows us the influence of elemental alloying on the optical properties of the DPs. With the Kubelka-Munk transformation a relation to the absorption is obtained, and the F(R) shifts towards higher wavelengths when the DPs are alloyed with Sb^{3+}, Fe^{3+}, Sn^{2+}, and Ti^{4+}, revealing their promising optical characteristics for photochemical applications, which will be discussed in Chapter 5.

4.5 Experimental details

4.5.1 General information

All chemicals were used as received without any further purification. CsBr (99.999%), AgBr (99.998%), $BiBr_3$ (99%), $SbBr_3$ (99.999%), $InBr_3$ (%), $FeBr_3$ (98%), $AlBr_3$ (98%), $SnBr_2$ (99.98%) and HBr (48%) were purchased from Alfa Aesar. $TiBr_4$ (98%) and isopropanol (technical grade) were purchased from Acros Organics. Ethanol (>99.9%) was purchased from VWR Chemicals. Unless mentioned otherwise, DP precursors for the mechanochemical synthesis were handled in a nitrogen-filled glovebox with H_2O and O_2 levels around 0.6 and <0.1 ppm, respectively.

4.5.2 Methods

Synthesis of CABB crystals – 2 mmol (426 mg) CsBr, 1 mmol (188 mg) AgBr, and 1 mmol (449 mg) $BiBr_3$ were added to a 20 mL glass vial. 10 mL of a 9 M HBr solution was added to the solid mixture, after which the vial was placed on a hotplate capable of magnetic stirring. The temperature was raised to 110 °C and stirring was set to 650 RPM. Immediately after the acid addition, the mixture turned an orange colour. After 10 minutes of stirring at an elevated temperature the solids started to dissolve, and the mixture turned into a transparent yellow solution. After the complete dissolution of bromide precursor salts the solution was allowed to cool down to RT. Upon cooling, red crystals started to appear, indicating the successful formation of CABB crystals. The supernatant was removed, and the CABB crystals were washed twice with 10 mL ethanol. The crystals were then air dried and stored in the dark.

Synthesis of CASB crystals – 426 mg CsBr, 188 mg AgBr, and 361 mg $SbBr_3$ were added to a 20 mL glass vial. First, 10 mL of a 9 M HBr solution was added, and the solids were partially dissolved by heating the solution to 120 °C for 2 hours, with stirring at 650 RPM. Since not all solids dissolved, an additional 17 mL of 9 M HBr was added to the mixture. After 30 minutes of stirring at 650 RPM at a temperature of 120 °C, the solids dissolved. Crystallization of CASB was initiated by evaporating the HBr solvent at 150 °C. Evaporation was continued until approximately 2 mL of HBr was left over. The deep brown supernatant was removed with a glass pipette. The leftover black CASB crystals were washed twice with 10 mL of ethanol. The crystals were then air dried and stored in the dark.

Mechanochemical synthesis of DP composites – The general description below applies to all the DPs that were synthesized in this work (*i.e.*, Bi exchanged with: 1% Fe, 10% Fe, 50% Fe, 50% Al, 50% In, 100% In, 100% Sb, 15% Sn, and 15% Ti). For the synthesis of CABB, 4 mmol (852 mg) CsBr, 2 mmol (376 mg) AgBr, and 2 mmol (897 mg) $BiBr_3$ were manually mixed using a mortar and pestle. The pre-mixed powder was transferred to a 10 mL stainless steel milling jar and loaded with two 4-gram stainless steel milling balls. The milling jar was closed air-tight, in the glovebox, and mounted into a shaker ball mill (Retsch Mixer Mill MM 400). The mechanochemical synthesis was performed by shaking the jar at 30 Hz for 90 minutes. By mixing the reactants and closing and opening the reaction cell inside a glovebox this synthesis was be performed under inert atmosphere.

X-ray diffraction crystallography – X-ray diffractograms were recorded with a Bruker AXs D8 Phaser in Bragg-Brentano geometry, using a Cu X-ray source ($K\alpha_{1,2}$ = 1.54184 Å) operated at 40 kV. All diffractograms were obtained by measuring from 5–60° 2θ with an integration time of 0.25 s and an increment of 0.025°. For the measurement of crystals and bulk powders, the DPs were first ground with a mortar and pestle to obtain more homogenous grain sizes. The powders were then loaded into a sample holder and pressed together with a glass slide to obtain a compact homogeneously distributed layer.

UV-Vis spectroscopy – To determine the absorptive properties of the DP composite powder samples the Kubelka-Munk transformation was used (see theoretical section).

The diffuse reflectance of a powder was measured in a so-called DRIFT mode. Note that the Kubelka-Munk transformation scales with the absorptive properties of the studied powders. In order to measure the diffuse reflectance, DP powder was sandwiched between two glass slides forming a thick layer of powder where no light is able to pass through. The sandwiched powder was then mounted at the back of the integrating sphere under an angle of 8° with respect to the incident beam. A port in the integrating sphere was removed, so that the specularly reflected light leaks out of the integrating sphere, allowing to only record the diffuse reflectance.

Scanning electron microscopy – The grain structure properties of DPs were studied using SEM. In addition, equipped with an energy dispersive X-ray detection system, the stoichiometric composition of the DPs was analyzed. A PhenomProX was used, operating at 15 kV. For analysis, the DPs were dispersed on a piece of carbon tape. This way the DP powder could be analyzed for its stoichiometric composition and crystallinity.

Chapter 5. DP composites for photochemical dye degradation

We use photochemical dye degradation as a model system to test our DP composites for their photochemical activity. Many studies have reported on this branch of photochemistry, making it a well-documented approach.[24,68,125] In this chapter, we use two different dyes to track the photochemical activity of our DP composites, namely rhodamine B (RhB) and methylene blue (MB). The dye degradation experiments are conducted by illuminating ethanoic suspensions of the DP powders with different light sources under ambient conditions, in a similar manner as described in literature.[24] To gain a better insight into the factors affecting the photochemical activity, three different light sources are used, emitting simulated sunlight, blue light (centered around 455 nm, with a FWHM of 25 nm), and green light (centered around 518 nm, with a FWHM of 31 nm), respectively. In this section we will give an extensive overview of the different dye degradation experiments that are performed in this work.

5.1 Rhodamine B degradation

We follow previous work from Zhang *et al.* to conduct dye degradation experiments using RhB as a dye in the concentration of 100 mg/L.[24] First, $3.77\cdot10^{-2}$ mmol (approximately 40 mg, depending on the composite) of DP powder is suspended in 100 mg/L RhB solution and stirred for 60 minutes in the dark to allow for adsorption and desorption equilibrium of dye on the DP surface. A simulated sunlight source, having an intensity of approximately one sun, is used to illuminate the ethanoic suspensions of $Cs_2AgBiBr_6$, $Cs_2AgSbBr_6$, $Cs_2AgInBr_6$, $Cs_2AgFe_{0.50}Bi_{0.50}Br_6$, and $Cs_2AgSn_{0.15}Bi_{0.85}Br_6$, respectively. The PL of RhB is measured every 20 minutes throughout the experiment.

Fig. 40a-c) shows the PL intensity of RhB over time for a selection of the DPs. In all cases the PL does not reach zero, indicating that not all the dye is degraded at the end of the experiment (after 160 minutes). It should be noted that upon addition of the ethanoic RhB solution to $Cs_2AgSbBr_6$ and $Cs_2AgInBr_6$ the native color of the DPs disappears, and the powders turn pale yellow. This is a strong indication that these composites are not stable under these conditions. Therefore, these DP composites are not included in the figure.

Fig. 40d) shows the PL of RhB over time. The rate of PL decay for unalloyed CABB is comparable to the rate of decay where 50% of the Bi^{3+} is exchanged with Fe^{3+}, whereas the PL of RhB decays minimally for $Cs_2AgSn_{0.15}Bi_{0.85}Br_6$. One would expect that the alloyed CABB compositions in both cases would demonstrate an improved photochemical activity considering the increased visible light absorption that was observed in Chapter 4.3. However, the chemical stability of the DP composites should also be taken into consideration. CABB is well-known to be stable in ethanol, but by (partial) substitution of Bi^{3+} with another cation the chemical stability may decrease.[24] The addition of a solvent could lead to chemical changes of the DP, leading to the observed color change of $Cs_2AgSbBr_6$ and $Cs_2AgInBr_6$. In the case of $Cs_2AgSn_{0.15}Bi_{0.85}Br_6$, earlier work found that Sn-containing DPs are prone to oxidation, where the Sn^{2+} oxidizes to Sn^{4+}.[55,126] Due to the hydrophilic nature of ethanol, moisture from the ambient air could be taken up by the ethanoic dye solution and induce the oxidation of Sn^{2+} to Sn^{4+} in the DP, leading to a decline of the photochemical activity.[127]

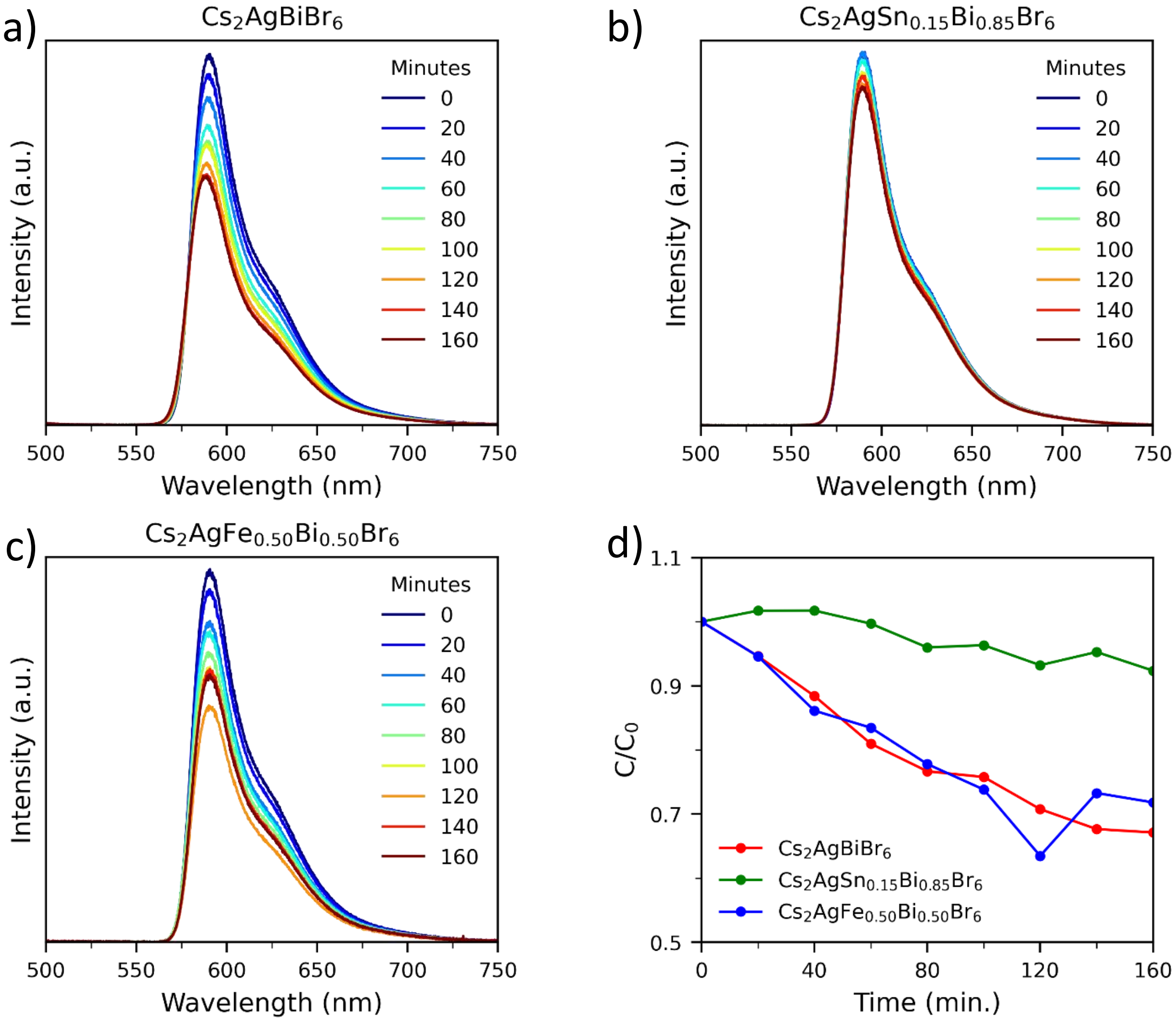

Figure 40. RhB PL decay measured over time under illumination of simulated sunlight, with **a)** $Cs_2AgBiBr_6$, **b)** $Cs_2AgSn_{0.15}Bi_{0.85}Br_6$ and **c)** $Cs_2AgFe_{0.50}Bi_{0.50}Br_6$ as a photocatalyst. **d)** Overview of the PL intensity decay for the three tested composite DPs for RhB degradation.

Considering the 50% Fe-alloyed DP, the PL intensity of RhB declines at a similar rate as CABB, while the sunlight absorption of the former is significantly enhanced. The improved light absorption scales with the number of photogenerated charge carriers, hypothesizing that this would lead to an enhanced reaction rate. However, as discussed in the theoretical section, whether a redox reaction will take place, and how the reaction pathway will propagate depends on the energy of the photogenerated charge carriers. Since the absorption of $Cs_2AgFe_{0.50}Bi_{0.50}Br_6$ is significantly redshifted compared to CABB, the bandgap energy might not match the required potential to degrade RhB. Another hypothesis is that defects in the crystal structure of $Cs_2AgFe_{0.50}Bi_{0.50}Br_6$ can inhibit the usage of these charges. Defects arise from imperfections in the crystal lattice and are more common for alloyed DP composites due to the introduction of non-native ions.[17,128] As discussed in Chapter 2.1, photoexcited charges can get trapped at these defect states in the crystal structure, preventing them from participating in redox reactions. This trapping mechanism proves to be one of the major causes of efficiency loss in photochemistry and photovoltaic applications.

Another suggestion regarding the lack of an enhanced photochemical activity of $Cs_2AgFe_{0.50}Bi_{0.50}Br_6$ is the consequence of the incomplete incorporation of Fe^{3+} in the CABB crystal lattice. This was discovered from relating the lattice constant to the alloying concentration, as discussed in Chapter 4.3. It is plausible that the unreacted $FeBr_3$ in the Fe-alloyed DP samples reduces the photochemical activity. In this hypothesis, $FeBr_3$ in the DP sample dissolves in the ethanoic dye solution and absorbs a portion of the incident light from the excitation source, thus decreasing the absorption of the Fe-alloyed DP sample. Consequently, less charges are excited that can partake in the dye degradation. If we consider that the absorption of $FeBr_3$ in ethanol (see Fig. 37a) partially overlaps with the emission of the simulated sunlight source, this as a valid reason for the lack of an improved RhB degradation rate under simulated sunlight.

For the following experiments, a light source is used that has an emission overlapping with the absorption maximum of the DP composites. For this, a light source emitting blue light, centered around 455 nm is chosen. At this wavelength all the synthesized DP composite powders absorb approximately the same amount of light. $Cs_2AgBiBr_6$, $Cs_2AgFe_{0.50}Bi_{0.50}Br_6$, $Cs_2AgIn_{0.50}Bi_{0.50}Br_6$, $Cs_2AgTi_{0.15}Bi_{0.85}Br_6$, $Cs_2AgFe_{0.10}Bi_{0.90}Br_6$ and $Cs_2AgFe_{0.01}Bi_{0.99}Br_6$ are used in this series of experiments.

Fig. 41 shows the PL decay of RhB with $Cs_2AgBiBr_6$ and $CsAgIn_{0.50}Bi_{0.50}Br_6$ under the influence of 455 nm light exposure, and the PL decay results of the remaining DP composites are given in Fig. S11. Compared to the simulated sunlight, the blue light source enables faster degradation of RhB. Interestingly, the PL maximum of RhB blueshifts during the experiments. In similar experiments reported in literature where the absorption decay of RhB is measured instead of PL, the effect of absorption blueshift is governed by the formation of rhodamine from the de-ethylation of RhB, driven by active oxygen species attacking the RhB (eq. 22, Chapter 2.5).[129] It is likely that the observed blueshift in PL can be ascribed to a similar process of RhB degradation, forming a rhodamine-based compound with a PL wavelength which is blueshifted from RhB.

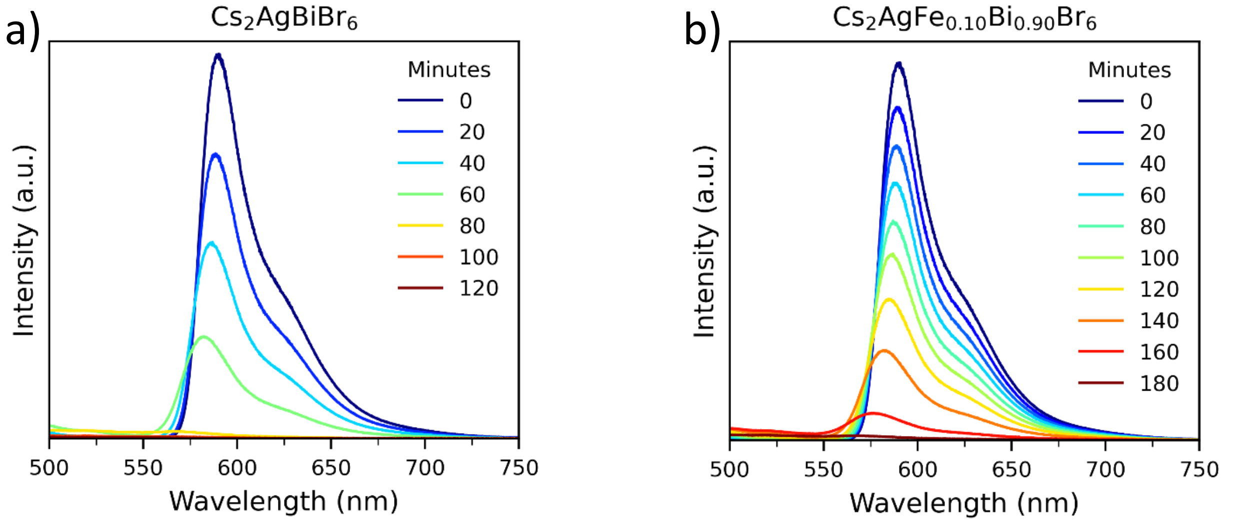

Figure 41. RhB PL decay measured over time under illumination of 455 nm light, with **a)** $Cs_2AgBiBr_6$, and **b)** $Cs_2AgIn_{0.50}Bi_{0.50}Br_6$. At the end of each measurement the majority of the RhB was degraded.

To get an idea of the reaction rate of these degradation experiments the decrease of the RhB PL intensity is plotted over time (Fig. 42a). In all cases the PL intensity follows a decreasing linear trend, suggesting zeroth-order reaction kinetics (eq. 23). The reaction rate of a zeroth-order reaction is determined by the slope of a linear fit of the data (Fig. 42b). To verify the validity of a zeroth-order reaction for RhB degradation, we identify the strength of the linear fits by considering the coefficient of determination (R^2). A perfect linear fit will have a value of 1, where any deviation in the datapoints will lower this value. The datapoints have a strong correlation with a linear fit. So, it follows that all DP samples degrade RhB under blue light illumination following zeroth-order reaction kinetics. Such reaction kinetics are also described in Chapter 2.5.[24]

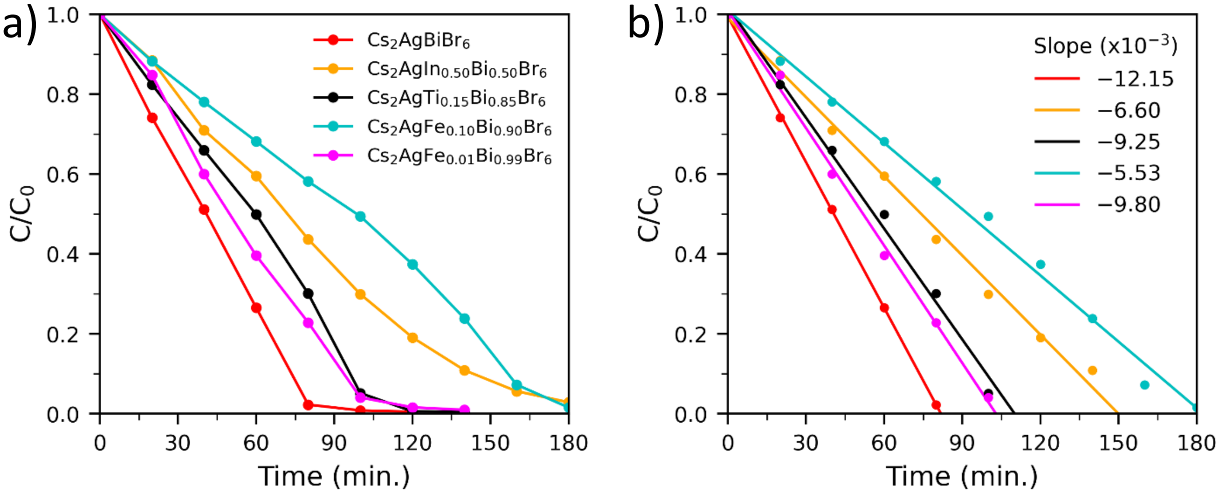

Figure 42. a) RhB PL maxima decay over time under illumination of 455 nm light, with the use of the DP composites as mentioned in the legend. **b)** Linear fits of the RhB PL decay for the different DP composites, with $R^2 > 0.99$. The legend shows the slope, equal to the reaction rate, of each degradation.

From the slope of the linear fits, we can conclude that CABB is the fastest at degrading RhB, while alloyed DP composites present slower degradation rates. As was discussed regarding RhB degradation with simulated sunlight exposure, the rates of alloyed DP composites could be affected by the introduction of defects in the crystal structure or by the lower energy of photogenerated charge carriers. These postulations can also be applied to the experiments with blue light.

A control test is performed to exclude the self-degradation mechanism of RhB when exposed to blue light (photolysis). Fig. S12 reveals only a slight decrease of the RhB PL intensity when illuminated with blue light, indicating that photolysis of RhB partakes an insignificant contribution to the observed PL decay of RhB during the dye degradation experiments.

To summarize, the RhB degradation experiments reveal no improved degradation rates when DPs with improved light absorption are used, for both simulated sunlight and blue light illumination. Additionally, $Cs_2AgSbBr_6$, $Cs_2AgInBr_6$, and $Cs_2AgSn_{0.15}Bi_{0.85}Br_6$ prove to be unstable when added to an ethanoic solution. Compared to simulated sunlight, the use of a blue light source improves the RhB degradation rate significantly. To gain more insight into the effect of bandgap engineering on the photochemical activity we test various DPs towards the photochemical degradation of MB, which is discussed in the next paragraph.

5.2 Methylene blue degradation

As mentioned above, the DP composites absorb approximately the same amount of light for the blue light source. To study the effect of the improved visible light absorption induced by alloying, the dye degradation experiments are repeated using another light source. By using a green light source (centered around 518 nm) the overlap of the CABB absorption profile and the emission spectrum of the lamp is significantly reduced (Fig. S3), while the emission spectrum of the green light source still overlaps with the absorption profile of the DP samples. This way, the effect of improved visible light absorption can be studied. To exclude photolysis of the dye, another dye molecule is required, as RhB absorbs 518 nm light as well. For this reason, MB is used.

We study different DP composites for the photochemical degradation of MB under 518 nm irradiation, namely $Cs_2AgBiBr_6$, $Cs_2AgFe_{0.50}Bi_{0.50}Br_6$, $Cs_2AgIn_{0.50}Bi_{0.50}Br_6$, $Cs_2AgSn_{0.15}Bi_{0.85}Br_6$, $Cs_2AgTi_{0.15}Bi_{0.85}Br_6$, $Cs_2AgFe_{0.10}Bi_{0.90}Br_6$ and $Cs_2AgFe_{0.01}Bi_{0.99}Br_6$. For these experiments the absorption of the dye is determined by means of UV-Vis spectroscopy. Fig. 43 represents the decreasing absorption profile of MB with $Cs_2AgBiBr_6$ and $Cs_2AgIn_{0.50}Bi_{0.50}Br_6$ (Fig. S13 shows the decrease of MB absorption profile for all other DP samples). Surprisingly, $Cs_2AgIn_{0.50}Bi_{0.50}Br_6$ is one of the best performing DPs in terms of reaction rate, even though its light absorption at the emission wavelength of green light is rather poor.

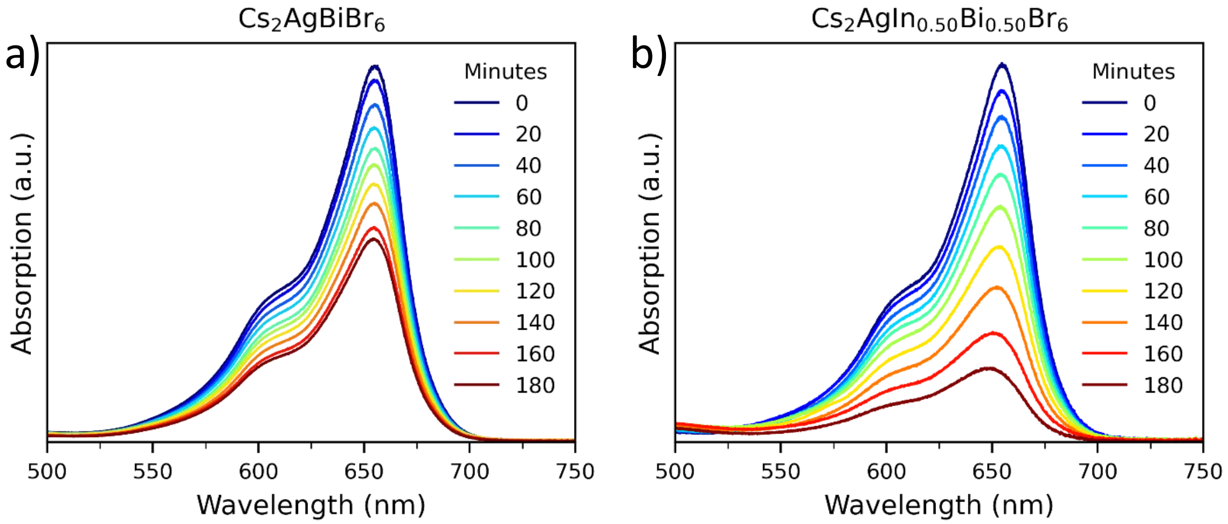

Figure 43. UV-Vis measurements recording the MB absorption decay over time under illumination of 518 nm light, with **a)** $Cs_2AgBiBr_6$, and **b)** $Cs_2AgIn_{0.50}Bi_{0.50}Br_6$.

Analogous to what is observed for RhB degradation, the studied DPs are expected to degrade MB with the kinetics of a zeroth-order reaction model. However, not all the tested DP composites show this linear dependance, as depicted in Fig. 44a-b). To distinct between linear and non-linear behavior we keep the R^2 above 0.95. We find that linearity applies to $Cs_2AgBiBr_6$, $Cs_2AgIn_{0.50}Bi_{0.50}Br_6$, $Cs_2AgTi_{0.15}Bi_{0.85}Br_6$, and $Cs_2AgFe_{0.01}Bi_{0.99}Br_6$. As discussed in Chapter 2.5, a linear decay is consistent with a zeroth-order kinetic. Moreover, according to the Lambert-Beer law there is a linear relation between absorption and concentration.[130] The measured absorption can therefore be directly related to the dye degradation reaction rate, which is equal to the slope of the decay.

Fig. 44b) reveals that $Cs_2AgFe_{0.50}Bi_{0.50}Br_6$ has no activity towards MB degradation, while it demonstrated a similar photochemical degradation rate as CABB under simulated sunlight for RhB degradation. To explain this difference, one should also consider the required energy to drive this reaction, as was discussed for RhB degradation in previous paragraph, where the bandgap energy of $Cs_2AgFe_{0.50}Bi_{0.50}Br_6$ might not match the required potential to degrade MB.

Another theory to account for the lack of MB degradation using $Cs_2AgFe_{0.50}Bi_{0.50}Br_6$ is the overlap of $FeBr_3$ absorption and green light emission. As was postulated for RhB degradation, the dissolved $FeBr_3$ from the Fe-alloyed DPs may absorb a portion of the incident excitation light during the dye degradation experiments, thus lowering the light absorption of the DP composite. Fig. S14 reveals that indeed the emission of 518 nm light partially overlaps with the absorption of $FeBr_3$.

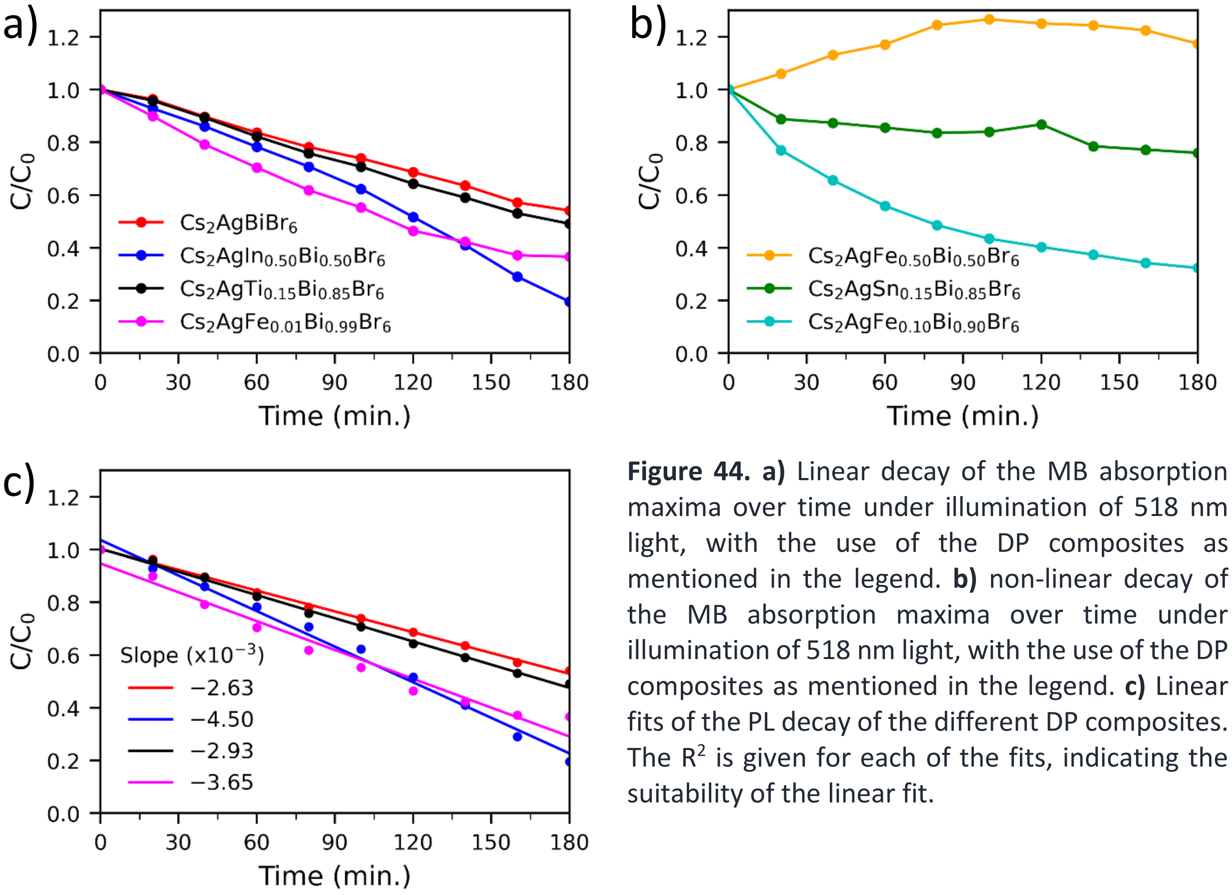

Figure 44. a) Linear decay of the MB absorption maxima over time under illumination of 518 nm light, with the use of the DP composites as mentioned in the legend. **b)** non-linear decay of the MB absorption maxima over time under illumination of 518 nm light, with the use of the DP composites as mentioned in the legend. **c)** Linear fits of the PL decay of the different DP composites. The R^2 is given for each of the fits, indicating the suitability of the linear fit.

To get a more detailed picture of the photochemical activity of our synthesized DP composites, a selection of alloyed DP composites is tested for MB degradation with 455 nm light. Interestingly, comparing MB degradation with $Cs_2AgBiBr_6$ under different illumination conditions (455 nm, 518 nm, and dark exposure) we find a fascinating trend: The MB dye degrades at a similar rate when exposed to 518 nm light as when there is no light source (Fig. 45a). It is postulated that this is an effect of MB adsorption onto the CABB surface, rather than photoinduced degradation. This adsorption effect was discussed in Chapter 2.5.

Here it is key to stress that the ethanoic MB solutions with DPs are allowed to reach adsorption and desorption equilibrium for 60 minutes in the dark prior to each measurement. To see if the adsorption and desorption is at equilibrium before the start of the dye degradation experiment, the absorption of MB is measured at an extended time frame while being exposed to CABB in the dark. The absorption is measured right after adding the ethanoic MB solution to CABB, after 1 hour of stirring and after 16 hours of stirring in the dark, respectively. As illustrated in Fig. 45b), the absorption of MB decreases significantly over a time frame of 16 hours compared to 1 hour of equilibration. Since the adsorption test was performed in the dark, we can exclude the effect of photochemical dye degradation. It is therefore likely that the observed decrease in absorption of MB under illumination of green light and dark exposure is due to adsorption onto the DP surface.

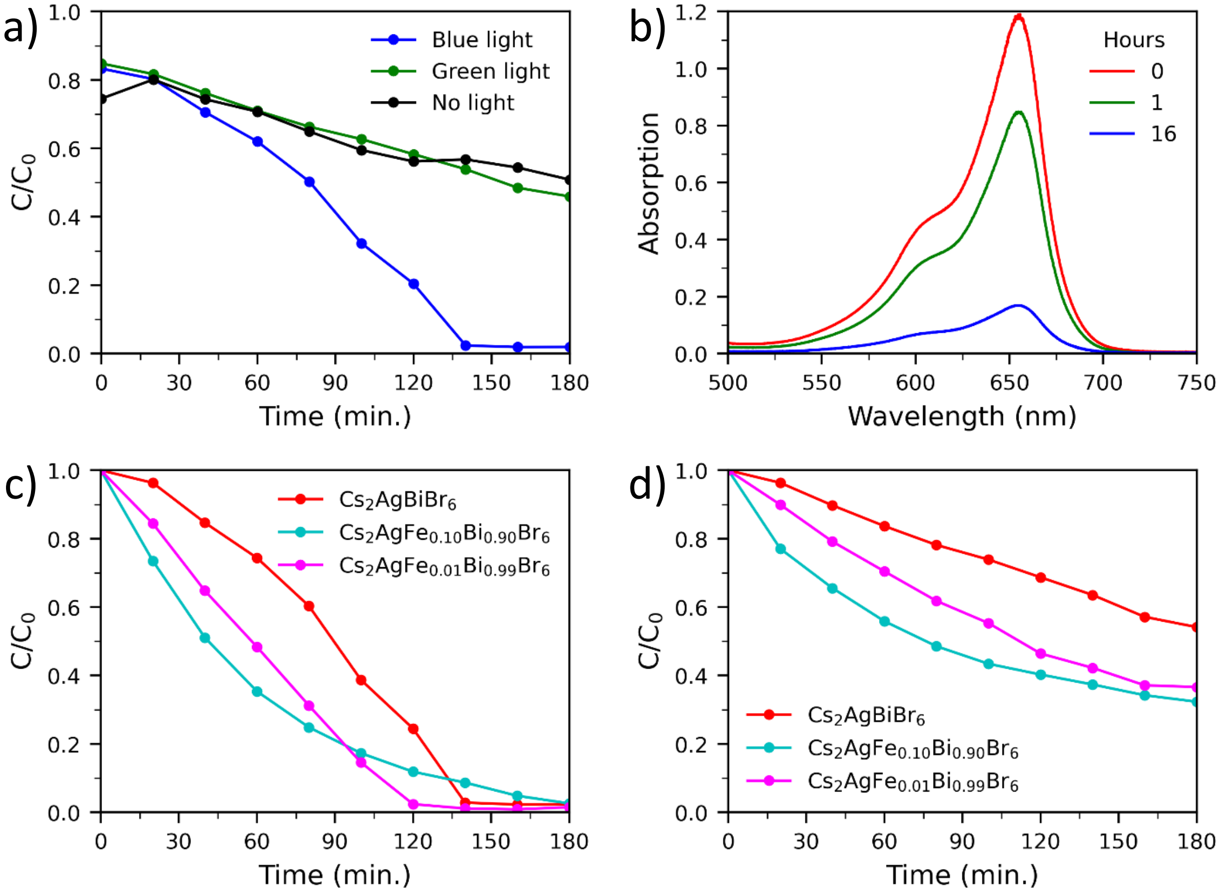

Figure 45. a) UV-Vis spectra of MB recorded at different times, to test the adsorption power of CABB under dark exposure. **b)** Comparison of MB dye degradation experiments performed under different illumination conditions (*i.e.*, 455 nm light (blue), 518 nm light (green) and without exposure to any light source (black)). **c)** MB absorption decay over time with the composites listed in the legend, under 455 nm light exposure. **d)** MB absorption decay over time with the composites listed in the legend, under 518 nm light exposure.

Since the adsorption and desorption equilibrium of MB on the CABB surface takes longer than 1 hour, we also test the adsorption capability of the various DP composites. Here, UV-Vis analysis of MB at the start of the degradation experiments reveals that, depending on the DP composite, the absorption of MB is different (Fig. S15). Since for every experiment the initial MB concentration is the same, it shows that the DPs have a varying tendency to adsorb MB onto the surface depending on the alloying composition. The above observations regarding the adsorption of MB (and dyes in general) ask for a more comprehensive study on this phenomenon and its effect on the dye degradation process.

Taking the adsorption effect into account, if the MB absorption decay under blue light exposure is considered, its rate can be regarded as a sum of photochemical MB degradation and MB adsorption onto the DP surface. Fig. 45c) shows the degradation of MB with $Cs_2AgFe_{0.01}Bi_{0.99}Br_6$ and $Cs_2AgFe_{0.10}Bi_{0.90}Br_6$, under 455 nm light exposure compared to CABB. MB degradation under 518 nm light exposure with Fe-alloyed DP composites is highlighted in Fig. 45d) to demonstrate the effect of light source. These figures illustrate that using a light source emitting light with a higher energy (blue light) is superior compared to using green light in aiding the degradation of MB, independent of the composite that is being used.

In general, we see that the 1% Fe and 10% Fe DPs are more active in degrading MB under illumination compared to CABB. As was observed earlier, the MB degradation with $Cs_2AgFe_{0.10}Bi_{0.90}Br_6$ follows a different degradation mechanism as the reaction kinetics are non-linear. It appears that the dye is degraded following an exponential trend, suggesting first-order reaction kinetics. As discussed in Chapter 2.5, first-order reaction kinetics are observed for weak adsorptive photoactive materials, suggesting that $Cs_2AgFe_{0.10}Bi_{0.90}Br_6$ is less efficient at adsorbing MB onto its surface. However, considering the absorption of MB in the first hour of an experiment (Fig. S15), $Cs_2AgFe_{0.10}Bi_{0.90}Br_6$ is one of the leading DPs at adsorbing MB, which is indicated by the low absorption intensity of MB. Hence, the first-order kinetics cannot be ascribed to the weak adsorption of MB onto the $Cs_2AgFe_{0.10}Bi_{0.90}Br_6$ DP surface, and a different mechanism must be at play.

We describe the exponential decay of MB with a mono natural exponential fit in the form of:

$$C_t = a \cdot e^{(-kt)} + b \tag{24}$$

Where, a is the amplitude and b gives the height of the fit. In Fig. S16 we show the exponential fit of MB degradation with $Cs_2AgFe_{0.10}Bi_{0.90}Br_6$ under 518 nm and 455 nm light illumination. The reaction rates of $Cs_2AgFe_{0.10}Bi_{0.90}Br_6$ are determined from this fit, and together with the reaction rates of $Cs_2AgBiBr_6$ and $Cs_2AgFe_{0.01}Bi_{0.99}Br_6$, are listed in Table 4.

Table 4. DP composites and their respective reaction rates towards MB degradation under different illumination conditions.

DP composite	Reaction rate (blue light)	Reaction rate (green light)
$Cs_2AgBiBr_6$	$7.09 \cdot 10^{-3}$	$2.63 \cdot 10^{-3}$
$Cs_2AgFe_{0.01}Bi_{0.99}Br_6$	$8.33 \cdot 10^{-3}$	$3.65 \cdot 10^{-3}$
$Cs_2AgFe_{0.10}Bi_{0.90}Br_6$	$2.92 \cdot 10^{-4}$ s^{-1}	$2.76 \cdot 10^{-4}$ s^{-1}

5.3 Conclusions

To summarize, the above experiments demonstrate that tuning the absorption of DPs is a promising way to enhance the photochemical activity towards dye degradation. Despite that some of the synthesized DP composites show poor stability in ethanoic conditions, useful information regarding the kinetics of dye degradation is obtained by performing tests with the stable DP composites. We find that the kinetics of RhB and MB degradation are considerably different and that adsorption effects play a crucial role in the dye degradation process. In case of RhB degradation, the photoactive DP composites have zeroth-order kinetics under simulated sunlight and blue light irradiation, where CABB is the most effective at degrading RhB. For MB degradation, however, Fe-alloyed CABB (1% and 10% Fe, respectively) shows the most promising reaction rates under blue and green light illumination. Interestingly, $Cs_2AgFe_{0.10}Bi_{0.90}Br_6$ reveals first-order kinetics towards MB degradation, whereas $Cs_2AgFe_{0.50}Bi_{0.50}Br_6$ has no activity at all.

In conclusion, we demonstrate that Fe-alloying increases the rate of degradation of MB, having an improved activity compared to CABB. These observations pave ways to explore the alloying of CABB to a greater extend, and test these DP composites for other photochemical reactions, such as CO_2 reduction.

5.4 Experimental details

5.4.1 General information

All chemicals were used as received without any further purification. Rhodamine B (≥95%) and methylene blue were purchased from Sigma-Aldrich. Ethanol (>99.9%) was purchased from VWR Chemicals.

5.4.2 Methods

Photochemical dye degradation – In general, $3.77 \cdot 10^{-2}$ mmol (40 mg, depending on the compound) of DP powder was transferred to a 20 mL glass vial. Next, 20 mL of an ethanoic dye solution was added. The initial dye concentration was different depending on the dye. In case of RhB it was 100 mg/L while for MB the concentration was 10 mg/L. The DP was first allowed to reach adsorption/desorption equilibrium with the dye in solution by stirring the solution for 1 hour at 500 RPM in the dark. To study the photoactivity over time aliquots were taken at different time intervals when illuminating the mixture. This was typically done by taking 1.5 mL from the suspension and diluting it with 1.5 mL ethanol. To separate the DP powder from the suspension the diluted aliquot was centrifuged for 5 minutes at 1,000 RPM. In case of RhB, the PL of the supernatant was measured with an Ocean Insight FLAME-T-VIS-NIR-ES spectrometer combined with a 405 nm excitation source. For MB, the supernatant was studied using UV-Vis absorption spectroscopy (Agilent Technologies Cary 60 UV-Vis Spectrophotometer). After taking the first aliquot, the light source was turned on, which was located approximately 13 cm from the sample solution. The process of taking an aliquot, diluting, centrifugation, and measuring the PL or absorption was performed every 20 minutes for a duration of 180 minutes. See Table S1 for an inventory of the performed dye degradation experiments.

Chapter 6. Conclusions and outlook

We aimed to develop photoactive thin films for photochemical CO_2 reduction, based on the double perovskite $Cs_2AgBiBr_6$. For this, we first explored the (full) exchange of Bi^{3+} with Sb^{3+} in CABB thin films to reduce the bandgap energy, thus increasing the light absorption in the visible part of the spectrum. The dropwise addition of an antisolvent during the spin coating process enabled us to obtain smooth CABB thin films with a high surface coverage. However, we found by means of SEM that with an increased Sb-content in the film, the surface packing of crystal grains is reduced. This is be attributed to the poor dissolution of $SbBr_3$ in DMSO, which was mostly evident for Sb concentrations > 50%. Next, we performed photochemical CO_2 reduction experiments with CABB thin films and control experiments (*i.e.*, with an empty cell and clean substrate). We discovered that the low photoactivity towards CO_2 reduction was not induced by the DP, but most likely by a contamination in the photocatalytic cell. We also explored a selection of different charge transport layers (*i.e.*, TiO_2, ZnO, and NiO_x) that allow for a better separation of photogenerated charges, and hence would improve the efficiency of photochemical reactions. We found that TiO_2 would be an unsuitable carrier layer for CABB-based DP thin films since it requires annealing at temperatures at which CABB decomposes. Regarding NiO_x and ZnO, further investigation is needed to determine whether they will be suitable for their use in CABB-based photochemical devices. Since the synthesis of Sb-alloyed thin films proved challenging, combined with the fact that the CABB films showed no significant photoactivity towards CO_2 conversion, we shifted the focus of our work to other routes to synthesize alloyed CABB.

We first studied the solution-based synthesis of CABB and CASB in HBr. This method delivered crystalline and phase-pure CABB crystals and nearly phase-pure crystalline CASB crystals. To circumvent the use of solvents and to facilitate the exploration of a variety of alloys, we used a solid-state mechanochemical approach, yielding phase-pure DPs with varying compositions. In this work, Bi^{3+} was (partially) exchanged with Sb^{3+}, In^{3+}, Fe^{3+}, Al^{3+}, Sn^{2+}, and Ti^{4+} using a ball mixer. The X-ray reflection angles of these DPs matched well with the elpasolite crystal structure, and from the lattice plane reflections we also yielded information regarding the lattice constant of the DP composites. We observe a general trend of shrinkage of the lattice constant when Bi^{3+} is exchanged with a smaller cation, whereas the lattice constant expands with the exchange of a larger cation. One interesting exception on this is the exchange of Bi^{3+} with the smaller Al^{3+}, where the lattice constant in fact increases. The exact cause of this discrepancy remains unclear, however. Analysis of the optical properties revealed that the cationic substitutions have a significant effect on the absorption of the DP. To emphasize, the light absorption redshifted towards the infrared part of the visible spectrum when Fe^{3+} was used a substituent. However, in-depth crystallography analysis revealed that the lattice constant does not decrease linearly with increasing Fe-alloying, indicating that there is a limit to the alloying concentration of Fe^{3+} into the CABB structure. These considerations strongly suggest the presence of leftover $FeBr_3$ after the ball milling synthesis. To establish the effect of alloying on the photochemical activity of CABB, we tested these various DPs in a model reaction.

As a model reaction we used dye degradation with RhB and MB, respectively. The degradation of the dyes was monitored by measuring the PL of RhB and absorption of MB over the course of several hours. During the experiment, a suspension of DP powder in an ethanoic solution of the respective dye was illuminated with either simulated sunlight, blue light (455 nm) or green light (518 nm). For RhB degradation under simulated sunlight and blue light irradiation, we find that CABB is the superior photoactive material compared to the other DP composites. Since the RhB absorption partially overlaps with the green light emission, we were unable to test the effect of improved absorption towards the red part of the spectrum of DPs on the photochemical activity. MB, having an absorption which does not overlap with either blue or green light emission was used next. Interestingly for MB degradation under green light irradiation, the decay rate is enhanced when Bi^{3+} is exchanged with 1% Fe^{3+}, 10% Fe^{3+}, 15% Ti^{4+}, and 50% In^{3+}, respectively. The Fe- and Ti-based DPs shift the absorption to higher wavelengths, thus increasing the light absorption efficiency of the material. Interestingly, the In-based composite also shows an improved degradation rate, despite the blueshift of absorption as opposed to CABB. It is likely that the MB absorption decrease is not only governed by dye degradation but also by the MB adsorption. Further investigation of the photochemical activity of 1% and 10% Fe-alloyed DPs reveals that the MB degradation rate under blue light illumination of these DPs is also improved compared to CABB.

The improved photochemical activity of CABB alloyed with Fe^{3+} paves a way to study these materials to a greater extend. However, one should also consider the presence of unreacted precursors and the stability of the DPs in reaction conditions. Furthermore, future research should focus on improving the understanding of the dye degradation process and how CABB plays a part in photochemical reactions. The better understanding allows for a more directed search of other dopants to improve the photochemical activity, as well as maintaining the excellent chemical stability of CABB. In addition, the photochemical activity towards other reactions should be considered. For example, we attempted to reduce CO_2 using DP thin films. However, using other deposition techniques, such as vacuum or laser deposition, one could enable the fabrication of DP thin films of a broad range of different alloys. One of the added benefits of thin films compared to bulk powders are the advanced spectroscopic techniques that can be employed to characterize the DP films. In addition, thin films can be applied to nearly all surfaces, making it a viable route for future applications, while powder-based applications are limited.

Chapter 7. Acknowledgements

I want to thank Huygen Jöbsis MSc. for his excellent daily guidance and supervision throughout the project. His help and support motivated me to successfully complete this research project. Huygens hands-on guidance and knowledge on the perovskite-related topic has had a major contribution in the success of this work. I would also like to thank dr. Eline Hutter for accepting me in the Photochemistry research group as part of my Master thesis. I have learned a lot from our project-related discussions and supporting feedback she provided on my research. I also thank the members of the Photochemistry group for all the lively discussions and interesting suggestions during the meetings. Finally, I want to thank dr. Celso de Mello Donegá for taking the time to be my second examiner.

Chapter 8. References

1. Roy, S. C., Varghese, O. K., Paulose, M. & Grimes, C. A. Toward solar fuels: Photocatalytic conversion of carbon dioxide to hydrocarbons. *ACS Nano* vol. 4 1259–1278 (2010).
2. Wu, J., Huang, Y., Ye, W. & Li, Y. CO2 Reduction: From the Electrochemical to Photochemical Approach. *Advanced Science* vol. 4 (2017).
3. Zhang, Z., Li, Z., Meng, L., Lien, S. Y. & Gao, P. Perovskite-Based Tandem Solar Cells: Get the Most Out of the Sun. *Advanced Functional Materials* vol. 30 (2020).
4. Menedjhi, A., Bouarissa, N., Saib, S. & Bouamama, K. Halide double perovskite Cs2AgInBr6 for photovoltaic's applications: Optical properties and stability. *Optik (Stuttg)* **243**, (2021).
5. Gao, W. *et al.* High-Quality Cs2AgBiBr6 Double Perovskite Film for Lead-Free Inverted Planar Heterojunction Solar Cells with 2.2 % Efficiency. *ChemPhysChem* **19**, 1696–1700 (2018).
6. Wu, D. *et al.* High visible-light photocatalytic performance of stable lead-free Cs2AgBiBr6 double perovskite nanocrystals. *Journal of Catalysis* **397**, 27–35 (2021).
7. Zhou, L., Xu, Y. F., Chen, B. X., Kuang, D. bin & Su, C. Y. Synthesis and Photocatalytic Application of Stable Lead-Free Cs2AgBiBr6 Perovskite Nanocrystals. *Small* **14**, (2018).
8. Hutter, E. M., Gélvez-Rueda, M. C., Bartesaghi, D., Grozema, F. C. & Savenije, T. J. Band-Like Charge Transport in Cs2AgBiBr6 and Mixed Antimony-Bismuth Cs2AgBi1-xSbxBr6 Halide Double Perovskites. *ACS Omega* **3**, 11655–11662 (2018).
9. Li, Z. *et al.* Bandgap lowering in mixed alloys of Cs2Ag(SbxBi1-x)Br6 double perovskite thin films. *Journal of Materials Chemistry A* **8**, 21780–21788 (2020).
10. Noyes, W. A. & Kassel, L. S. A REVIEW OF PHOTOCHEMISTRY. *Chem. Rev* **3**, 199–225 (1926).
11. Cook, T. R. *et al.* Solar energy supply and storage for the legacy and nonlegacy worlds. *Chemical Reviews* **110**, 6474–6502 (2010).
12. Liu, B., Zhao, X., Terashima, C., Fujishima, A. & Nakata, K. Thermodynamic and kinetic analysis of heterogeneous photocatalysis for semiconductor systems. *Physical Chemistry Chemical Physics* vol. 16 8751–8760 (2014).
13. Hamza El-Saba, M. Chapter 5 Energy Band Theory & Classification of Solids. in (2015).
14. Hook, J. R. & Hall, H. E. *Solid State Physics*. (1991).
15. Muckel, F. *et al.* Exciton-driven change of phonon modes causes strong temperature dependent bandgap shift in nanoclusters. *Nature Communications* **11**, (2020).

16. de Mello Donegá, C. *Nanoparticles: Workhorses of nanoscience*. *Nanoparticles: Workhorses of Nanoscience* vol. 9783662448236 (Springer-Verlag Berlin Heidelberg, 2014).

17. Maiti, A., Chatterjee, S., Peedikakkandy, L. & Pal, A. J. Defects and Their Passivation in Hybrid Halide Perovskites toward Solar Cell Applications. *Solar RRL* vol. 4 (2020).

18. Gerhard, M. *et al.* Microscopic insight into non-radiative decay in perovskite semiconductors from temperature-dependent luminescence blinking. *Nature Communications* **10**, (2019).

19. Bisquert, J. *The Physics of Solar Cells Perovskites, Organics, and Photovoltaic Fundamentals*. (2018).

20. Yuan, J., Liu, H., Wang, S. & Li, X. How to apply metal halide perovskites to photocatalysis: Challenges and development. *Nanoscale* vol. 13 10281–10304 (2021).

21. Dey, A. *et al.* State of the Art and Prospects for Halide Perovskite Nanocrystals. *ACS Nano* vol. 15 10775–10981 (2021).

22. Hirakawa, T. & Kamat, P. v. Charge separation and catalytic activity of Ag@TiO2 core-shell composite clusters under UV-irradiation. *J Am Chem Soc* **127**, 3928–3934 (2005).

23. Hirakawa, T. & Kamat, P. v. Photoinduced electron storage and surface plasmon modulation in Ag@TiO2 clusters. *Langmuir* **20**, 5645–5647 (2004).

24. Zhang, Z. *et al.* Stable and Highly Efficient Photocatalysis with Lead-Free Double-Perovskite of Cs2AgBiBr6. *Angewandte Chemie* **131**, 7341–7345 (2019).

25. Jang, Y. J. *et al.* Unbiased Sunlight-Driven Artificial Photosynthesis of Carbon Monoxide from CO2 Using a ZnTe-Based Photocathode and a Perovskite Solar Cell in Tandem. *ACS Nano* **10**, 6980–6987 (2016).

26. Xu, K. *et al.* Hydrogen from wet air and sunlight in a tandem photoelectrochemical cell. *International Journal of Hydrogen Energy* **44**, 587–593 (2019).

27. Liu, D. & Kelly, T. L. Perovskite solar cells with a planar heterojunction structure prepared using room-temperature solution processing techniques. *Nature Photonics* **8**, 133–138 (2014).

28. Huang, H., Pradhan, B., Hofkens, J., Roeffaers, M. B. J. & Steele, J. A. Solar-Driven Metal Halide Perovskite Photocatalysis: Design, Stability, and Performance. *ACS Energy Letters* vol. 5 1107–1123 (2020).

29. Chilvery, A., Das, S., Guggilla, P., Brantley, C. & Sunda-Meya, A. A perspective on the recent progress in solution-processed methods for highly efficient perovskite solar cells. *Science and Technology of Advanced Materials* vol. 17 650–658 (2016).

30. Green, M. A., Ho-Baillie, A. & Snaith, H. J. The emergence of perovskite solar cells. *Nature Photonics* vol. 8 506–514 (2014).

31. Kojima, A., Teshima, K., Shirai, Y. & Miyasaka, T. Organometal halide perovskites as visible-light sensitizers for photovoltaic cells. *J Am Chem Soc* **131**, 6050–6051 (2009).

32. Etgar, L. *et al.* Mesoscopic CH3NH3PbI3/TiO2 heterojunction solar cells. *J Am Chem Soc* **134**, 17396–17399 (2012).

33. Gourji, F. H. & Velauthapillai, D. A review on Cs-based Pb-free double halide perovskites: From theoretical and experimental studies to doping and applications. *Molecules* vol. 26 (2021).

34. Zhao, X. G. *et al.* Design of Lead-Free Inorganic Halide Perovskites for Solar Cells via Cation-Transmutation. *J Am Chem Soc* **139**, 2630–2638 (2017).

35. Lei, H., Hardy, D. & Gao, F. Lead-Free Double Perovskite Cs2AgBiBr6: Fundamentals, Applications, and Perspectives. *Advanced Functional Materials* vol. 31 (2021).

36. Bartel, C. J. *et al.* New tolerance factor to predict the stability of perovskite oxides and halides. *Science Advances* **5**, (2019).

37. Fedorovskiy, A. E., Drigo, N. A. & Nazeeruddin, M. K. The Role of Goldschmidt's Tolerance Factor in the Formation of A2BX6 Double Halide Perovskites and its Optimal Range. *Small Methods* **4**, (2020).

38. Goldschmidt, V. M. Die Gesetze der Krystallochemie. *Naturwissenschaften* **14**, 477–485 (1926).

39. Zhao, X. G. *et al.* Design of Lead-Free Inorganic Halide Perovskites for Solar Cells via Cation-Transmutation. *J Am Chem Soc* **139**, 2630–2638 (2017).

40. Li, L. *et al.* Studies on the regularity of perovskite formation via machine learning. *Computational Materials Science* **199**, (2021).

41. Greul, E., Petrus, M. L., Binek, A., Docampo, P. & Bein, T. Highly stable, phase pure Cs2AgBiBr6 double perovskite thin films for optoelectronic applications. *Journal of Materials Chemistry A* **5**, 19972–19981 (2017).

42. García-Espejo, G., Rodríguez-Padrón, D., Luque, R., Camacho, L. & de Miguel, G. Mechanochemical synthesis of three double perovskites: Cs2AgBiBr6, (CH3NH3)2TlBiBr6 and Cs2AgSbBr6. *Nanoscale* **11**, 16650–16657 (2019).

43. Ji, F. *et al.* Lead-Free Halide Double Perovskite Cs2AgBiBr6 with Decreased Band Gap. *Angewandte Chemie - International Edition* **59**, 15191–15194 (2020).

44. Slavney, A. H., Hu, T., Lindenberg, A. M. & Karunadasa, H. I. A Bismuth-Halide Double Perovskite with Long Carrier Recombination Lifetime for Photovoltaic Applications. *J Am Chem Soc* **138**, 2138–2141 (2016).

45. Hong, Z. *et al.* Completely Solvent-free Protocols to Access Phase-Pure, Metastable Metal Halide Perovskites and Functional Photodetectors from the Precursor Salts. *iScience* **16**, 312–325 (2019).

46. Tan, D. & García, F. Main group mechanochemistry: from curiosity to established protocols. *Chemical Society Reviews* vol. 48 2274–2292 (2019).

47. Rodkey, N. *et al.* Pulsed Laser Deposition of Cs2AgBiBr6: From Mechanochemically Synthesized Powders to Dry, Single-Step Deposition. *Chemistry of Materials* **33**, 7417–7422 (2021).

48. Pantaler, M., Fettkenhauer, C., Nguyen, H. L., Anusca, I. & Lupascu, D. C. Deposition routes of Cs2AgBiBr6 double perovskites for photovoltaic applications. in *MRS Advances* vol. 3 1819–1823 (Materials Research Society, 2018).

49. Gong, J. & Krishnan, S. Mathematical modeling of dye-sensitized solar cells. in *Dye-Sensitized Solar Cells: Mathematical Modelling, and Materials Design and Optimization* 51–81 (Elsevier, 2019). doi:10.1016/B978-0-12-814541-8.00002-1.

50. Sebastiá-Luna, P. *et al.* Tuning the Optical Absorption of Sn-, Ge-, and Zn-Substituted Cs2AgBiBr6 Double Perovskites: Structural and Electronic Effects. *Chemistry of Materials* **33**, 8028–8035 (2021).

51. Du, K., Meng, W., Wang, X., Yan, Y. & Mitzi, D. B. Bandgap Engineering of Lead-Free Double Perovskite Cs2AgBiBr6 through Trivalent Metal Alloying. *Angewandte Chemie* **129**, 8270–8274 (2017).

52. Zhang, Z. *et al.* Improvement of Cs2AgBiBr6 double perovskite solar cell by rubidium doping. *Organic Electronics* **74**, 204–210 (2019).

53. Lamba, R. S., Basera, P., Singh, S., Bhattacharya, S. & Sapra, S. Lead-Free Alloyed Double-Perovskite Nanocrystals of Cs2(NaxAg1-x)BiBr6 with Tunable Band Gap. *Journal of Physical Chemistry C* (2021) doi:10.1021/acs.jpcc.0c09554.

54. Gray, M. B., McClure, E. T. & Woodward, P. M. Cs2AgBiBr6-: XClx solid solutions-band gap engineering with halide double perovskites. *Journal of Materials Chemistry C* **7**, 9686–9689 (2019).

55. Lindquist, K. P. *et al.* Tuning the bandgap of Cs2AgBiBr6 through dilute tin alloying. *Chemical Science* **10**, 10620–10628 (2019).

56. Ma, X., Li, Z. & Yang, J. Efficient Direct Band Gap Photovoltaic Material Predicted Via Doping Double Perovskites Cs2AgBiX6 (X = Cl, Br). *Journal of Physical Chemistry C* **125**, 10868–10875 (2021).

57. Torrent, J. & Barrón, V. Diffuse Reflectance Spectroscopy. in *Methods of Soil Analysis. Part 5. Mineralogical Methods* (Soil Science Society of America, 2008).

58. Kubelka, P. & Munk, F. *An Article on Optics of Paint Layers*. (1931).

59. López, R. & Gómez, R. Band-gap energy estimation from diffuse reflectance measurements on sol-gel and commercial TiO2: A comparative study. *Journal of Sol-Gel Science and Technology* **61**, 1–7 (2012).

60. Kelly, A. (Anthony) & Knowles, K. M. *Crystallography and crystal defects*. (Wiley, 2012).

61. Bragg, W. H. The reflection of X-rays by crystals. *Royal Society* **88**, (1913).

62. Jiang, P. *et al.* Unprecedented lattice volume expansion on doping stereochemically active Pb2+ into uniaxially strained structure of CaBa1−xPbxZn2Ga2O7. *Nature Communications* **11**, (2020).

63. Cullity, B. D. & Stock, S. R. *Elements of X-ray diffraction*. (Prentice-Hall, 2001).

64. Saowadee, N., Agersted, K. & Bowen, J. R. Lattice constant measurement from electron backscatter diffraction patterns. *Journal of Microscopy* **266**, 200–210 (2017).

65. Scherrer, P. Bestimmung der inneren Struktur und der Größe von Kolloidteilchen mittels Röntgenstrahlen. *Göttinger Nachrichten Gesell.* **2**, 98–100 (1918).

66. Miranda, M. A. R. & Sasaki, J. M. The limit of application of the Scherrer equation. *Acta Crystallographica Section A: Foundations and Advances* **74**, 54–65 (2018).

67. Muniz, F. T. L., Miranda, M. A. R., Morilla Dos Santos, C. & Sasaki, J. M. The Scherrer equation and the dynamical theory of X-ray diffraction. *Acta Crystallographica Section A: Foundations and Advances* **72**, 385–390 (2016).

68. Yang, H. & Yang, J. Photocatalytic degradation of rhodamine B catalyzed by TiO2 films on a capillary column. *RSC Advances* **8**, 11921–11929 (2018).

69. Wang, B. *et al.* Ionic liquid-induced strategy for porous perovskite-like PbBiO2Br photocatalysts with enhanced photocatalytic activity and mechanism insight. *Applied Catalysis B: Environmental* **206**, 127–135 (2017).

70. Al-Kahtani, A. A. Photocatalytic Degradation of Rhodamine B Dye in Wastewater Using Gelatin/CuS/PVA Nanocomposites under Solar Light Irradiation. *Journal of Biomaterials and Nanobiotechnology* **08**, 66–82 (2017).

71. Houas, A. *et al. Photocatalytic degradation pathway of methylene blue in water*. *Applied Catalysis B: Environmental* vol. 31 (2001).

72. Yu, Z. & Chuang, S. S. C. Probing methylene blue photocatalytic degradation by adsorbed ethanol with in situ IR. *Journal of Physical Chemistry C* **111**, 13813–13820 (2007).

73. Asahi, R., Morikawa, T., Ohwaki, T., Aoki, K. & Taga, Y. Visible-light photocatalysis in nitrogen-doped titanium oxides. *Science (1979)* **293**, 269–271 (2001).

74. Liang, L. *et al.* Efficiency and mechanisms of rhodamine B degradation in Fenton-like systems based on zero-valent iron. *RSC Advances* **10**, 28509–28515 (2020).

75. Wright, A. D. *et al.* Ultrafast Excited-State Localization in Cs2AgBiBr6 Double Perovskite. *Journal of Physical Chemistry Letters* **12**, 3352–3360 (2021).

76. Li, K. *et al.* Highly-efficient and stable photocatalytic activity of lead-free Cs2AgInCl6 double perovskite for organic pollutant degradation. *Journal of Colloid and Interface Science* **596**, 376–383 (2021).

77. Wang, C. *et al.* Reaction kinetics of photocatalytic degradation of sulfosalicylic acid using TiO2 microspheres. *Journal of Hazardous Materials* **163**, 1101–1106 (2009).

78. Mahdiani, M., Soofivand, F., Ansari, F. & Salavati-Niasari, M. Grafting of CuFe12O19 nanoparticles on CNT and graphene: Eco-friendly synthesis, characterization and photocatalytic activity. *Journal of Cleaner Production* **176**, 1185–1197 (2018).

79. Kamat, P. v. Holy Grails of Solar Photochemistry. *ACS Energy Letters* vol. 1 1273–1274 (2016).

80. Chen, P., Huang, Y., Shi, Z., Chen, X. & Li, N. Improving the catalytic CO2 reduction on Cs2AgBiBr6 by halide defect engineering: A DFT study. *Materials* **14**, (2021).

81. Wang, Y. *et al.* Lead-free perovskite Cs2AgBiBr6@g-C3N4 Z-scheme system for improving CH4 production in photocatalytic CO2 reduction. *Applied Catalysis B: Environmental* **282**, (2021).

82. Liu, Z. *et al.* Synthesis of lead-free Cs2AgBix6 (X = Cl, Br, I) double perovskite nanoplatelets and their application in CO2 photocatalytic reduction. *Nano Letters* **21**, 1620–1627 (2021).

83. Kumar, S. *et al.* Mechanochemically synthesized Pb-free halide perovskite-based Cs2AgBiBr6-Cu-RGO nanocomposite for photocatalytic CO2 reduction. *Journal of Materials Chemistry A* **9**, 12179–12187 (2021).

84. Liu, L., Zhao, H., Andino, J. M. & Li, Y. Photocatalytic CO2 reduction with H2O on TiO2 nanocrystals: Comparison of anatase, rutile, and brookite polymorphs and exploration of surface chemistry. *ACS Catalysis* **2**, 1817–1828 (2012).

85. Zhao, D. *et al.* Facile deposition of high-quality Cs2AgBiBr6 films for efficient double perovskite solar cells. *Science China Materials* **63**, 1518–1525 (2020).

86. Li, Z. *et al.* Understanding the Role of Grain Boundaries on Charge-Carrier and Ion Transport in Cs2AgBiBr6 Thin Films. *Advanced Functional Materials* **31**, (2021).

87. Sirtl, M. T. *et al.* The Bottlenecks of Cs2AgBiBr6 Solar Cells: How Contacts and Slow Transients Limit the Performance. *Advanced Optical Materials* **9**, (2021).

88. Jöbsis, H. J. *et al.* Recombination and localization: Unfolding the pathways behind conductivity losses in Cs2AgBiBr6 thin films. *Applied Physics Letters* **119**, (2021).

89. Connor, B. A., Leppert, L., Smith, M. D., Neaton, J. B. & Karunadasa, H. I. Layered halide double perovskites: Dimensional reduction of Cs2AgBiBr6. *J Am Chem Soc* **140**, 5235–5240 (2018).

90. Wei, F. *et al.* Enhanced visible light absorption for lead-free double perovskite Cs2AgSbBr6. *Chemical Communications* **55**, 3721–3724 (2019).

91. Creutz, S. E., Crites, E. N., de Siena, M. C. & Gamelin, D. R. Colloidal Nanocrystals of Lead-Free Double-Perovskite (Elpasolite) Semiconductors: Synthesis and Anion Exchange to Access New Materials. *Nano Letters* **18**, 1118–1123 (2018).

92. Sun, S. *et al.* Accelerated Development of Perovskite-Inspired Materials via High-Throughput Synthesis and Machine-Learning Diagnosis. *Joule* **3**, 1437–1451 (2019).

93. Warren, B. E. *X-RAY DETERMINATION OF THE STRUCTURE OF GLASS**. (1934).

94. Schmidbauer, M. *et al. Diffuse scattering from interface roughness in grazing-incidence x-ray diffraction*. *Article in Physical Review B* https://www.researchgate.net/publication/259383497 (1996).

95. Kumar, P. *et al.* Microwave spin resonance investigation on the effect of the post-processing annealing of CoFe2O4 nanoparticles. *Nanoscale Advances* **2**, 1939–1948 (2020).

96. Rigter, S. A. *et al.* Passivation Properties and Formation Mechanism of Amorphous Halide Perovskite Thin Films. *Advanced Functional Materials* **31**, (2021).

97. Tauc, J. Optical properties and electronic structure of amorphous Ge and Si. *Mat. Res. Bull* **3**, 37–46 (1967).

98. Lubarda, V. A. On the effective lattice parameter of binary alloys. *Mechanics of Materials* **35**, 53–68 (2003).

99. Wang, W. N. *et al.* Size and structure matter: Enhanced CO2 photoreduction efficiency by size-resolved ultrafine Pt nanoparticles on TiO2 single crystals. *J Am Chem Soc* **134**, 11276–11281 (2012).

100. Newbury, D. E. & Ritchie, N. W. M. Is scanning electron microscopy/energy dispersive X-ray spectrometry (SEM/EDS) quantitative? *Scanning* **35**, 141–168 (2013).

101. Michalak, I., Chojnacka, K. & Marycz, K. Using ICP-OES and SEM-EDX in biosorption studies. *Microchimica Acta* **172**, 65–74 (2011).

102. Kuhl, K. P., Cave, E. R., Abram, D. N. & Jaramillo, T. F. New insights into the electrochemical reduction of carbon dioxide on metallic copper surfaces. *Energy and Environmental Science* **5**, 7050–7059 (2012).

103. Yu, Z. & Sun, L. Inorganic Hole-Transporting Materials for Perovskite Solar Cells. *Small Methods* vol. 2 (2018).

104. Shinen, M. H., Alsaati, S. A. A. & Razooqi, F. Z. Preparation of high transmittance TiO2 thin films by sol-gel technique as antireflection coating. in *Journal of Physics: Conference Series* vol. 1032 (Institute of Physics Publishing, 2018).

105. Mursal, Irhamni, Bukhari & Jalil, Z. Structural and Optical Properties of Zinc Oxide (ZnO) based Thin Films Deposited by Sol-Gel Spin Coating Method. in *Journal of Physics: Conference Series* vol. 1116 (Institute of Physics Publishing, 2018).

106. Su, J., Huang, Y. qiang, Chen, H. & Huang, J. Solution Growth and Performance Study of Cs2AgBiBr6 Single Crystal. *Crystal Research and Technology* **55**, (2020).

107. Liu, S. *et al.* Nickel oxide hole injection/transport layers for efficient solution-processed organic light-emitting diodes. *Chemistry of Materials* **26**, 4528–4534 (2014).

108. Abdullah, M. A. R. *et al.* Preparation of nickel oxide thin films at different annealing temperature by sol-gel spin coating method. in *AIP Conference Proceedings* vol. 1733 (American Institute of Physics Inc., 2016).

109. Danks, A. E., Hall, S. R. & Schnepp, Z. The evolution of "sol-gel" chemistry as a technique for materials synthesis. *Materials Horizons* **3**, 91–112 (2016).

110. Manders, J. R. *et al.* Solution-Processed Nickel Oxide Hole Transport Layers in High Efficiency Polymer Photovoltaic Cells. *Advanced Functional Materials* **23**, 2993–3001 (2013).

111. Pacholski, C., Kornowski, A. & Weller, H. *Self-Assembly of ZnO: From Nanodots to Nanorods*. *Angew. Chem. Int. Ed* vol. 41 www.ccdc.cam.ac.uk/conts/ (2002).

112. Bao, X. *et al.* High-performance inverted planar perovskite solar cells without a hole transport layer via a solution process under ambient conditions. *Journal of Materials Chemistry A* **3**, 19294–19298 (2015).

113. Hou, P. *et al.* Precursor engineering for high-quality Cs2AgBiBr6 films toward efficient lead-free double perovskite solar cells. *Journal of Materials Chemistry C* **9**, 9659–9669 (2021).

114. Hoye, R. L. Z. *et al.* Fundamental Carrier Lifetime Exceeding 1 µs in Cs2AgBiBr6 Double Perovskite. *Advanced Materials Interfaces* **5**, (2018).

115. Igbari, F. *et al.* Composition Stoichiometry of Cs2AgBiBr6 Films for Highly Efficient Lead-Free Perovskite Solar Cells. *Nano Letters* **19**, 2066–2073 (2019).

116. Palazon, F., el Ajjouri, Y. & Bolink, H. J. Making by Grinding: Mechanochemistry Boosts the Development of Halide Perovskites and Other Multinary Metal Halides. *Advanced Energy Materials* vol. 10 (2020).

117. Kandel, R. *et al.* Stabilization and Solvent Driven Crystal-to-Crystal Transition between New Bismuth Halides. *Inorganic Chemistry* **59**, 7049–7055 (2020).

118. Persson, K. Materials Data on Cs3Sb2Br9 (SG:164) by Materials Project. (2014).

119. Breternitz, J. *et al.* Mechanochemical synthesis of the lead-free double perovskite Cs2[AgIn]Br6 and its optical properties. *JPhys Energy* **1**, (2019).

120. Fang, Z. *et al.* Comparison of catalytic activity of carbon-based AgBr nanocomposites for conversion of CO2 under visible light. *Journal of Saudi Chemical Society* **18**, 299–307 (2014).

121. Persson, K. Materials Data on AgBr (SG:225) by Materials Project. (2014).

122. Persson, K. Materials Data on AlBr3 (SG:14) by Materials Project. (2014).

123. Persson, K. Materials Data on CsAgBr2 (SG:63) by Materials Project. (2014).

124. ben Ghzaiel, T., Dhaoui, W., Pasko, A. & Mazaleyrat, F. Effect of non-magnetic and magnetic trivalent ion substitutions on BaM-ferrite properties synthesized by hydrothermal method. *Journal of Alloys and Compounds* **671**, 245–253 (2016).

125. Carta, C. L. The Effects of Medium on the UV-Induced Photodegradation of The Effects of Medium on the UV-Induced Photodegradation of Rhodamine B Dye Rhodamine B Dye. (2014) doi:10.21220/s2-pvy5-9w91.

126. Kontos, A. G. *et al.* Structural Stability, Vibrational Properties, and Photoluminescence in CsSnI3 Perovskite upon the Addition of SnF2. *Inorganic Chemistry* **56**, 84–91 (2017).

127. Cápiro, N. L., Stafford, B. P., Rixey, W. G., Bedient, P. B. & Alvarez, P. J. J. Fuel-grade ethanol transport and impacts to groundwater in a pilot-scale aquifer tank. *Water Research* **41**, 656–664 (2007).

128. Li, T., Zhao, X., Yang, D., Du, M. H. & Zhang, L. Intrinsic Defect Properties in Halide Double Perovskites for Optoelectronic Applications. *Physical Review Applied* **10**, (2018).

129. Hu, Y. *et al.* Role of active oxygen species in the liquid-phase photocatalytic degradation of RhB using BiVO4/TiO2 heterostructure under visible light irradiation. *Journal of Molecular Catalysis A: Chemical* **408**, 172–178 (2015).

130. Mayerhöfer, T. G., Pahlow, S. & Popp, J. The Bouguer-Beer-Lambert Law: Shining Light on the Obscure. *ChemPhysChem* (2020) doi:10.1002/cphc.202000464.

Annex

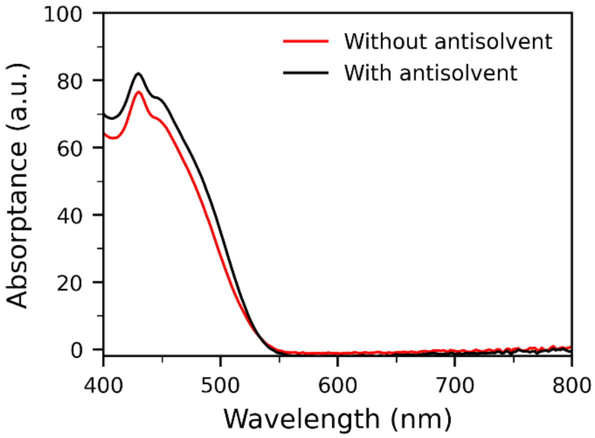

Figure S1. UV-Vis absorptance of CABB thin films spin coated without (red) and with (black) antisolvent. CABB thin film spin coated with antisolvent has a slightly higher absorptance, most likely thanks to a higher surface coverage of CABB.

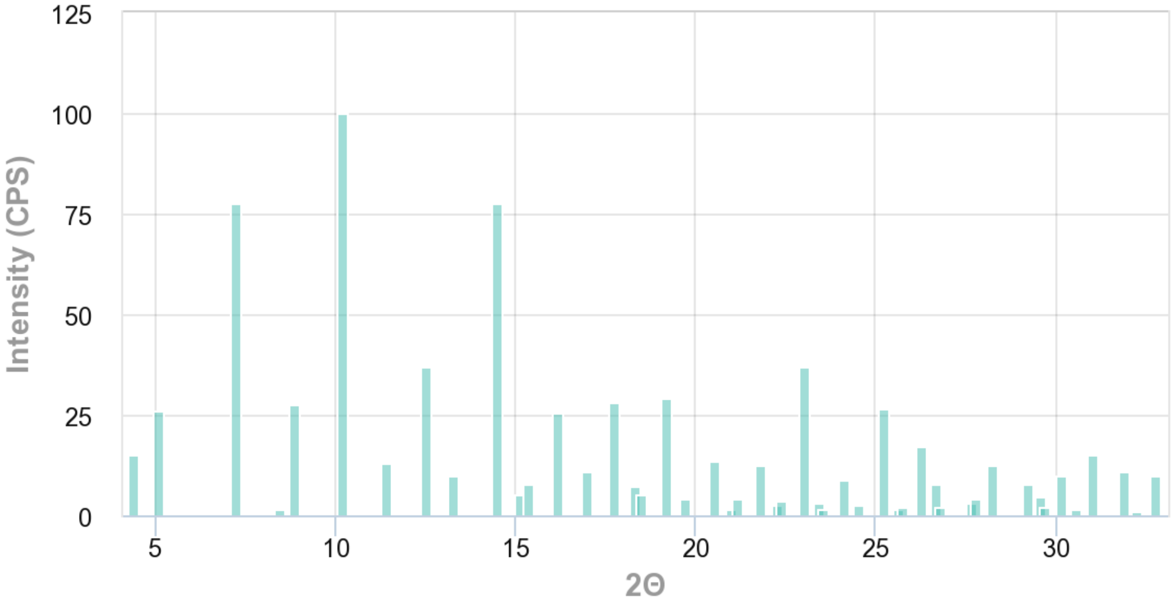

Figure S2. Calculated XRD diffractogram of Cs_3BiBr_6 (Ag radiation source). (Source: The Materials Project: mp-1112980)

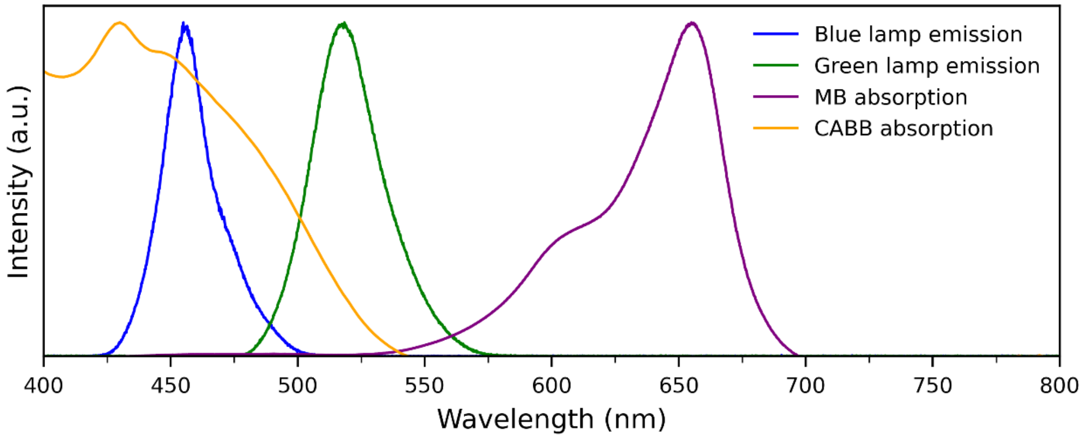

Figure S3. Graph of the different optical properties of the dye degradation experiments, namely the emission spectra of the blue and green lamp (455 nm and 518 nm, respectively), and the absorption spectra of MB and CABB.

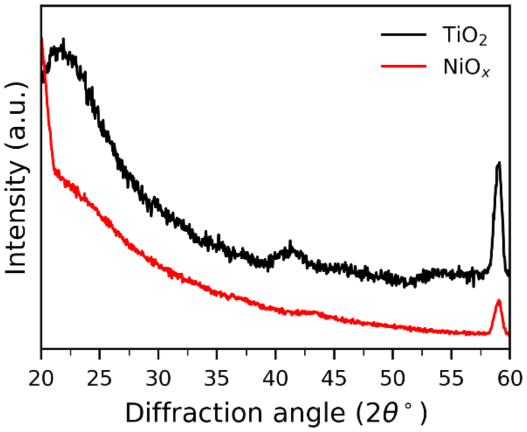

Figure S4. XRD patterns of TiO_2 (black) and NiO_x (red). No significant peaks are observed, most likely due to the small thickness of the films.

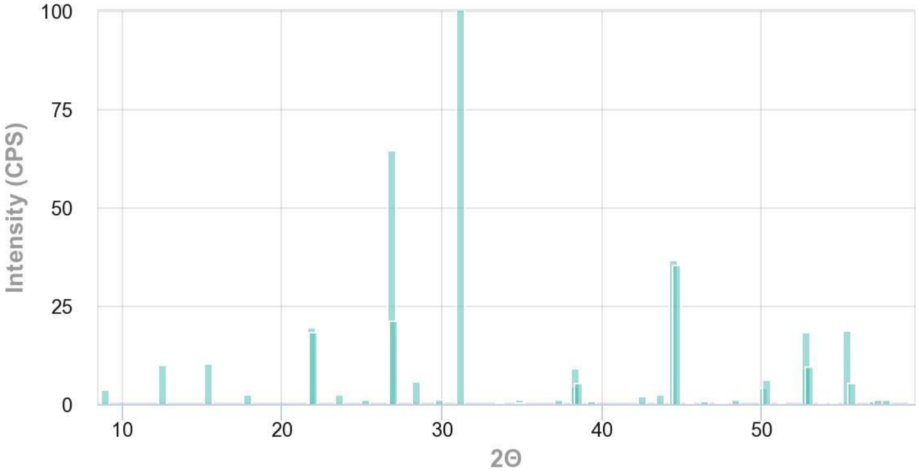

Figure S5. Calculated XRD diffractogram of $Cs_3Sb_2Br_9$ (Cu radiation source).[118]

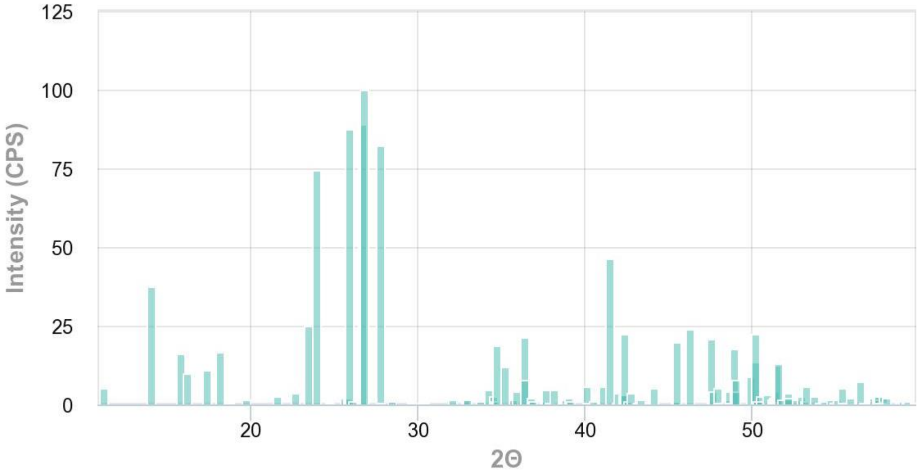

Figure S6. Calculated XRD diffractogram of $AlBr_3$ (Cu radiation source).[122]

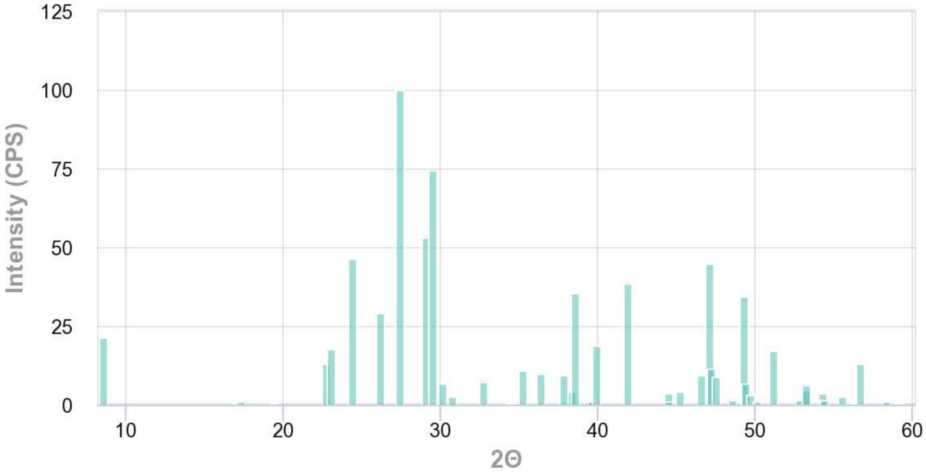

Figure S7. Calculated XRD diffractogram of $CsAgBr_2$ (Cu radiation source).[123]

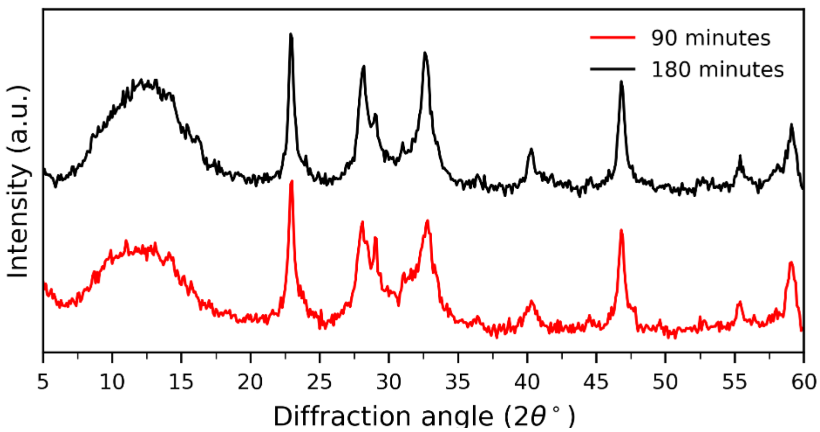

Figure S8. XRD patterns of $Cs_2AgInBr_6$ after 90 minutes of ball milling (red), and 180 minutes of ball milling (black). The diffraction peak of a secondary phase at 29° 2θ is reduced and the remaining peaks are in general sharper after extended ball milling.

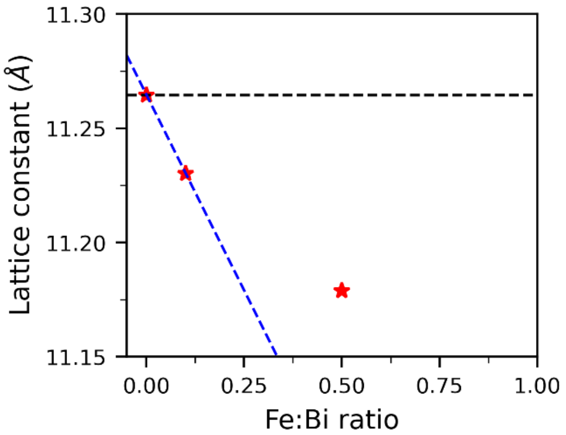

Figure S9. Plot of the mean lattice constants of Fe-alloyed CABB, revealing that the lattice constant does not decrease linearly.

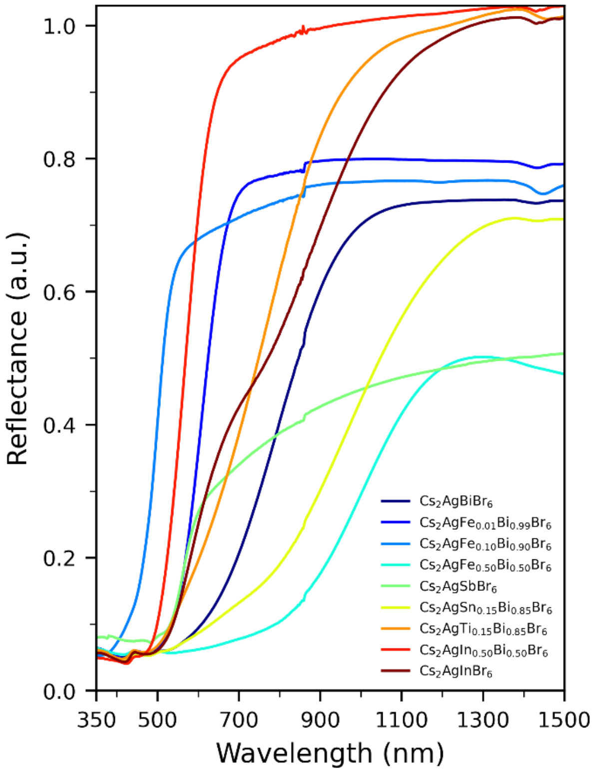

Figure S10. UV-Vis diffuse reflectance spectra of $Cs_2AgM_xBi_{1-x}Br_6$ DP composites.

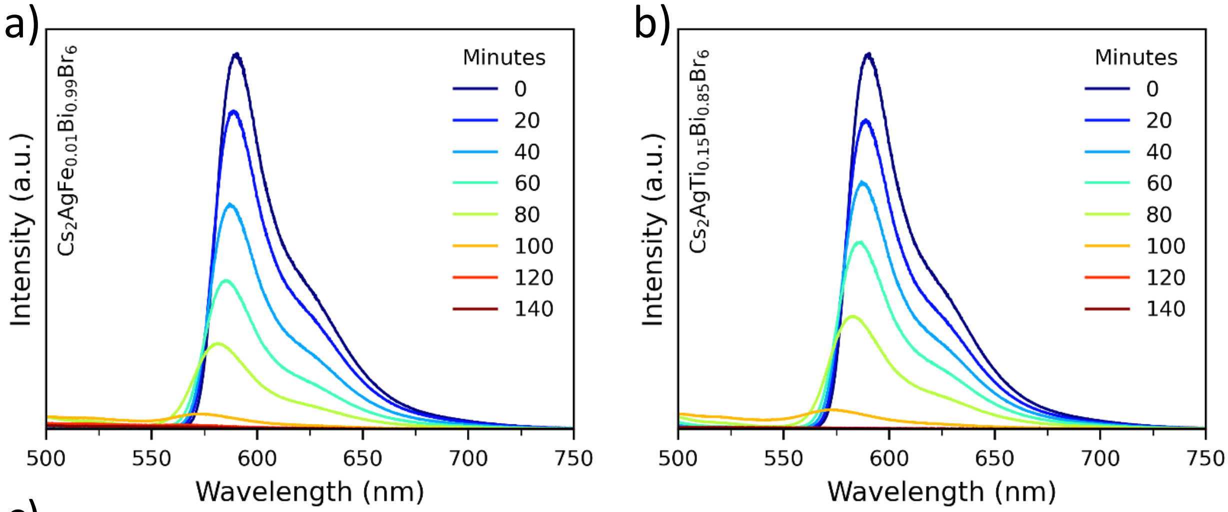

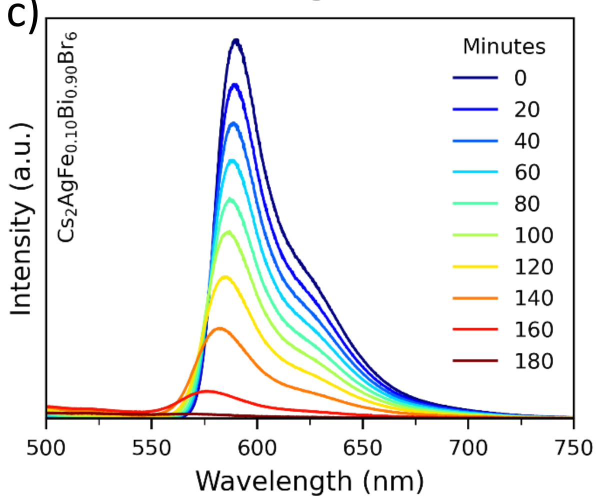

Figure S11. RhB PL decay measured over time under illumination of 455 nm light, with **a)** $Cs_2AgFe_{0.01}Bi_{0.99}Br_6$, **b)** $Cs_2AgTi_{0.15}Bi_{0.85}Br_6$ and **c)** $Cs_2AgFe_{0.10}Bi_{0.90}Br_6$.

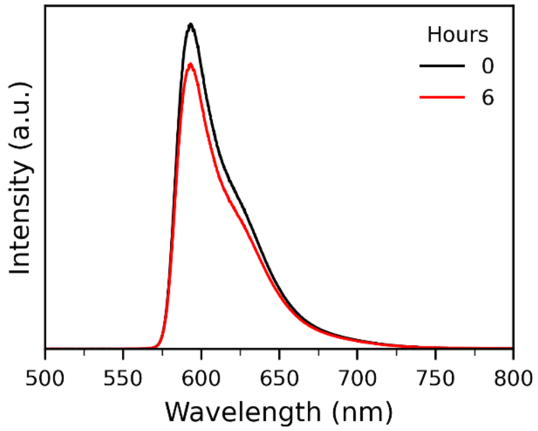

Figure S12. PL decay of RhB while exposed to 455 nm light, in the beginning (black) and after 6 hours.

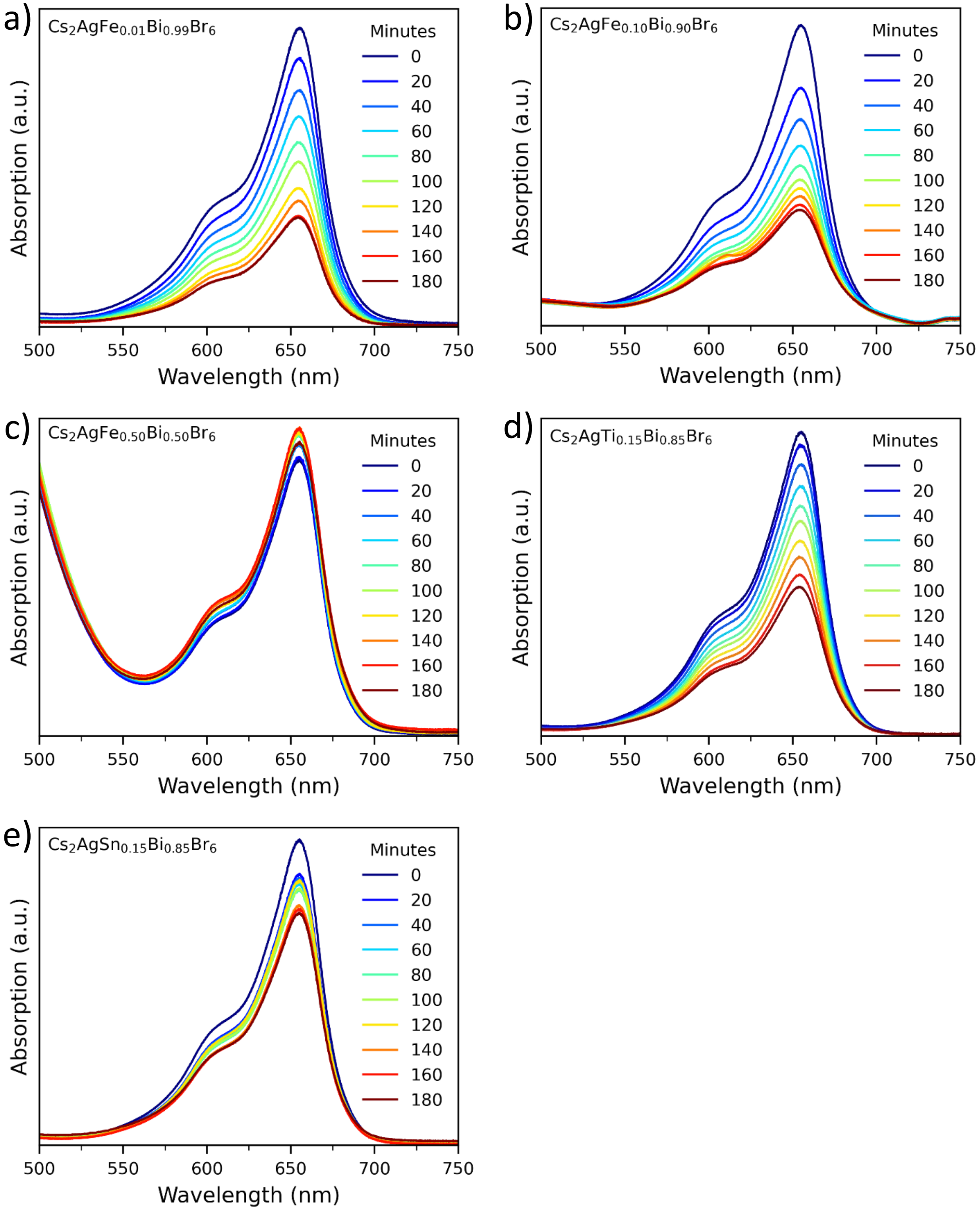

Figure S13. UV-Vis measurements recording the MB absorption decay over time under illumination of 518 nm light, with **a)** $Cs_2AgFe_{0.01}Bi_{0.99}Br_6$, **b)** $Cs_2AgFe_{0.10}Bi_{0.90}Br_6$, **c)** $Cs_2AgFe_{0.50}Bi_{0.50}Br_6$, **d)** $Cs_2AgTi_{0.15}Bi_{0.85}Br_6$ and **e)** $Cs_2AgSn_{0.15}Bi_{0.85}Br_6$.

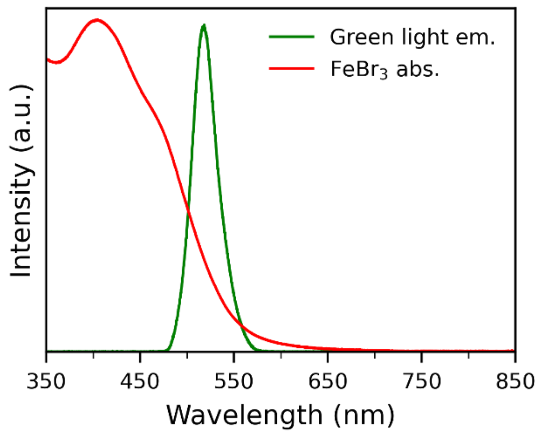

Figure S14. Comparison of green light emission (518 nm) with the absorption of FeBr$_3$, revealing the overlap of both.

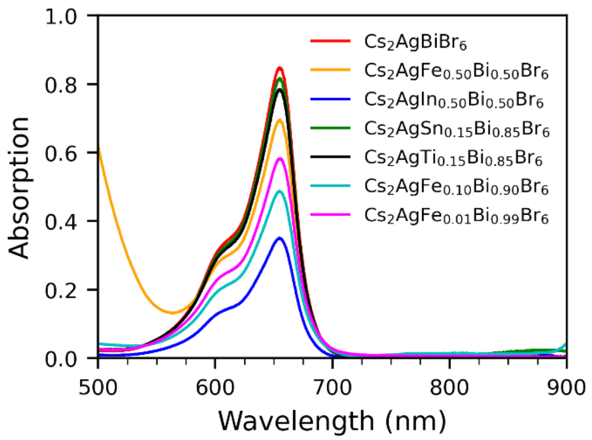

Figure S15. Absorption spectra recorded of a 10 mg/L MB solution in ethanol, with added DP composite powder (as labeled in the legend). The difference in absorption intensity is indicative of the adsorption capabilities for some of the composites.

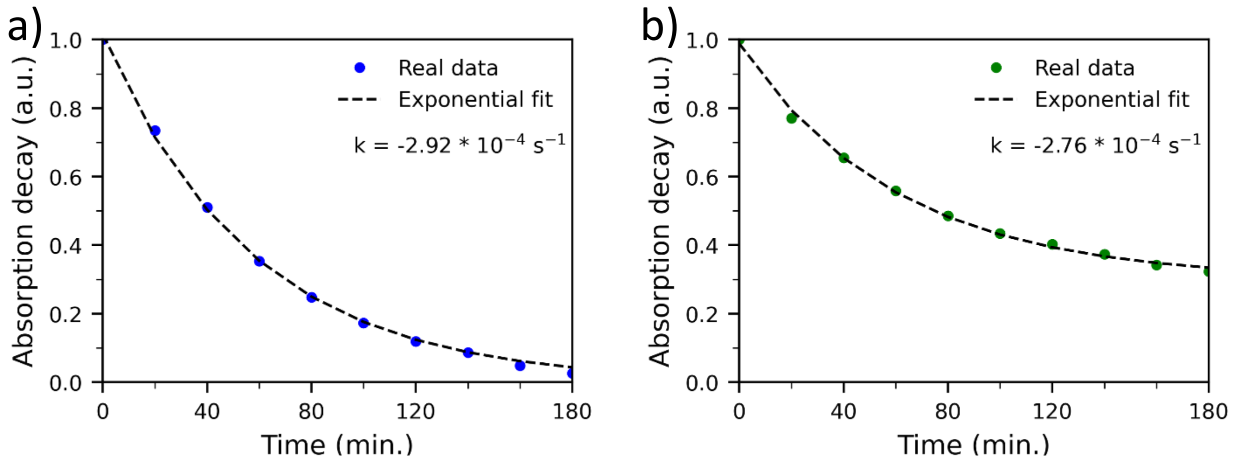

Figure S16. Mono exponential fits of the decay of MB absorption over time with Cs$_2$AgFe$_{0.10}$Bi$_{0.90}$Br$_6$, under **a)** 455 nm light exposure and **b)** 518 nm light exposure.

Table S1. Inventory of photochemical dye degradation experiments. The combination of DP composite and experimental conditions are color coded: green indicating that the combination of DP, light source and dye have been tested. Red indicates that these conditions have not been tested for the respective DP.

DP composites	Sim. sunlight / RhB	Blue light / RhB	Blue light / MB	Green light / RhB	Green light / MB
$Cs_2AgBiBr_6$	🟩	🟩	🟩	🟩	🟩
$Cs_2AgSbBr_6$	🟩	🟥	🟥	🟥	🟥
$Cs_2AgInBr_6$	🟩	🟥	🟥	🟥	🟥
$Cs_2AgIn_{0.5}Bi_{0.5}Br_6$	🟥	🟩	🟥	🟥	🟩
$Cs_2AgAl_{0.5}Bi_{0.5}Br_6$	🟥	🟥	🟥	🟥	🟥
$Cs_2AgFe_{0.5}Bi_{0.5}Br_6$	🟩	🟩	🟥	🟥	🟩
$Cs_2AgFe_{0.1}Bi_{0.9}Br_6$	🟥	🟩	🟩	🟥	🟩
$Cs_2AgFe_{0.01}Bi_{0.99}Br_6$	🟥	🟩	🟩	🟥	🟩
$Cs_2AgTi_{0.15}Bi_{0.85}Br_6$	🟥	🟩	🟥	🟥	🟩
$Cs_2AgSn_{0.15}Bi_{0.85}Br_6$	🟩	🟥	🟥	🟥	🟩